

Fluid –Rock Characterization and Interactions in NMR Well Logging

2 st Annual Progress Report

Reporting Period Start Date: August 1, 2000
Reporting Period End Date: July 31, 2001

George J. Hirasaki
Kishore K. Mohanty

Report Issued September 16, 2001

DOE Award Number: DE-AC26-99BC15201

Rice University
6100 Main Street
Houston, TX 77005-1892

Subcontractor
University of Houston
4800 Calhoun Road
Houston, TX 77204-4792

DISCLAIMER

"This report was prepared as an account of work sponsored by an agency of the United States Government. Neither the United States Government nor any agency thereof, nor any of their employees, makes any warranty, express or implied, or assumes any legal liability or responsibility for the accuracy, completeness, or usefulness of any information, apparatus, product, or process disclosed, or represents that its use would not infringe privately owned rights. Reference herein to any specific commercial product, process, or service by trade name, trademark, manufacturer, or otherwise does not necessarily constitute or imply its endorsement, recommendation, or favoring by the United States Government or any agency thereof. The views and opinions of authors expressed herein do not necessarily state or reflect those of the United States Government or any agency thereof."

ABSTRACT

Objective: To characterize the fluid properties and fluid-rock interactions that are needed for formation evaluation by NMR well logging.

This project is a partnership between Professor George J. Hirasaki at Rice University and Professor Kishore Mohanty at University of Houston. In addition to the DOE, this project is supported by a consortium of oil companies and service companies.

The fluid properties characterization has emphasized the departure of live oils from correlations based on dead oils. New measurements are reported for ethane and propane. Mixing rules are developed for methane and gases without protons. The coupling between the relaxation time distribution and the diffusivity distribution is demonstrated with a binary mixture of hexane and squalene. Asphaltic components can result in a difference between the T_1 and T_2 relaxation time distributions. This difference is a function of viscosity and NMR Larmor frequency.

The fluid-rock interactions that are reported here are the effects of surface relaxation and diffusion. The consequence of not being in the fast diffusion regime is examined. Experimental and theoretical aspects of CPMG measurements in a constant field gradient are examined. The pulse field gradient method is explored to evaluate vuggy carbonates.

The objectives of pore morphology and rock characterization are to identify vug connectivity by using X-ray CT scan, and to improve NMR permeability correlation. CT scanning of dry Yates core material shows that uniformity of vug distribution varies from core to core. CT scanning of core floods in one Chester Field sample shows that the vugs are non-touching.

TABLE OF CONTENTS

Disclaimer	1
Abstract	2
Table of Contents	3
List of Graphical Material	3
Introduction	7
Executive Summary	8
Task 1.0 Fluid Properties	10
Relaxation Time and Self-Diffusion Measurements of Pure Ethane and Propane	10
Interpretation of Spin-Lattice Relaxation in CH ₄ , C ₂ H ₆ and CH ₄ Mixtures	28
Relaxation Time and Diffusivity of Hydrocarbon Mixtures	60
Relaxation Time Distribution of Asphaltenic Oils.....	67
Task 2.0 Fluid-Rock Interactions.....	73
Study Of Slow Diffusion In NMR Relaxation Of Water In Porous Media	73
CPMG Relaxation by Diffusion with Constant Magnetic Field Gradient in a Restricted Geometry: Numerical Simulation and Application	83
Laboratory Technique for CPMG Gradient Measurements.....	104
Extending PFG Restricted Diffusion Measurements	109
Task 3.0 PoreMorphology/Rock Characterization.....	118
Study Of Vuggy Carbonate Cores using X-Ray CT	118

LISTS OF GRAPHICAL MATERIAL

Table of Tables

Task 1.0 Fluid Properties	
Relaxation Time and Self-Diffusion Measurements of Pure Ethane and Propane	
Table 1 Spin-lattice relaxation time of pure ethane.	20
Table 2 Spin-lattice relaxation time of pure propane.....	21
Table 3 Diffusion coefficients of pure ethane.....	23
Table 4 Diffusion coefficients of pure propane.	24
Interpretation of Spin-Lattice Relaxation in CH ₄ , C ₂ H ₆ and CH ₄ Mixtures	
Table 1 Relaxation times by spin rotation interaction.....	38
Table 2 Molecular constants of methane.....	40
Table 3 Molecular constants of ethane.....	43
Table 4 Cross section for angular momentum transfer for CH ₄ molecules with various collision partners.	52
Relaxation Time and Diffusivity of Hydrocarbon Mixtures	
Table 1 Relaxation time and diffusivity of <i>n</i> -hexane and squalene mixtures.....	62
Task 2.0 Fluid-Rock Interactions	
CPMG Relaxation by Diffusion with Constant Magnetic Field Gradient in a Restricted Geometry: Numerical Simulation and Application	
Table 1. The boundary between different relaxation regimes.....	96

	Table 2. Summary of the partition of the ($\log_{10} D^*$, $\log_{10} \tau^*$) domain into regions of three relaxation regimes.	96
	Laboratory Technique for CPMG Gradient Measurements	
	Table 1: Signal-to-noise ratio from different sampling techniques.....	108
	Extending PFG Restricted Diffusion Measurements	
	Table 1: Relaxation Times and Diffusivities.....	114
Task	3.0 PoreMorphology/Rock Characterization	
	Study Of Vuggy Carbonate Cores using X-Ray CT	
	Table 1. Available and Selected Parameter in CT-Scan.	121

Table of Figures

Task 1.0 Fluid Properties

Relaxation Time and Self-Diffusion Measurements of Pure Ethane and Propane

Fig. 1	T_1 versus viscosity/temperature plot.	11
Fig. 2	Schematic diagram of the high pressure NMR apparatus.....	13
Fig. 3	NMR system.	14
Fig. 4	Inversion recovery sequence.....	14
Fig. 5	Sequence of pulse gradient spin-echo method.....	16
Fig. 6	Comparison of viscosity for pure ethane – experimental and SUPERTRAPP.....	18
Fig. 7	Comparison of viscosity for pure propane – experimental and SUPERTRAPP.....	19
Fig. 8	T_1 versus viscosity/temperature plot of pure alkanes.....	22
Fig. 9	T_1 versus viscosity plot of pure alkanes.....	22
Fig. 10	T_1 dependence on diffusion coefficient.....	24
Fig. 11	Diffusivity dependence on η/T for pure alkanes.	25

Interpretation of Spin-Lattice Relaxation in CH_4 , C_2H_6 and CH_4 Mixtures

Fig. 1	Proton $T_{1, \text{sr}} / (\rho g(\sigma))$ vs. T plot in methane based on the kinetic model.....	41
Fig. 2	Proton $T_{1, \text{sr}}$ vs. η/T plot in methane based on the diffusion model	41
Fig. 3	$T_{1, \text{sr}} / (\rho g(\sigma))$ vs. T plots in ethane based on the kinetic model.....	45
Fig. 4	$T_{1, \text{sr}}$ vs. η/T plots in ethane based on the diffusion model.....	46
Fig. 5	Correlation of spin rotation T_1 , viscosity and temperature for vapor ethane.	49
Fig. 6	Comparison of experimental results and calculated results for pure ethane.	49
Fig. 7	Contributions to the proton relaxation rate of ethane.	50
Fig. 8	Correlation of cross section for angular momentum transfer by collisions for $\text{CH}_4\text{-He}$	51
Fig. 9	Correlation of cross section for angular momentum transfer by collisions for $\text{CH}_4\text{-Ne}$	52
Fig. 10	Comparison of experimental results and calculated results for $\text{CH}_4\text{-CO}_2$	53
Fig. 11	Comparison of experimental results and calculated results for $\text{CH}_4\text{-N}_2$	53

Fig. 12 Comparison of experimental results and calculated results for CH ₄ -He.	54
Fig. 13 Comparison of experimental results and calculated results for CH ₄ -Ne.	54
Fig. 14 Comparison of experimental results and calculated results for CH ₄ -Ar.	55
Relaxation Time and Diffusivity of Hydrocarbon Mixtures	
Fig. 1. Relaxation time distributions of <i>n</i> -hexane and squalene mixtures	63
Fig. 2 Diffusivity of <i>n</i> -hexane and squalene mixtures.	64
Fig. 3. Constituent relaxation time and diffusivity as a function of concentration.	65
Fig. 4. Ratio of constituent diffusivity and relaxation time compared to the correlation.	65
Fig. 5 Correlation between constituent diffusivity and relaxation time of <i>n</i> -hexane and squalene.	66
Relaxation Time Distribution of Asphaltenic Oils	
Fig. 1. T_1 and T_2 relaxation times as a function of viscosity and frequency.	69
Fig. 2. Effect of oxygen on relaxation time of alkanes.	69
Fig. 3. Relaxation time distributions of a light oil.	70
Fig. 4. Relaxation time distributions of a moderate gravity oil.	70
Fig. 5. Relaxation time distributions for a viscous oil.	71
Fig. 6. Relaxation time distributions of a very heavy oil.	71
Fig. 7. Correlation of log mean T_1/T_2 with oil viscosity, 2 MHz.	72
Fig. 8. Correlation of the peaks of the distributions with the asphaltene content, 2 MHz.	72
Task 2.0 Fluid-Rock Interactions	
Study Of Slow Diffusion In NMR Relaxation Of Water In Porous Media	
Fig. 1 (a). T_2 relaxation time distribution calculated from analytical solution for a single-pore in the slow-diffusion region.	77
Fig. 1(b) T_2 relaxation time distribution.	78
Fig. 2. Sum of higher order relative intensities versus $\rho a/D$	78
Fig. 3. Log Mean T_2 versus surface relaxivity.	79
Fig. 4. Dimensionless Log Mean T_2 versus $\rho a/D$	80
Fig. 5. Dimensionless Log Mean T_2 versus dimensionless group $a/(\rho^* T_{2B})$	81
Fig. 6. Contour plot of Dimensionless Log Mean T_2 with respect to dimensionless group $\rho a/D$ and $a/(\rho^* T_{2B})$	82
CPMG Relaxation by Diffusion with Constant Magnetic Field Gradient in a Restricted Geometry: Numerical Simulation and Application	
Fig. 1. CPMG pulse sequence.	97
Fig. 2. System of study.	97
Fig. 3. Partition of the $(\log_{10} D^*, \log_{10} \tau^*)$ domain into three relaxation regimes.	98
Fig. 4. Comparison of contour lines of T_2^*	98

Fig. 5. Contour lines of T_2^* from Eq. [7].	99
Fig. 6. Contour lines of T_2^* from Eq. [8].	99
Fig. 7. Contour lines of T_2^* from Eq. [9].	100
Fig. 8. Contour lines of T_2^* from Eq. [10].	100
Fig. 9. Vertical branch point lines on the $(\log_{10} D^*, \log_{10} \tau^*)$ domain.	101
Fig. 10. Contour lines of T_2^* from Eq. [10].	101
Fig. 11. Comparison of numerical simulation results with analytical solutions with newly-adjusted boundaries.	102
Fig. 12. Relaxation rate vs. half echo spacing on a log-log plot.	103
Laboratory Technique for CPMG Gradient Measurements	
Fig. 1: Frequency drift as a function of total pulsing time.	105
Fig. 2. Pulse Spacing Shift.	105
Fig. 3: First ten echoes.	106
Fig. 4: Centering of the Sampling Window.	107
Fig. 5: Matched Filter Data.	107
Extending PFG Restricted Diffusion Measurements	
Fig. 1: The Hahn Echo in a Magnetic Field Gradient.	110
Fig. 2: Pulsed Field Gradient Sequence.	111
Fig. 3: Pulsed Field Gradient – Stimulated Echo Sequence.	112
Fig. 4: Water-Saturated T_2 Distribution.	115
Fig. 5: Pentane-Saturated T_2 Distribution.	115
Fig. 6: Diffusion decay comparison.	115
Fig. 7: Restricted diffusion comparison. Both samples are Yates field carbonates saturated with pentane.	116
Task 3.0 PoreMorphology/Rock Characterization	
Study Of Vuggy Carbonate Cores using X-Ray CT	
Fig. 1 Simplified Model of Carbonate Rocks.	119
Fig. 2. Picture of sample no.17C9.	123
Fig. 3 CT Image for sample 17C9 at selected slices.	123
Fig. 4 Picture of sample no. 2416.	124
Fig. 5 CT Images for Sample 2416 at selected slices.	124
Fig. 6 Picture of sample no. 7626B.	125
Fig. 7 CT Images for Sample 7626B at selected slices.	125
Fig. 8 Porosity distribution from CT scans.	129
Fig. 9 Doped brine profile at 0.25 PV Injected.	130
Fig. 10 Doped brine profile at 0.5 PV Injected.	131
Fig. 11 Doped brine profile at 1.25 PV injected.	132
Fig. 12 Doped Oil Profile at S_{wr} .	133
Fig. 13 Doped Oil Profile at S_{or} .	134
Fig 14. T_2 distribution for Chester Field sample and for doped oil.	135

INTRODUCTION

Objective: To characterize the fluid properties and fluid-rock interactions which are needed for formation evaluation by NMR well logging.

NMR well logging is finding wide use in formation evaluation. The formation parameters commonly estimated are porosity, permeability, and capillary bound water. Special cases include estimation of oil viscosity, residual oil saturation, location of oil/water contact, and interpretation on whether the hydrocarbon is oil or gas. In most cases, it is adequate to determine if the formation is sandstone or carbonate and then use default parameters and interpretation methods. However, it is important to recognize the exceptional cases and have parameters and interpretation methods for these cases.

Default rock and fluid properties are very useful in the interpretation of NMR logs because the exact lithology and fluid composition of the logged interval may not be known. In most cases it is necessary to only know if the formation is sandstone or carbonate. For example, a water-wet sandstone formation with insignificant internal gradient effects, having microporosity that is diffusionally isolated from the macropores and containing a hydrocarbon with a unit hydrogen index and long bulk relaxation time can use a 33 ms T_2 cutoff to estimate the volume of capillary-bound water, mobile fluids, total porosity, and permeability (Kenyon, 1997; Kleinberg and Vinegar, 1996; Straley, et al., 1997). However, there are limits to the validity of the default properties and core analysis or fluid analysis will be needed in these cases to refine the correlations.

Some exceptions we propose to address are as follows: (1) departure of the relaxation time – viscosity correlation for methane-containing live oil from existing correlations based on stock tank oils and viscosity standards, (2) departure of the live oil hydrogen index from unity or the correlations based on alkanes or on API gravity, (3) crude oils that have bulk fluid relaxation time distributions that overlap with that for the capillary bound water, (4) wettability alterations that result in oil relaxation time distributions that overlap with that for the capillary bound water, (5) wettability alteration with crude oils and oil based drilling fluids that alter value of the capillary bound water from that of water-wet conditions, (6) diffusion effects resulting from internal gradients which cause an echo spacing dependent shortening of the relaxation time distribution for both brine and hydrocarbons, (7) diffusional coupling between the brine in the micropores and the brine in the macropores, and (8) estimation of permeability of vuggy carbonates.

EXECUTIVE SUMMARY

The work is divided into; Task 1.0 Fluid Properties, Task 2.0 Fluid-Rock Interactions, Task 3.0 Pore Morphology/Rock Characterization.

Task 1.0 Fluid Properties

The main emphasis of fluid properties is the characterization of live oils. The relaxation time versus oil viscosity correlations in the literature are based on dead oils. Live oils are expected to differ from dead oils because methane relaxes with the spin-rotation mechanism while higher molecular weight hydrocarbons relax by the dipole-dipole mechanism. These two mechanisms have the opposite dependence on viscosity. A correlation between relaxation time, diffusivity, and gas/oil ratio was developed and reported in the 1st annual report. This report has measurements of relaxation time and diffusivity of pure ethane and propane. These two hydrocarbons are components of natural gas in addition to methane. The results show that ethane, similar to methane, has a significant spin-rotation contribution to relaxation, even as a liquid. Propane has relaxation time dependence more similar to that of the higher alkanes but it also appears to have a small contribution from spin-rotation. Literature data show the influence of gas components without hydrogen, such as nitrogen and carbon dioxide on the relaxation of methane. Models for the contributions of these components are presented.

Several methods of fluid identification in NMR logging depend on the difference of both the relaxation time and diffusivity of the fluids. Crude oils often have a broad relaxation time and diffusivity distributions. One recent fluid identification method assumes that the distributions of relaxation time and diffusivity are coupled. Laboratory measurements were made with a binary mixture of *n*-hexane and squalene to verify this assumption.

Asphaltic oil may be problematic because of the broad relaxation time distribution and possibly reduced hydrogen index. The ratio of T_1/T_2 is a function of the viscosity and asphaltene content as well as the Larmor frequency.

Task 2.0 Fluid-Rock Interactions

A basic assumption for estimating the pore size distribution from the relaxation time distribution is that the system is in the, “fast-diffusion limit.” This condition exists when the diffusivity of the fluid in the pore is large enough that the magnetization profile in the pore has a uniform value due to being “well-mixed” by diffusion. The relaxation response when the system is not in the fast-diffusion limit is examined. The analytical solution for the response shows not a single relaxation time for the pore but rather a dominant relaxation time and several shorter and smaller amplitude relaxation times. The mean relaxation time for the slab, cylinder, and spherical pore geometry are presented as a function of dimensionless groups. The dimensionless groups are the ratio of surface relaxation rate to diffusion rate and the bulk relaxation time to the fast-diffusion surface relaxation time.

Constant gradient CPMG is used in NMR well logging for fluid identification. A numerical investigation examines the CPMG response in a 1-D pore with zero surface relaxation. The relaxation time can be expressed as a function of two dimensionless groups. The analysis show that the values of the dimensionless groups which define the

boundary between the different regimes are different from the values presented in the literature.

Fluid identification with NMR logs is made with a static magnetic field gradient. Some issues with laboratory gradient CPMG measurements are discussed. Gradients established with a electromagnet develops heat and a change in the temperature of the permanent magnet will change the Larmor frequency. Even with a cooling system, the system must be operated long enough to reach a steady state condition. The interval between the 90° pulse and the first 180° pulse in a gradient CPMG sequence should be slightly less than one-half of the echo spacing. The echo shape in gradient CPMG is very narrow and the timing may need to be adjusted to measure the peak of the echo.

The relaxation time distribution is not a good estimator of permeability in vuggy carbonates. This is because the relaxation time is an estimator of the pore body size distributions and the pore body size of carbonates does not correlate well with the pore throat size. Measurement of restricted diffusion with pulse field gradient measurements has the potential to measure the tortuosity of the medium. Restricted diffusion was measured for two vuggy carbonate samples, one high permeability and the other low permeability. Pentane was used as the fluid since it has a higher diffusivity and relaxation time and a lower surface relaxivity compared to water.

Task 3.0 Pore Morphology/Rock Characterization.

The objectives of pore morphology and rock characterization are to identify vug connectivity by using X-ray CT scan, and to improve NMR permeability correlation. CT scanning of dry Yates core material shows that uniformity of vug distribution varies from core to core. CT scanning of core floods in one Chester Field sample shows that the vugs are non-touching.

Task 1. Fluid Properties.

Relaxation Time and Self-Diffusion Measurements of Pure Ethane and Propane

Ying Zhang, George J. Hirasaki, Riki Kobayashi, and Waylon House
Rice University, Houston, Texas

Abstract

The proton spin lattice relaxation time T_1 and self-diffusion coefficient D have been measured in ethane and propane from 20 to 52 °C at pressures up to 6000 psia using an 89MHz NMR apparatus.

I. Introduction

Nuclear Magnetic Resonance (NMR) technique is based on the measurements of absorption of electromagnetic radiation of material in a magnetic field. It can provide the information of spin-lattice relaxation time, T_1 , and the diffusion coefficient, D . NMR technique has been widely used for studies of molecular motion and for the measurements of rock and fluid properties for the past decades.

Viscosity and diffusivity are important transport properties in understanding the flow of fluid in porous media. Figure 1 is the plot of relaxation time versus viscosity/temperature for pure alkanes and alkane mixtures.¹⁻⁶ Previous work shows that pure higher alkanes, higher alkane mixtures, viscosity standards and stock tank crude oils have NMR relaxation times which vary linearly with viscosity/temperature on a log-log scale. The work by this lab shows that pure methane and methane-alkane mixtures at some temperatures and pressures do not follow the trend. Methane relaxes by spin rotation mechanism in addition to dipole-dipole interactions while other higher alkanes relax only by dipole-dipole interactions. The straight line of liquid ethane departs from the linear correlation of higher alkanes. It is interesting to note that the curve of liquid methane converges to the curve of liquid ethane with increasing viscosity/temperature.

Propane is a non-polar alkane containing three C-atoms and is a substance of great technical importance. In addition, ethane and propane are also common components of natural gas associated with oils at reservoir conditions. However, the NMR relaxation time has not been previously measured for these materials at conditions typical of petroleum reservoirs.

It is not certain if ethane and propane will relax by spin-rotation mechanism like methane or by dipole-dipole interactions as other higher alkanes. So the objectives of this work are to measure proton spin-lattice relaxation times and self-diffusion coefficients of ethane and propane. Then the relationships between transport properties, temperature and relaxation times were investigated.

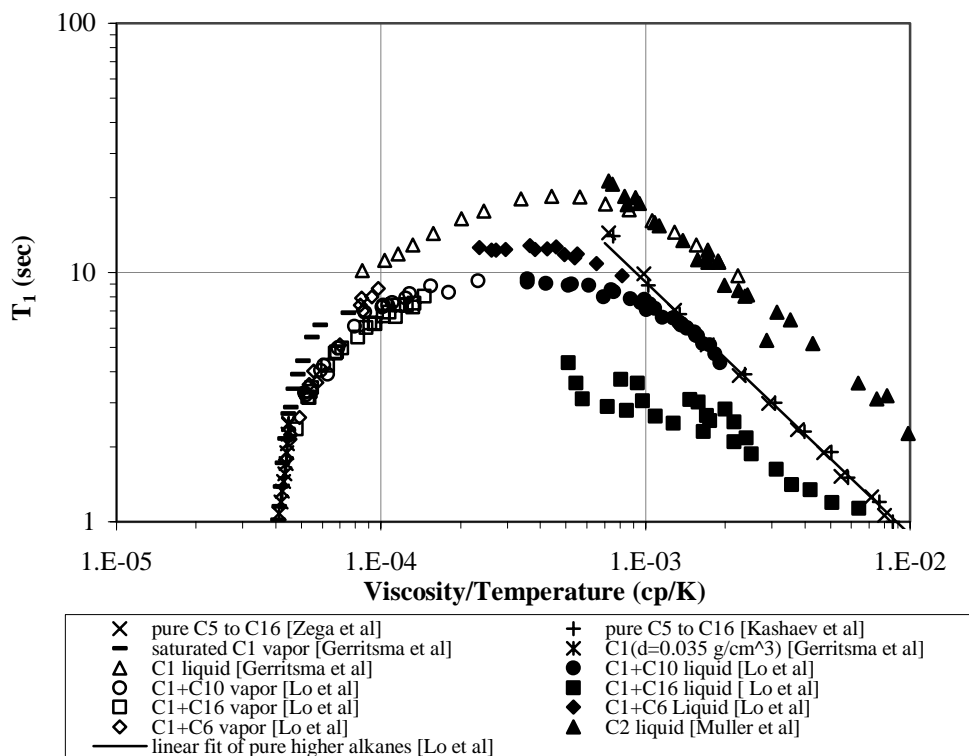


Figure 1 T_1 versus viscosity/temperature plot

II. Experimental procedure

2.1. Equipment

Relaxation times and self-diffusion of ethane and propane at elevated temperatures and pressures were measured with a super-conducting NMR spectrometer^{3, 7}. This spectrometer is connected with a high pressure vapor-liquid equilibrium apparatus and a temperature regulated air bath that maintains a constant temperature of the fluid as it is introduced to the NMR probe. Figure 2 is a schematic diagram of the apparatus. The magnet is a super-conducting magnet made by Oxford with the proton frequency of 89 MHz. It is kept at liquid helium temperature. The probe is made specifically for high pressure fluids by constructing the sample chamber and sensing coils inside the pressure vessel.

The system pressure is generated by the two high pressure hand pumps, HiP Model 62-6-10. For fluid experiments, a hand pump with bigger volume is introduced to the system, which can help achieve high pressure. The pressures are measured at three different locations. Two pressure transducers are installed near the HiP high pressure

pumps, and the other one is installed between the sapphire cell and NMR probe. The pressure transducers used to measure the pump pressure are Setra Model 204, with pressure range 0 to 5000 psig. The one used to measure system pressure is Setra Model 280E, with pressure range 0 to 10000 psig. All of the pressure transducers are connected to the Omega high performance strain gauge indicators model DP41-S for pressure readings. The transducers are calibrated with a Ruska dead weight gauge.

The temperature is controlled by an air bath. Heat is generated by eight coiled Nichrome heating elements. Six of the heating elements are connected in series to a power stat to supply a baseline output. The others are connected to a Bayley Model 123 precision temperature controller. The actual NMR system is presented in Figure 3. Air from the bath is circulated externally to the probe by four blowers. Two of them are right below the heating elements and blow the hot air to the upper part of the air bath system. The top blower moves hot air to the probe through PVC pipes and the exhausted hot air is sucked out of the conduit by the bottom blower. Thus the return air goes through the heater unit and is reheated. The temperature operating range is 20 °C to 60 °C. Three non-magnetic RTDs (resistant temperature detectors) are added to the apparatus for temperature measurements. The temperatures are taken in the closed air bath system, at the probe and at the magnet bore. The RTDs are connected to Omega Model CN77373-C2 temperature meters. The temperature accuracy is ± 0.2 °C. The reported temperature is the one taken at the sample probe.

There are two problems in the heating system. First, the magnet must be kept at liquid helium temperature, therefore it is surrounded by liquid helium and liquid nitrogen. When elevated temperature experiments are performed, the magnet bore could be heated thus the liquid nitrogen and liquid helium may be vaporized. In order to keep the magnet bore cool, a PVC liner is installed between the magnet bore and the sample probe. When high temperature experiments are performed, the hot air goes inside of the PVC liner, and chilled air is forced through between the magnet bore and the PVC liner. This way the magnet bore is kept well below 25 °C. The other problem is the thermal gradient. It can be minimized by wrapping thick fiberglass insulation around the PVC pipes.

Two high pressure tubes are added to connect the sapphire cell and the sample probe, so the samples can be transferred to and from the probe. The samples are transferred by a magnetic pump.

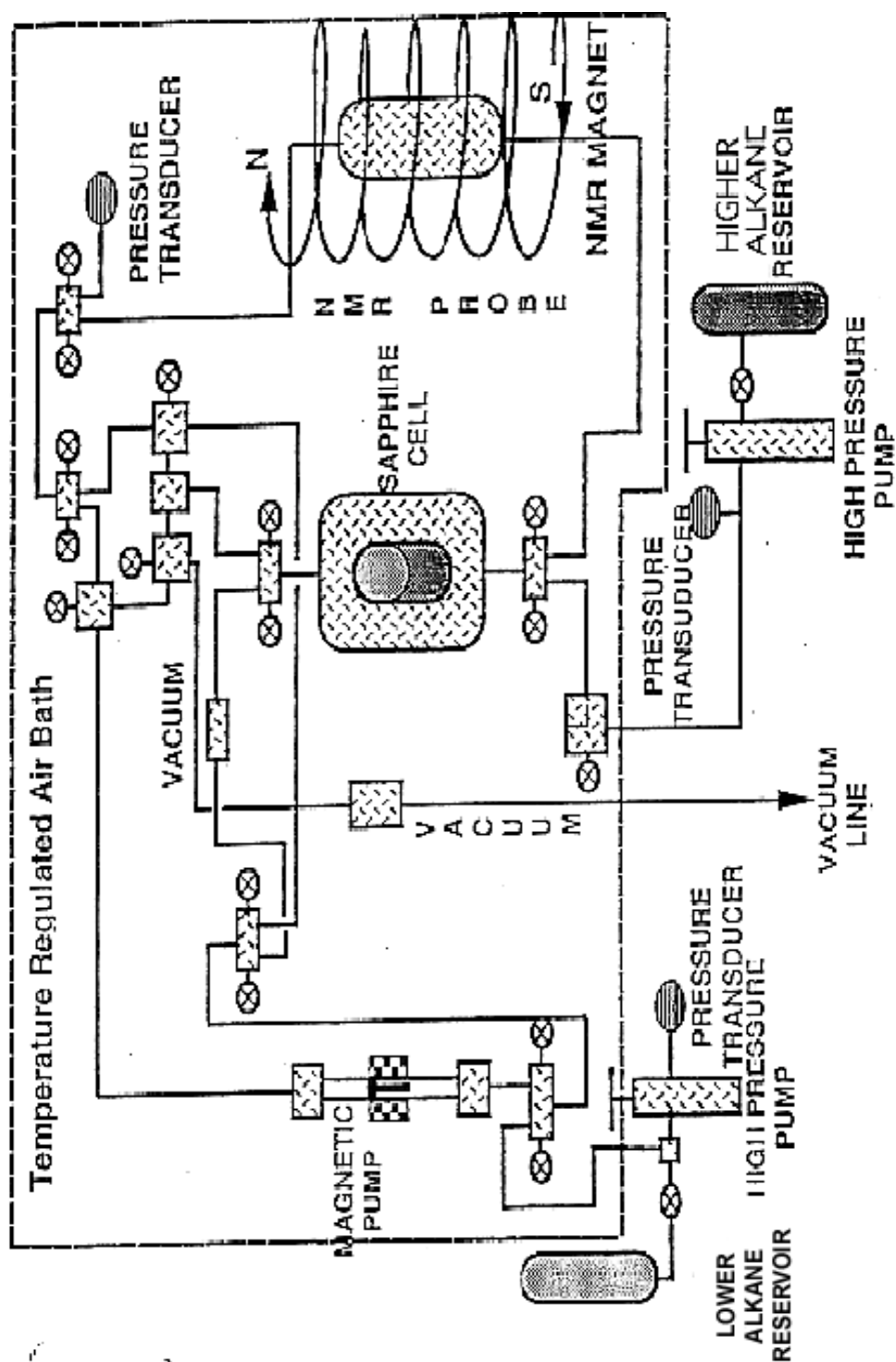


Figure 2 Schematic diagram of the high pressure NMR apparatus

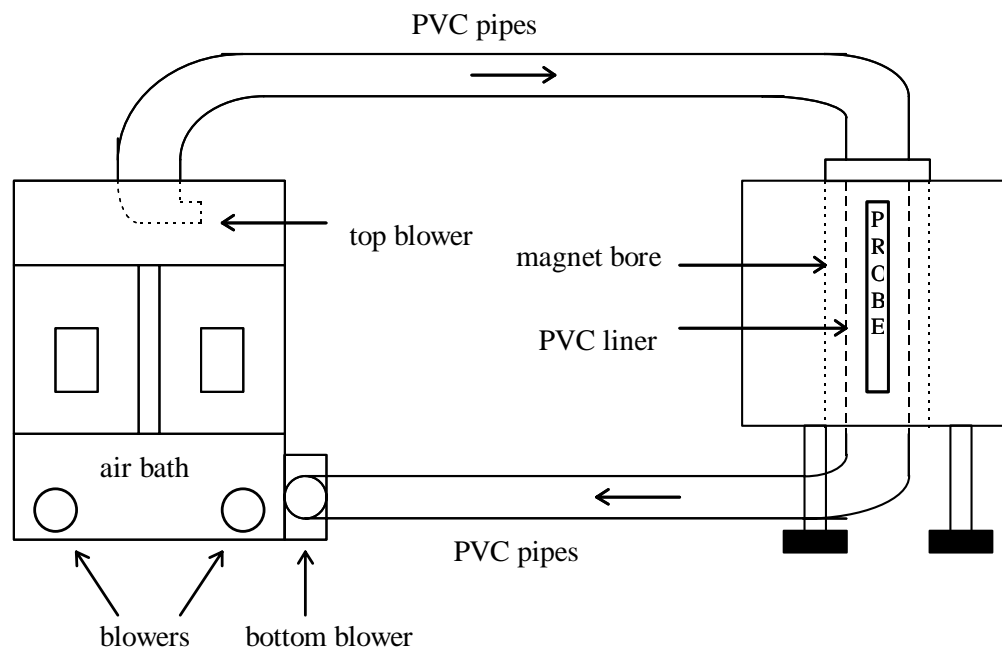


Figure 3 NMR system

2.2. Sample preparation

Pure ethane and propane gases were obtained from Matheson Gas Products. The quality of both ethane and propane was Matheson purity, 99.95% minimum. The oxygen content was less than 2 ppm. No further purification of ethane and propane was attempted except further removal of oxygen.

Oxygen presence affects relaxation time significantly since it is paramagnetic. The oxygen contained in ethane and propane gases was further removed by passing the gases through an oxygen absorbing purifier, Matheson Model 6411. The oxygen content should be less than 0.1 ppm after purifying.

The apparatus should be cleaned before introducing a new sample. The apparatus was filled with hexane for one day and then the hexane was flushed out. Then the apparatus was heated to 50 °C and evacuated for at least eight hours to ensure complete removal of hexane. The cleaning procedure was performed three times.

2.3. Spin-lattice relaxation time measurements

T_1 was measured by the inversion recovery method¹⁸. The pulse sequence of inversion recovery method consists of a 180° pulse followed by a 90° pulse, as shown in Figure 4. The 180° pulse inverts the equilibrium magnetization M to the negative z-axis. After delay t , a 90° pulse is applied to tip the magnetization to x-y plane, the free induction decay is recorded to get the initial amplitude of the FID, which is proportional to M . For

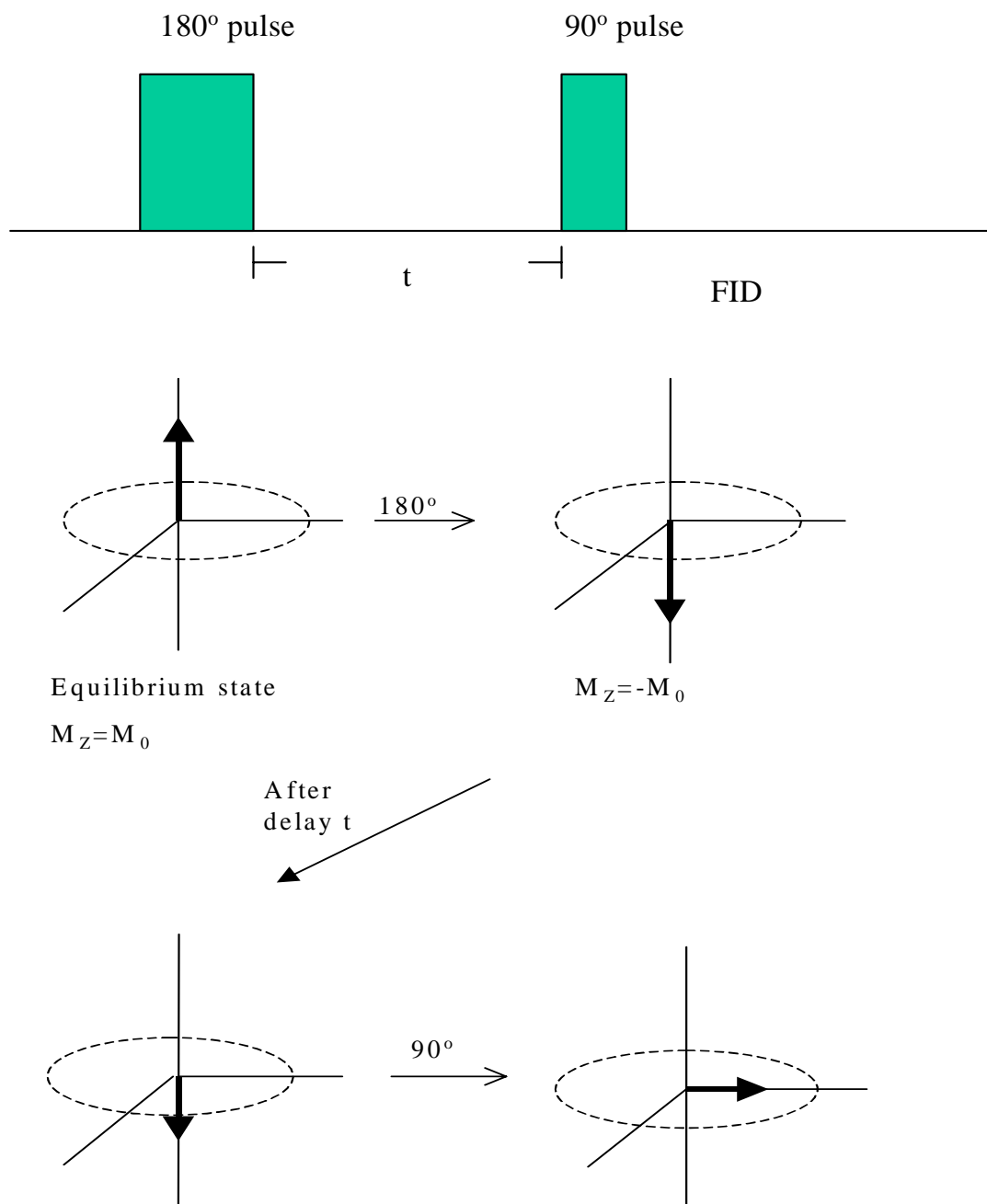


Figure 4 Inversion recovery sequence

each measurement, 35 to 50 FIDs are acquired over duration time t up to five times the longest T_1 . The data collected are t 's and their corresponding magnetization M_z . With the initial condition $M_z = -M_0$ at $t = 0$, T_1 for a single type of protons can be described as a function of t ,

$$M_z = M_0 \left(1 - 2e^{\frac{-t}{T_1}} \right) \quad (1)$$

The amplitude M_0 is determined at least four times by taking the maximum point of the FID and the average is used. T_1 is determined from a least square fit of

$$f(t) = \ln \left(\frac{M_o - M_z}{2M_o} \right) \text{ vs. } t.$$

2.4. Self-diffusion measurements

Pulse gradient spin-echo sequence¹⁹ is used for diffusion measurements. The pulse sequence consists of a 90° pulse, a 180° pulse and two gradient pulses. A 90° pulse is first applied to flip the magnetization to y-axis, and the spin isochromats start to dephase due to the inhomogeneity of B_0 . Then a magnetic field gradient of strength g and duration δ is applied, followed by a 180° pulse. The gradient causes the spins to dephase more rapidly, with the normal rate of dephasing resuming after the gradient pulse. The 180° pulse flips the spins to reverse the direction of dephasing. A second identical gradient pulse is applied after the 180° pulse to affect the dephasing rate. The time interval between two RF pulses is τ , and the time between two gradient pulses is called Δ . A spin-echo occurs at time 2τ . Figure 5 is the sequence of the pulse gradient spin-echo method.

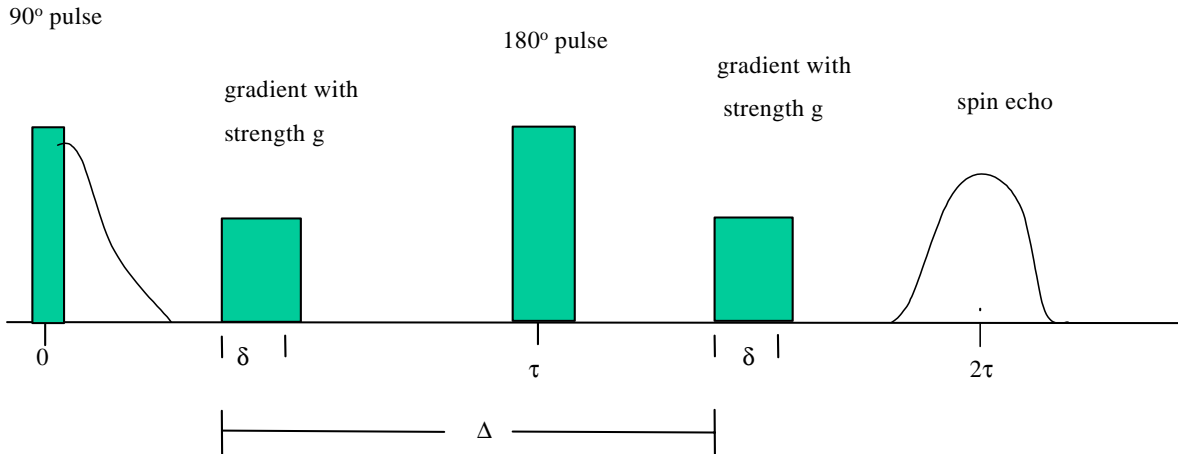


Figure 5 Sequence of pulse gradient spin-echo method

For unbounded diffusion, the random walk motion of molecules can be described as a probability function $P(\mathbf{r}_0 | \mathbf{r}, t)$. \mathbf{r}_0 is the initial position of a molecule, and \mathbf{r} is the position it moves to after the time interval t . According to Fick's law, the probability can be described as

$$P(\mathbf{r}_0 | \mathbf{r}, t) = (4\pi Dt)^{-\frac{3}{2}} e^{-\frac{(\mathbf{r}-\mathbf{r}_0)^2}{4Dt}} \quad (2)$$

In this equation, D is the diffusion coefficient. This corresponds to a Gaussian distribution with variant $2Dt$. For a nuclear spin that diffuses according to the previous equation, the spin echo height attenuation R for the pulse gradient experiment is given by

$$R = \frac{M}{M(0)} = e^{-\gamma^2 \delta^2 g^2 (\Delta - \frac{1}{3}\delta) D} \quad (3)$$

where γ is the gyromagnetic ratio of the spin. M is the echo height with applied gradient, g , and $M(0)$ is the echo height when the gradient is off.

When measuring the diffusion coefficient with pulse gradient spin-echo sequence, g , δ or Δ can be varied. If we take the natural logarithm of Equation (3), we get

$$\ln(R) = -\gamma^2 \delta^2 G^2 \left(\Delta - \frac{1}{3}\delta \right) D \quad (4)$$

The diffusion coefficient can be calculated by plotting $\ln(R)$ vs. $-\gamma^2 \delta^2 G^2 \left(\Delta - \frac{1}{3}\delta \right)$. The slope is the diffusion coefficient.

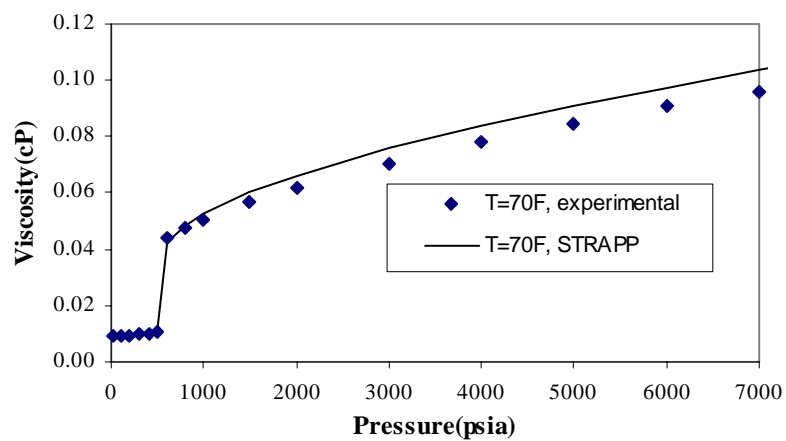
For each measurement, the gradient duration δ was changed. 30 to 40 data points were taken at different δ , and the corresponding echo height was recorded. All other variables (g and Δ) were kept constant within one experiment.

2.5. Estimation of viscosity

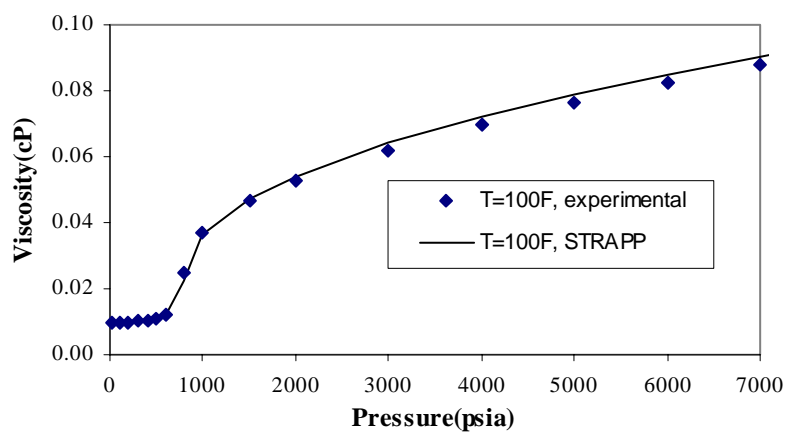
Figure 6 compares the estimated viscosity by SUPERTRAPP with literature experimental data²¹ for pure ethane at 70, 100 and 130 °F in temperature, and 15 to 7000 psia in pressure. SUPERTRAPP is a software for thermodynamic and transport properties estimation (NIST, 1999).²⁰ It turns out that SUPERTRAPP gives close estimations for ethane at higher temperature. For estimation of lower temperature (70 °F), the error increases with pressure. Therefore, interpolations of experimental data were used to estimate ethane viscosity.

Viscosity of pure propane was estimated by SUPERTRAPP. Estimated viscosity data by SUPERTRAPP were compared with literature experimental data¹²⁻¹⁷ at 70, 100 and 130 °F in temperature, and 200 to 7000 psia in pressure. Figure 7 shows the results of comparison. SUPERTRAPP can give good estimation at the temperature range from 70 °F to 130 °F. Since most of the measurements are in this temperature range, SUPERTRAPP estimations are adequate within experimental conditions.

(a)



(b)



(c)

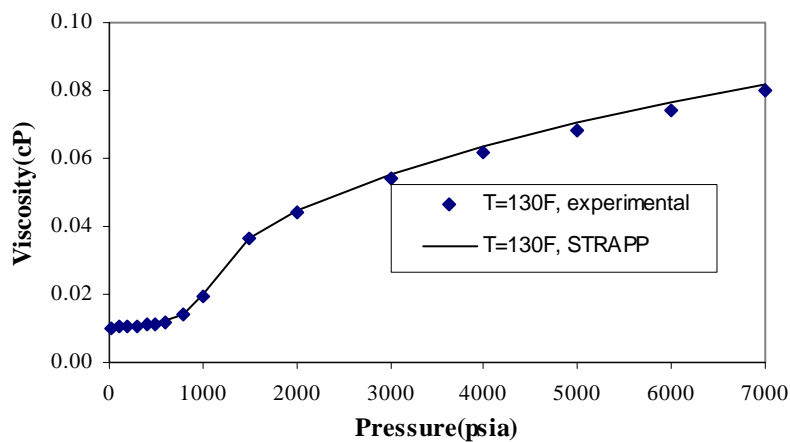
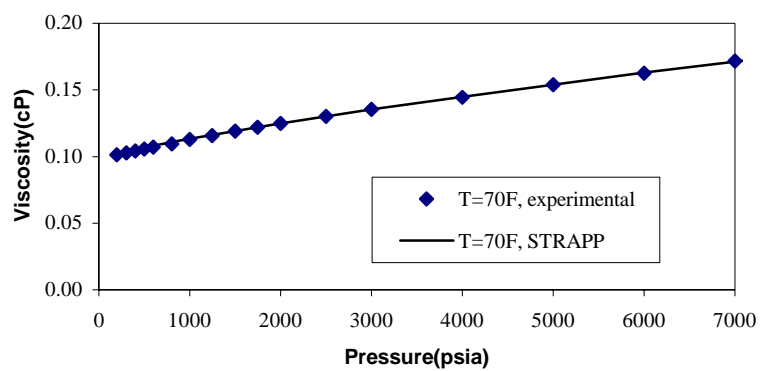
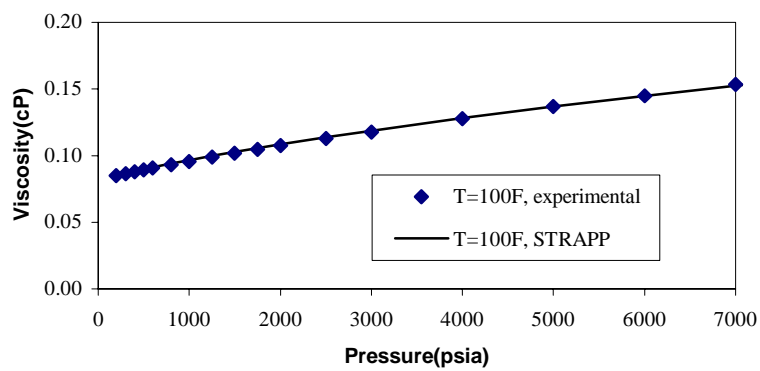


Figure 6 Comparison of viscosity for pure ethane – experimental and SUPERTRAPP

(a)



(b)



(c)

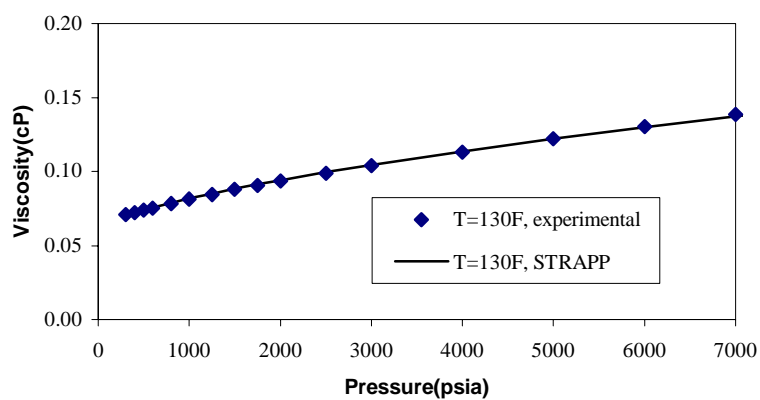


Figure 7 Comparison of viscosity for pure propane – experimental and SUPERTRAPP

III. Results and discussion

3.1. Relaxation time

Relaxation times of pure ethane and propane were measured at various temperatures and pressures. The results were posted in Table 1 and Table 2 respectively.

Figure 8 is the plot of relaxation time versus viscosity/temperature for pure ethane, pure propane, pure methane and other pure alkanes.^{1, 2, 4, 5, 6} The relaxation behavior of ethane and propane is similar to that of methane. Pure ethane and propane at some temperatures and pressures do not follow the linear relationship, either. It seems that the data points of propane are on the curve of methane. Similar to methane, ethane and propane may relax by spin rotation mechanism in addition to dipole-dipole interactions while other higher alkanes relax only by dipole-dipole interactions. The spin rotation mechanism has a different dependence on viscosity/temperature.

Figure 9 shows the plot of T_1 versus viscosity. It is interesting to note that the data points of methane, ethane, propane and other alkanes fall on the same curve by this plot. It will be meaningful to investigate what factors contribute to this phenomenon.

Table 1 Spin-lattice relaxation time of pure ethane

Temp. (°C)	Pressure (psia)	Viscosity (cP)	Visc./Temp. (cP/K)	Log mean T_1 (sec)
19.4	433	9.48E-03	3.24E-05	7.20
19.3	495	9.68E-03	3.31E-05	7.28
19.6	550	2.45E-02	8.38E-05	19.50
20.0	572	3.95E-02	1.35E-04	20.39
20.5	658	4.82E-02	1.64E-04	20.06
20.0	990	5.14E-02	1.75E-04	22.10
19.6	1612	5.85E-02	2.00E-04	21.24
19.9	2344	6.56E-02	2.24E-04	22.01
19.9	2948	7.07E-02	2.41E-04	19.52
20.3	2764	6.91E-02	2.35E-04	18.37
19.9	3825	7.76E-02	2.65E-04	19.40
20.0	4409	8.16E-02	2.78E-04	17.46
27.8	576	1.23E-02	4.09E-05	8.57
28.7	706	3.43E-02	1.14E-04	16.75
32.1	1336	4.78E-02	1.57E-04	18.28
33.4	761	2.87E-02	9.36E-05	17.64
34.9	1151	4.28E-02	1.39E-04	18.36
36.1	663	1.88E-02	6.08E-05	9.94
36.1	802	2.73E-02	8.82E-05	17.56
36.3	613	1.54E-02	4.98E-05	8.49
36.7	716	2.09E-02	6.76E-05	10.28
46.1	739	1.71E-02	5.36E-05	9.07

Table 2 Spin-lattice relaxation time of pure propane

Temp. (°C)	Pressure (psia)	Viscosity (cP)	Visc./Temp. (cP/K)	Log mean T_1 (sec)
18.7	114	8.48E-03	2.91E-05	3.93
29.0	150	8.91E-03	2.95E-05	5.66
33.0	160	9.05E-03	2.96E-05	3.79
20.2	211	1.04E-01	3.54E-04	21.69
20.7	403	1.06E-01	3.60E-04	21.11
19.4	639	1.21E-01	4.13E-04	19.86
20.4	971	1.14E-01	3.87E-04	21.71
20.8	1501	1.20E-01	4.07E-04	23.16
20.7	1994	1.25E-01	4.26E-04	22.65
20.7	2501	1.31E-01	4.44E-04	21.99
20.1	3026	1.37E-01	4.66E-04	20.99
20.4	4040	1.46E-01	4.98E-04	18.70
20.8	4569	1.51E-01	5.12E-04	20.91
20.8	5003	1.54E-01	5.26E-04	18.91
20.8	5940	1.63E-01	5.54E-04	18.72
52.5	304	7.22E-02	2.22E-04	26.85
52.3	604	7.75E-02	2.38E-04	26.42
51.8	1049	8.46E-02	2.60E-04	26.67
52.3	2023	9.60E-02	2.95E-04	25.49
52.5	2981	1.06E-01	3.25E-04	23.50
48.5	3960	1.18E-01	3.67E-04	23.24
52.5	3997	1.15E-01	3.53E-04	23.73
48.5	4987	1.27E-01	3.94E-04	21.58
52.5	5979	1.31E-01	4.03E-04	19.39

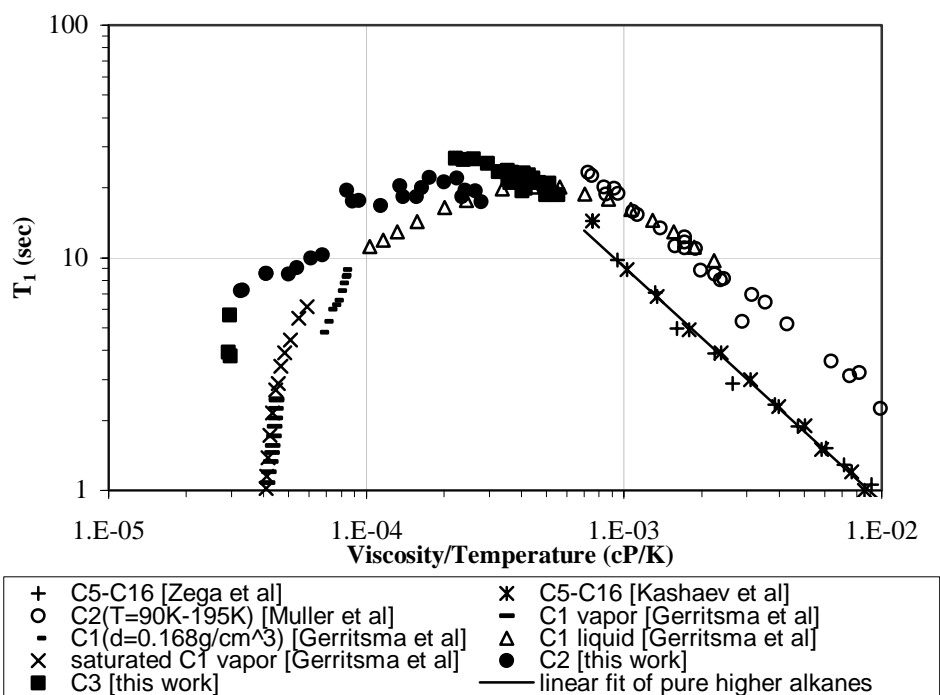


Figure 8 T_1 versus viscosity/temperature plot of pure alkanes

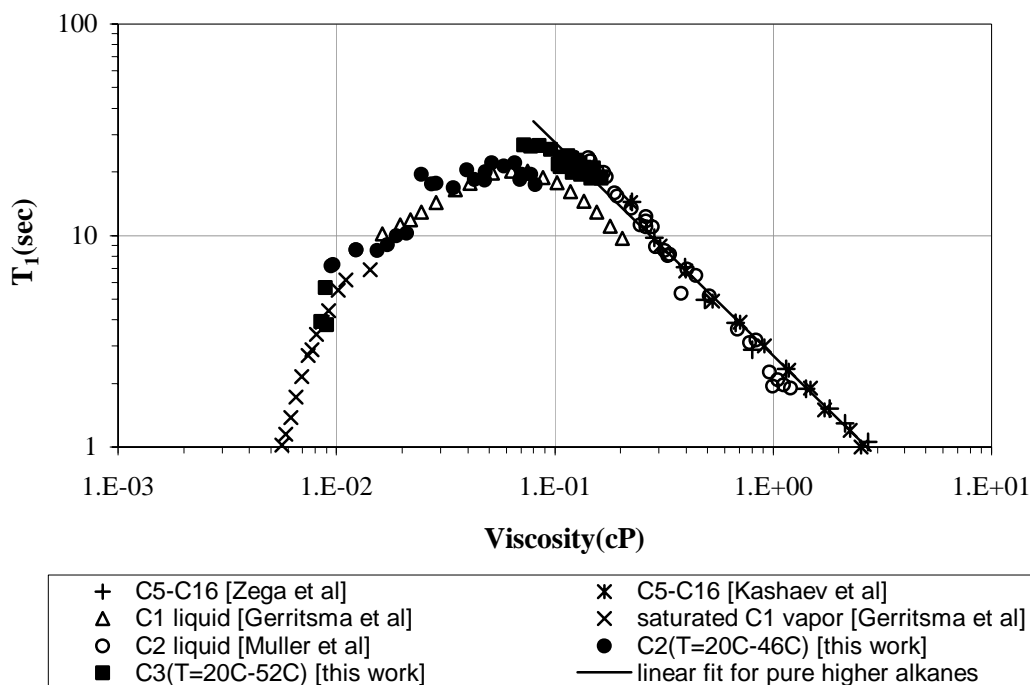


Figure 9 T_1 versus viscosity plot of pure alkanes

3.2. Diffusion coefficient

Self-diffusion coefficients of ethane were also measured at various temperatures and pressures. The result was shown in Table 3. The attempt to measure diffusion coefficient for propane is not very successful. The power supply to the NMR spectrometer was changed and the new power line introduced significant noise. For vapor propane, the spin echo signal is too small to be measurable. Diffusion coefficient measurement can be made for liquid propane. However, the noise was still large although the scan number was doubled. The diffusion coefficient data obtained for the propane system may show greater error than the ethane system. Table 4 listed the diffusion coefficient data for propane.

T_1 dependence on diffusion coefficient was plotted and observed. Figure 10 is the plot of log mean T_1 against diffusion coefficient for ethane, propane and other alkanes.³ Ethane and propane depart from the straight line of the pure higher alkanes.

Table 3 Diffusion coefficients of pure ethane

Temp. (°C)	Pressure (psia)	Viscosity (cP)	Visc./Temp. (cP/K)	Log mean $D(\text{cm}^2/\text{sec})$
19.7	434	9.50E-03	3.24E-05	1.28E-03
19.2	483	1.13E-02	3.87E-05	6.05E-04
19.9	571	3.96E-02	1.35E-04	3.06E-04
20.1	722	4.91E-02	1.68E-04	2.56E-04
20.1	835	4.92E-02	1.68E-04	2.44E-04
20.2	925	5.04E-02	1.72E-04	2.35E-04
20.0	1560	5.80E-02	1.98E-04	2.38E-04
20.1	2233	6.46E-02	2.20E-04	2.32E-04
20.0	2929	7.04E-02	2.40E-04	2.05E-04
19.8	3791	7.71E-02	2.63E-04	1.98E-04
19.7	4557	8.27E-02	2.82E-04	1.87E-04
28.0	549	1.19E-02	3.96E-05	1.12E-03
28.0	577	1.23E-02	4.09E-05	1.40E-03
28.7	706	3.43E-02	1.14E-04	3.95E-04
32.0	1301	4.72E-02	1.55E-04	3.16E-04
33.4	761	2.87E-02	9.36E-05	5.30E-04
35.0	1137	4.20E-02	1.36E-04	3.40E-04
36.1	802	2.73E-02	8.82E-05	4.59E-04
36.3	614	1.54E-02	4.98E-05	9.02E-04
36.5	474	1.07E-02	3.46E-05	1.52E-03
36.7	715	2.09E-02	6.76E-05	7.84E-04
46.3	740	1.71E-02	5.36E-05	9.24E-04

Table 4 Diffusion coefficients of pure propane

Temp. (°C)	Pressure (psia)	Viscosity (cP)	Visc./Temp. (cP/K)	Log mean $D(\text{cm}^2/\text{sec})$
18.4	124	1.04E-01	3.58E-04	1.77E-04
20.5	609	1.09E-01	3.71E-04	1.62E-04
20.6	986	1.14E-01	3.87E-04	1.19E-04
16.0	1967	1.30E-01	4.50E-04	1.04E-04
18.4	2988	1.38E-01	4.74E-04	1.10E-04
19.1	3958	1.47E-01	5.02E-04	1.11E-04
17.5	5027	1.59E-01	5.46E-04	1.04E-04
17.5	5943	1.67E-01	5.74E-04	8.56E-05
28.8	159	9.36E-02	3.10E-04	1.67E-04
40.0	219	8.30E-02	2.65E-04	2.17E-04
40.0	2161	1.08E-01	3.45E-04	1.32E-04
52.6	309	7.22E-02	2.21E-04	2.07E-04
52.5	5032	1.24E-01	3.80E-04	1.14E-04
52.5	6053	1.32E-01	4.05E-04	1.22E-04

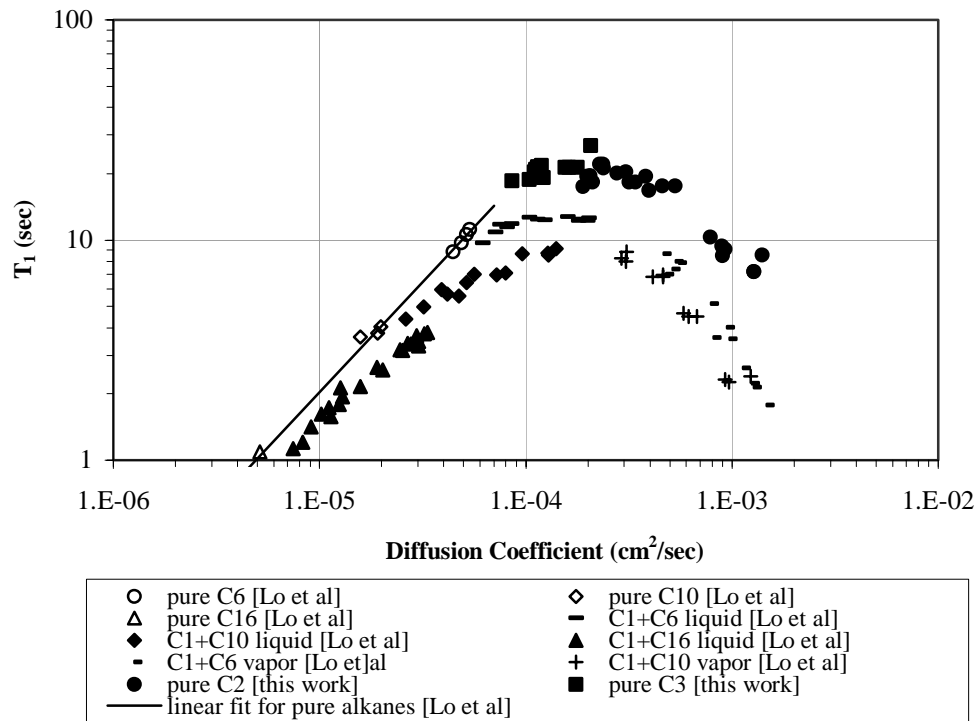


Figure 10 T_1 dependence on diffusion coefficient

Diffusion coefficient dependence on viscosity/temperature was plotted in Figure 11^{3, 9-11}. According to the Stokes-Einstein equation,⁸ diffusion coefficient D has the following relationship with viscosity η and temperature T .

$$D = \frac{kT}{4\pi\sigma\eta} \quad (5)$$

where σ is characteristic length of the intermolecular potential and k is Boltzmann constant.

This relationship is applicable to all of the alkane mixtures and pure alkanes. Diffusion coefficients are proportional to T/η , $D=5.05 \times 10^{-8} \times T/\eta$, where D is expressed in cm^2/sec , viscosity is expressed in cP and T is absolute temperature in K.³ The literature diffusion coefficient data for ethane and propane are also plotted here⁹⁻¹¹. The data from this work agree with the literature data. The data of ethane and propane are consistent with the Stokes-Einstein equation.

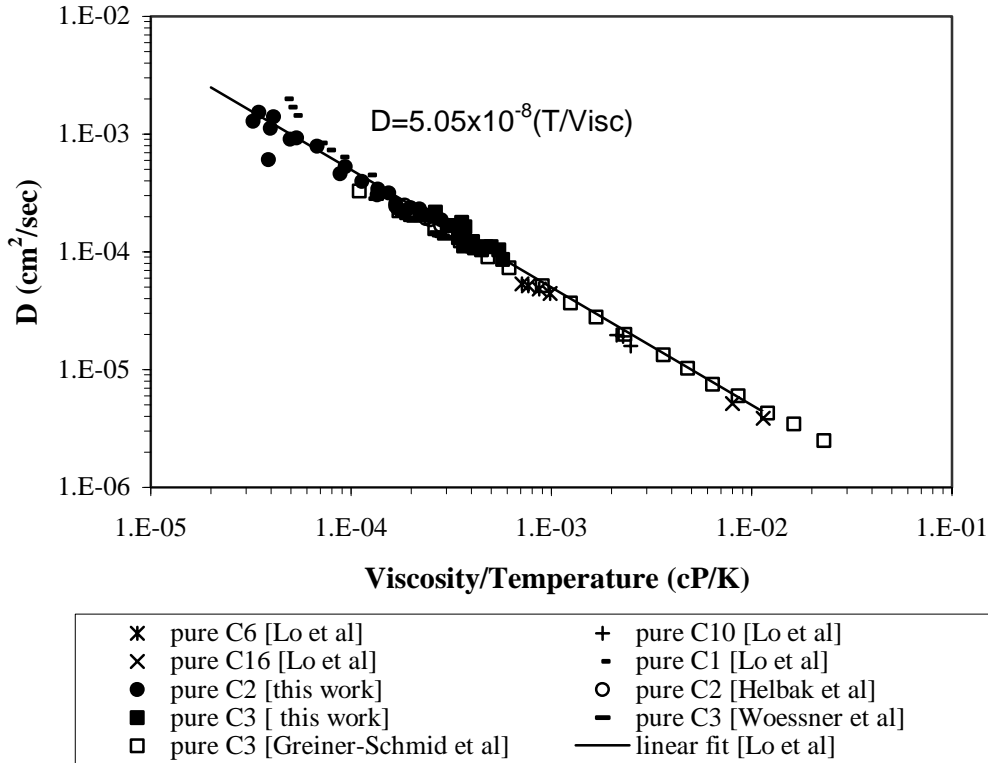


Figure 11 Diffusivity dependence on η/T for pure alkanes

IV. Conclusions

T_1 and diffusion coefficients were measured for ethane and propane. The relationships between transport properties, temperature and relaxation times were

observed. The linear relationship between T_1 and viscosity/temperature for pure alkanes does not hold for ethane and propane. T_1 of ethane and propane does not depend linearly on the diffusion coefficient. The result for the diffusion coefficient agrees with the literature data and is consistent with the Stokes-Einstein equation.

V. References

1. Gerritsma, C. J., Oosting, P. H. and Trappeniers, N. J., "Proton-Spin-Lattice Relaxation and Self-Diffusion in Methanes", *Physica*, Vol. 51, p. 365-417 (1971).
2. Muller, B. H. and Noble, J. D., "Proton Spin-Lattice Relaxation in Pure Liquid Ethane and Some of Its Deuterated Modifications" *J. Chem. Phys.*, p.777-779 (1962).
3. Lo, S. W., "Correlations of NMR Relaxation Time with Viscosity/Temperature, Diffusion Coefficient and Gas/Oil Ratio of Methane-Hydrocarbon Mixtures," Ph.D. dissertation, Rice University, Houston, Texas (1999).
4. Zega, J. A., "Spin-Lattice Relaxation in Pure and Mixed Alkanes and Their Correlation with Thermodynamic and Macroscopic Transport Properties," M.S. thesis, Rice University, Houston, Texas (1987).
5. Zega, J. A., "Spin-Lattice Relaxation in Normal Alkanes at Elevated Pressures," Ph.D. dissertation, Rice University, Houston, Texas (1990).
6. Kashaev, S. K. G., Le, B., and Zinyatov, M. Z., "Proton Spin-Lattice Relaxation, Viscosity, and Vibration of Molecules in the Series of n-Paraffins", *Doklady Akademii Nauk SSSR*, Vol. 157, No. 6, p.1438-1440 (1964).
7. Etesse, P., "High Pressure NMR Study of CO₂ and Supercritical CO₂-n-Hexadecane Mixtures", Ph.D. dissertation, Rice University, Houston, Texas (1992).
8. Abragam, A., *The Principles of Nuclear Magnetism*, Oxford University Press, London, 1961.
9. Helbak, M., Hafskjold, B., Dysthe, D. K. and Sorland, G. H., "Self-Diffusion Coefficients of Methane or Ethane Mixtures with Hydrocarbons at High Pressure by NMR", *J. Chem. Eng. Data*, Vol. 41, p. 98-603 (1996).
10. Woessner, D. E., Snowden, B. S., JR., George, R. A., and Melrose, J. C., "Dense Gas Diffusion Coefficients for the Methane-Propane System", *I & EC Fundamentals*, Vol. 8, No. 4, p. 779-786 (1969).
11. Greiner-Schmid, A., Wappmann, S., Has, M., and Ludemann, H.-D., "Self-Diffusion in the Compressed Fluid Lower Alkanes: Methane, Ethane, and Propane", *J. Chem. Phys.*, Vol. 94, p. 5643-5649 (1991).
12. Diller, D. E., "Measurements of the Viscosity of Saturated and Compressed Liquid Propane", *J. Chem. Eng. Data*, Vol. 27, p. 240-243 (1982).
13. Hildebrand, J. H., "Viscosity of Dilute Gases and Vapors", *Proc. Natl. Acad. Sci. USA*, Vol. 73, No. 12, p. 4302-4303 (1976).
14. Kestin, J., Khalifa, H. E., and Wakeham, W. A., "The Viscosity of Five Gaseous Hydrocarbons", *J. Chem. Phys.*, Vol. 66, No. 3, p. 1132-1134 (1977).

15. Vogel, E., "The Viscosity of Gaseous Propane and Its Initial Density Dependence", *Int. J. Thermophys.*, Vol. 16, No. 6, p. 1335-1351 (1995).
16. Starling, K. E., Eakin, B. E., and Ellington, R. T., "Liquid, Gas and Dense-Fluid Viscosity of Propane", *A.I.Ch.E. J.*, Vol. 6, No. 3, p. 438-442 (1960).
17. Giddings, J. G., Kao, J. T.F., and Kobayashi, R., "Development of a High-Pressure Capillary-Tube Viscometer and Its Application to Methane, Propane, and Their Mixtures in the Gaseous and Liquid Regions", *J. Chem. Phys.*, Vol. 45, No. 2, p. 578-586 (1965).
18. Harris, R. K., *Nuclear Magnetic Resonance Spectroscopy*, Chapt. 4, Bath Press, Bath, 1986.
19. Tanner, J. E. and Stejskal, E. O., "Restricted Self-Diffusion of Protons in Colloidal Systems by the Pulsed-Gradient Spin-Echo Method", *J. Chem. Phys.*, Vol. 49, No. 4, p. 1768-1777 (1968).
20. National Institute of Standards and Technology, "NIST Thermophysical Properties of Hydrocarbon Mixtures Database (SUPERTRAPP)," Version 3.0 (1999).
21. Eakin, B. E., Starling, K. E., Dolan, J. P., and Ellington, R. T., "Liquid, Gas and Dense Fluid Viscosity of Ethane," *J. Chem. Eng. Data*, Vol. 7, p. 33-36 (1962).

Interpretation of Spin-Lattice Relaxation in CH₄, C₂H₆ and CH₄ Mixtures

Ying Zhang, George J. Hirasaki, Riki Kobayashi, and Waylon House
Rice University, Houston, Texas

Abstract

The relationship between $T_{1,\text{sr}}$ and density, temperature and viscosity was investigated for methane and ethane. The proton spin rotation interaction constants have first been calculated for ethane. The proton relaxation times were calculated and compared with the experimental data for ethane. Spin rotation interaction is shown to be the main contribution in gaseous ethane. At liquid densities, intra- and intermolecular dipole-dipole interactions and spin rotation interaction all have significant contributions. The general mixing rule for T_1 was proposed and was then tested for CH₄-CO₂, CH₄-N₂, CH₄-He, CH₄-Ne and CH₄-Ar gas mixtures.

I. Theory for spin relaxation

In general, three interactions, viz. the intra- and intermolecular dipole-dipole interactions and the spin rotation interaction contribute to the total relaxation rate for most spin $\frac{1}{2}$ nuclei. If these interactions are independent, the total relaxation rate may be given by ^{1,2}

$$\frac{1}{T_1} = R = R_{\text{intra}} + R_{\text{inter}} + R_{\text{sr}} \quad (1)$$

where R_{intra} is the relaxation rate by intramolecular dipole-dipole interaction, R_{inter} is the relaxation rate by intermolecular dipole-dipole interaction, and R_{sr} is the relaxation rate by spin rotation interaction.

The theoretical calculation of different contributions will be briefly discussed in the followings.

1.1. Intermolecular dipole-dipole interaction

Dipole-dipole interaction mechanism is caused by the interaction of the magnetic dipoles of the nuclei. For the interaction with nuclei in neighboring molecules, it is intermolecular dipole-dipole interaction. The relaxation will in general arise from the relative translational motion of the molecules.

McConnell ¹ described the molecular motion with a Langevin equation assuming that the molecular motion can be described as translational and rotational diffusions and then derived the relation for dipole-dipole interaction

$$\frac{1}{T_1} = I(I+1) \left\{ \frac{4}{3} j(\omega_0) + \frac{16}{3} j(2\omega_0) \right\} \quad (2)$$

where I is spin quantum number, ω_0 is the Larmor angular frequency, and $j(\omega)$ is the spectral density.

The evaluation of the spectral density will depend on whether the dipole-dipole interaction is intermolecular or intramolecular, and also on the particular model chosen to describe the thermal motion. For intermolecular dipole-dipole interaction, Brownian motion model in the extreme narrowing limit gives ¹

$$\frac{1}{T_{1,\text{inter}}} = R_{\text{inter}} = \frac{8\pi n \nu \gamma^4 \hbar^2 I(I+1)}{15D\sigma} \quad (3)$$

where γ is gyromagnetic ratio, \hbar is Plank's constant, n is the number density, ν is the number of resonant nuclei in a given molecule, σ is the molecular diameter, and D is translational diffusion coefficient.

1.2. Intramolecular dipole-dipole interaction

Intramolecular dipole-dipole interaction mechanism is due to the interaction of nuclei in the same molecule. If the molecule is regarded as rigid, the relaxation results from the rotational motion of the molecule.

It is assumed that the autocorrelation function is exponential. If the rotational molecular motion can be described by the diffusion equation, Equation (2) in the extreme narrowing limit will be expressed as ¹

$$\frac{1}{T_{1,\text{intra}}} = R_{\text{intra}} = 2I(I+1) \gamma^4 \hbar^2 \tau_\theta \sum_{j=1} r_{ij}^{-6} \quad (4)$$

where r_{ij} is distance between two nuclei in the same molecule, and τ_θ is molecular reorientation correlation time.

Numerous studies of rotational molecular motion have shown that reorientational correlation time can be given by the Stokes-Einstein-Debye equation ⁴⁻⁹

$$\tau_\theta = A_1 \eta / T + \tau^0 \quad (5)$$

where η is the viscosity, T is the temperature, τ^0 is the zero-viscosity intercept, and A_1 is related to the volume of the rotating particle and the drag that the particle experiences from the surrounding fluid. Alm *et al.*⁶⁻⁷ suggested that the intercept was related to free rotation and that it could be described as

$$\tau^0 = \tau_{\text{FR}} = \left(\frac{2\pi}{9} \right)^{1/2} \left(\frac{I_{\text{av}}}{kT} \right)^{1/2} \quad (6)$$

where k is Boltzmann constant and I_{av} is given by

$$\frac{1}{I_{\text{av}}} = \frac{1}{3} \left(\frac{2}{I_{\perp}} + \frac{1}{I_{\parallel}} \right) \quad (7)$$

I_{\parallel} , I_{\perp} are moments of inertia of the molecule along parallel and perpendicular axes.

Substituting Equation (5), Equation (6) and Equation (7) into Equation (4), we obtain

$$\frac{1}{T_{1,\text{intra}}} = R_{\text{intra}} = 2I(I+1)\gamma^4\hbar^2 \left[A_1 \frac{\eta}{T} + \left(\frac{2\pi}{9} \right)^{1/2} \left(\frac{1}{kT} \cdot \frac{3I_{\parallel} I_{\perp}}{2I_{\parallel} + I_{\perp}} \right)^{1/2} \right] \sum_{j=1} r_{ij}^{-6} \quad (8)$$

1.3. Spin rotation interaction

It has been shown that spin rotation relaxation is the dominant mechanism for spin $\frac{1}{2}$ in a gas. The spin rotation interaction is due to magnetic fields generated at a nucleus by the motion of a molecular magnetic moment which arises from the electron distribution in a molecule. Molecular collisions cause the magnetic moment to fluctuate. This can result in fluctuating magnetic fields which are felt by the nucleus. The magnitude of the effect is proportional to the rotational velocity and inversely proportional to the moment of inertia. Thus spin rotation interaction will be the strongest in small spherical molecules. The Hamiltonian for the interaction of molecular and nuclear magnetic moment is ^{1, 2}

$$H_{\text{sr}} = -h\mathbf{I} \cdot \mathbf{C} \cdot \mathbf{J} \quad (9)$$

where \mathbf{C} is the spin rotation coupling tensor, \mathbf{I} is the spin angular momentum operator of the resonant spin, and \mathbf{J} is the molecular rotational angular momentum of the molecule. For symmetric top molecules, the spin rotation coupling tensor is a symmetric tensor.

Theoretical predictions concerning spin rotation interaction can be categorized to two cases, the kinetic model for low densities and the diffusion model for high densities. The two models differ in the assumed model for the rotation molecular motion.

1.3.1. Kinetic model

In dilute gases, T_1 can be connected to the thermal average of the binary collision cross sections for angular momentum transfer for spin rotation interaction. The kinetic model can adequately describe spin rotation interaction in dilute gases. Gordon¹⁰ developed the kinetic model of spin rotation interaction for the case of linear molecules. Then Bloom *et al.*^{12, 13} extended theoretical treatment to spherical and symmetric top molecules. The basic assumptions underlying the kinetic model are as follows

- (a) “High frequency” transitions associated with changes in the energy of rigid rotation and centrifugal distortion are neglected.
- (b) The rotational Larmor period is much longer than interaction times during which the molecules reorient.
- (c) The free molecule correlation functions (in the absence of collisions) are independent of time. The effect of molecular collisions is to limit the lifetime of the molecule in any state and to cause the free molecule correlation functions to decay to zero exponentially.
- (d) The oscillating terms in the free molecule correlation functions are negligible.
- (e) The rotational angular momentum J_l and the rotation matrix for frame transformation D_{0-1} ² are statistically dependent for the dilute gases.

For symmetric top molecules with the resonant nuclei on the principal symmetry axis (*e. g.*, ¹³C in ethane), the relaxation time in the extreme narrowing limit may be expressed as

$$\begin{aligned} \frac{1}{T_{1, \text{sr}}} = 4\pi^2 \left\{ \frac{2}{3} C_{\text{av}}^2 \langle J(J+1) \rangle^{J,K} \tau_J - \frac{4}{9} \Delta C C_{\text{av}} \langle 2K^2 - J(J+1) \rangle^{J,K} \tau_{12}' \right. \\ \left. + \frac{2}{27} (\Delta C)^2 \left\langle \frac{[3K^2 - J(J+1)]^2}{J(J+1)} \right\rangle^{J,K} \tau_{12} \right\} \end{aligned} \quad (10)$$

where J, K are rotational quantum numbers, τ_J is the correlation time related with the angular momentum operator \mathbf{J} , τ_{12}' is the correlation time related with the tensor of rank one formed by the product of \mathbf{J} and the spherical harmonic $Y_{2m}(\Omega)$, τ_{12} is the correlation time related with the cross term between \mathbf{J} and $\mathbf{J}Y_{2m}$, and

$$C_{\text{av}} = \frac{1}{3}(C_{\parallel} + 2C_{\perp}) \quad (11)$$

$$\Delta C = C_{\perp} - C_{\parallel} \quad (12)$$

where C_{\parallel} , C_{\perp} are spin rotation constants describing the coupling of the nuclear and molecular angular momenta along parallel and perpendicular axes. Armstrong *et al.*^{14, 15} calculated the rotational averages in Equation (10) using the method of Birnbaum in terms of α and γ . α and γ are defined as

$$\alpha = \frac{\hbar^2}{2I_{\perp}kT} \quad (13)$$

$$y = \left(1 - \frac{I_{\parallel}}{I_{\perp}}\right)^{1/2} \quad (14)$$

Then we obtain

$$\begin{aligned} \frac{1}{T_{1,\text{sr}}} = \frac{4\pi^2}{\alpha} & \left\{ \left(1 - \frac{y^2}{3}\right) C_{\text{av}}^2 \tau_J + \frac{4}{9} y^2 \Delta C C_{\text{av}} \tau'_{12} \right. \\ & \left. + (\Delta C)^2 \left[9 \left(\frac{1-y^2}{y^2} \right)^2 \left(-1 - \frac{1}{3} y^2 + s \right) - 1 + \frac{5}{3} y^2 \right] \tau_{12} \right\} \end{aligned} \quad (15)$$

where

$$\begin{aligned} s &= \frac{1}{2y} \ln \left(\frac{1+y}{1-y} \right) \quad \text{for } I_{\perp} > I_{\parallel} \\ &= \frac{1}{|y|} \tan^{-1}|y| \quad \text{for } I_{\perp} < I_{\parallel} \end{aligned} \quad (16)$$

The averages in Equation (10) are inversely proportional to α and α is inversely proportional to temperature. It turns out that the averages in Equation (10) are proportional to temperature.

Armstrong *et al.*¹⁵ investigated the kinetic model for the resonant nuclei off the symmetry axis of the symmetric-top molecules (*e. g.*, ¹H in ethane). In this case, the \mathbf{C} tensor is not diagonal and can be expressed by Equation (37) in the molecular frame. The complete Hamiltonian for the spin rotation interaction is expressed as

$$H_{\text{sr}} = -\hbar \mathbf{I}^A \cdot \mathbf{C}^A \cdot \mathbf{J} - \frac{1}{6} \hbar \mathbf{I}^{E_1} \cdot \mathbf{C}^{E_1} \cdot \mathbf{J} - \frac{1}{2} \hbar \mathbf{I}^{E_2} \cdot \mathbf{C}^{E_2} \cdot \mathbf{J} \quad (17)$$

where

$$\mathbf{C}^A = \frac{1}{2} \begin{pmatrix} C_{xx} + C_{yy} & \dots & 0 & \dots & 0 \\ 0 & \dots & C_{xx} + C_{yy} & \dots & 0 \\ 0 & \dots & 0 & \dots & 2C_{zz} \end{pmatrix} \quad (18)$$

$$C^{E_1} = \frac{3}{2} \begin{pmatrix} C_{xx} - C_{yy} & \dots & 0 & \dots & 0 \\ 0 & \dots & -(C_{xx} - C_{yy}) & \dots & 0 \\ 0 & \dots & 0 & \dots & 0 \end{pmatrix} \quad (19)$$

$$C^{E_2} = -\frac{\sqrt{3}}{2} \begin{pmatrix} 0 & \dots & C_{xx} - C_{yy} & \dots & 0 \\ C_{xx} - C_{yy} & \dots & 0 & \dots & 0 \\ 0 & \dots & 0 & \dots & 0 \end{pmatrix} \quad (20)$$

with C_{xx} , C_{yy} , C_{zz} the diagonal components of the spin rotation tensor.

Armstrong¹⁵ argued that it was reasonable to neglect the contribution of the last two terms to Hamiltonian. Equation (15) and Equation (16) can also be used for the resonant nuclei off the symmetry axis of the symmetric-top molecules. However, for the resonant nuclei off the symmetry axis, Equation (12) becomes

$$\Delta C = (C_{\perp} - C_{\parallel}) \left(1 - \frac{3}{2} \sin^2 \theta\right) \quad (21)$$

where θ is the angle defined by Equation (38).

For spherical top molecules, y is equal to 0 and τ_J , τ_{12} , and τ_{12} are equal. Equation (15) simplifies to

$$\frac{1}{T_{1,\text{sr}}} = \frac{8\pi^2 I_{\text{av}} kT}{\hbar^2} \left(C_{\text{av}}^2 + \frac{4}{45} \Delta C^2 \right) \tau_J \quad (\text{spherical top molecules}) \quad (22)$$

For linear molecules, only perpendicular component of C_{\perp} is nonzero. Thus C tensor reduces to a scalar and Gordon's Kinetic theory¹⁰ gives

$$\frac{1}{T_{1,\text{sr}}} = \frac{16\pi^2 C_{\perp}^2 I_{\text{av}} kT}{3\hbar^2} \tau_J \quad (\text{linear molecules}) \quad (23)$$

τ_J represents the average time between collisions that cause angular momentum transfer and is given by Gordon's theory¹⁰ as follows

$$\tau_J = (n\bar{v}\sigma_J)^{-1} = \frac{1}{n\sigma_J} \sqrt{\frac{\pi\mu}{8kT}} \quad (24)$$

where \bar{v} is the mean relative velocity $(8kT/\pi\mu)^{1/2}$, μ is the reduced mass for a collision pair of molecules, and σ_J is the cross section for transfer of angular momentum by a collision. The reduced mass μ is given by

$$\frac{1}{\mu} = \frac{1}{m_1} + \frac{1}{m_2} \quad (25)$$

where m_1 and m_2 are the mass of two colliding molecules respectively.

The cross section $\sigma_J(T)$ is interpreted classically as¹⁰

$$\sigma_J(T) = \frac{1}{4I_{\text{av}}kT} \int_0^\infty \langle (\Delta J)^2 \rangle 2\pi b db \quad (26)$$

where ΔJ is the change in the rotational angular momentum vector of the molecule by a collision and $\langle \rangle$ denotes the average over the initial distribution of internal states before a collision and the initial distribution of relative velocities. If the collision integral is temperature independent, the cross section is inversely proportional to temperature. Then the angular momentum correlation time τ_J is expected to be proportional to $T^{1/2}$. It is assumed that the molecular motion is governed by a single correlation time. Substituting Equation (24) and Equation (26) into Equation (15), we obtain

$$\frac{T_{1,\text{sr}}}{n} = \frac{\hbar^2}{8\pi^2 C_{\text{eff}}^2 I_{\text{av}} I_{\perp} k^2} \cdot \sqrt{\frac{k}{2\pi\mu}} \cdot \left(\int_0^\infty \langle (\Delta J)^2 \rangle 2\pi b db \right) \cdot \frac{1}{T^{3/2}} \quad (27)$$

with

$$C_{\text{eff}}^2 = \left(1 - \frac{y^2}{3}\right) C_{\text{av}}^2 + \frac{4}{9} y^2 \Delta C C_{\text{av}} + (\Delta C)^2 \left[9 \left(\frac{1-y^2}{y^2} \right)^2 \left(-1 - \frac{1}{3} y^2 + s \right) - 1 + \frac{5}{3} y^2 \right] \quad (28)$$

and we would expect that T_1/n has a $T^{3/2}$ temperature dependence for the symmetrical top molecules. Apparently, this conclusion is also valid for spherical top and linear molecules.

At dense gases, the assumptions underlying the kinetic model may not be valid. We may estimate the main correction at dense gases by analogy with Enskog's theory of transport in dense gases.¹¹ For nuclear spin relaxation in compressed polyatomic gases, the collision frequency effect is important¹¹. Then the only modification is the replacement of n with $ng(\sigma)$ where $g(\sigma)$ is Enskog's correction to the collision frequency. The radial distribution function $g(\sigma)$ can be given by Carnahan-Starling equation^{16, 17}:

$$g(\sigma) = \frac{(1 - 0.5\xi)}{(1 - \xi)^3} \quad (29)$$

where $\xi = b/4V$ for a molar volume V and $b = 2\pi N_A \sigma^3 / 3$ (N_A is the Avogadro number). In dense fluids, Equation (24) becomes

$$\tau_J = [ng(\sigma)\bar{v}\sigma_J]^{-1} = \frac{1}{n\sigma_J} \cdot \frac{(1-\xi)^3}{(1-0.5\xi)} \cdot \sqrt{\frac{\pi\mu}{8kT}} \quad (30)$$

Since $g(\sigma)$ is independent of temperature, τ_J is still proportional to $T^{1/2}$ at dense gases. In general, we would expect

$$\frac{T_{1,\text{sr}}}{n} \propto T^{-3/2} \quad (31)$$

in the kinetic model.³⁴⁻³⁹

1.3.2. Diffusion model

The binary collision theory may not be useful in treating dense gases or liquids. Calculations of T_1 in dense fluids have often been based upon the diffusion model which describe the rotational motion of molecules with a diffusion equation.²⁰⁻²⁴ The diffusion process can be regarded as a random walk over points in phase space caused by collisions interrupting the free motion of the molecules. The diffusion model is appropriate when the angular momentum correlation time is small compared to the mean period of rotation of the free rotor.

The diffusion model for the spin rotation contribution to T_1 derived by Wang *et al.*²⁰⁻²⁴ will be summarized in the next paragraphs. In the liquid, the anisotropic intermolecular interactions are large. The restriction (e) in the kinetic model might be removed and the assumption of statistical independence may be reasonable for the liquid. The correlation functions can be evaluated by a Langevin equation for the molecular angular velocity. If the resonant nuclei are on the symmetry axis of symmetrical top molecules, the coordinate system chosen for diagonalizing the diffusion tensor will simultaneously diagonalize the \mathbf{C} tensor. The expression for spin rotation contribution to the relaxation time is given as

$$\begin{aligned} \frac{1}{T_{1,\text{sr}}} = R_{\text{sr}} = & \frac{8\pi^2}{3\hbar^2} \int_0^\infty dt \cos(\omega_0 t) \left\{ e^{-D_\perp t} C_\parallel \langle J_z(0)J_z(t) \rangle \right. \\ & \left. + e^{-2(D_\parallel + D_\perp)t} C_\perp^2 \langle J_x(0)J_x(t) + J_y(0)J_y(t) \rangle \right\} \end{aligned} \quad (32)$$

where D_\parallel , D_\perp are rotational diffusion constants parallel and perpendicular to the symmetry axis. Basically, the angular momentum correlation function is expected to decay over a time short to the Larmor period. It is reasonable for us to assume

$$\langle J_i(0)J_i(t) \rangle = I_i^2 \langle \omega_i^2 \rangle e^{-t/\tau_{Ji}} = kTI_i e^{-t/\tau_{Ji}} \quad i=x, y, z \quad (33)$$

where ω is the component of the angular velocity along the i -th principal axis, I_i is the component of moment of inertia along the i -th principal axis and τ_{Ji} is the angular momentum correlation time along the i -th principal axis and is given by

$$\tau_{Ji} = \frac{1}{\langle \omega_i^2 \rangle} \int_0^\infty \langle \omega_i(0)\omega_i(t) \rangle dt \quad (34)$$

Substituting Equation (33) into Equation (32), we obtain the expression for the relaxation time due to spin rotation interaction in the extreme narrowing limit as

$$\frac{1}{T_{1,\text{sr}}} = \frac{8\pi^2 kT}{3\hbar^2} \left(I_{\parallel}^2 C_{\parallel}^2 \left(\frac{\tau_{J\parallel}}{1 + 2D_{\perp}\tau_{J\parallel}} \right) + 2I_{\perp}^2 C_{\perp}^2 \left(\frac{\tau_{J\perp}}{1 + (D_{\perp} + D_{\parallel})\tau_{J\perp}} \right) \right) \quad (35)$$

where $\tau_{J\parallel}$, $\tau_{J\perp}$ are angular momentum correlation times along parallel and perpendicular axes.

Equation (35) reduces to

$$\frac{1}{T_{1,\text{sr}}} = \frac{8\pi^2 kT}{3\hbar^2} (I_{\parallel}^2 C_{\parallel}^2 \tau_{J\parallel} + 2I_{\perp}^2 C_{\perp}^2 \tau_{J\perp}) \quad (36)$$

in the limit $(D_{\perp} + D_{\parallel})\tau_{J\perp} \ll 1, D_{\perp}\tau_{J\parallel} \ll 1$.

Equation (35) and (36) may not be applied to the resonant nuclei off the symmetry axis (e. g., ^1H in ethane). Wang²⁰ has derived the diffusion model for the spin rotation contribution to T_1 for the resonant nuclei off the symmetry axis. He first assumes that the C-H bond in a molecule such as ethane lies along the z axis with the proton along the z axis at which the \mathbf{C} tensor for the proton is diagonalized, and he then relocates the proton to its final position at the y axis on the x-y plane by rotation about the carbon through an angle θ . As a result, the \mathbf{C} tensor element for the proton after the transformation is given by

$$\mathbf{C} = \begin{pmatrix} C_{\perp} - \Delta C \sin^2 \theta & \dots & 0 & \dots & \Delta C \sin \theta \cos \theta \\ 0 & \dots & C_{\perp} & \dots & 0 \\ \Delta C \sin \theta \cos \theta & \dots & 0 & \dots & C_{\parallel} + \Delta C \sin^2 \theta \end{pmatrix} \quad (37)$$

$$\theta = \frac{180^\circ - \angle H - C - C}{2} \quad (38)$$

Wang then obtains the expression for spin rotation contribution to the relaxation time

$$\frac{1}{T_{1,\text{sr}}} = R_{\text{sr}} = \frac{8\pi^2 kT}{3\hbar^2} \left\{ I_{\parallel} (C_{\parallel} + \Delta C \sin^2 \theta)^2 \frac{\tau_{J\parallel}}{1 + 2D_{\perp} \tau_{J\parallel}} + I_{\perp} (\Delta C)^2 \sin^2 \theta \cos^2 \theta \left[\frac{\tau_{J\perp}}{1 + 2D_{\perp} \tau_{J\perp}} + \frac{\tau_{J\parallel}}{1 + (D_{\perp} + D_{\parallel}) \tau_{J\parallel}} \right] + I_{\perp} [(C_{\perp} - \Delta C \sin^2 \theta)^2 + C_{\perp}^2] \frac{\tau_{J\perp}}{1 + (D_{\perp} + D_{\parallel}) \tau_{J\perp}} \right\} \quad (39)$$

which reduces to

$$\frac{1}{T_{1,\text{sr}}} = R_{\text{sr}} = \frac{8\pi^2 kT}{3\hbar^2} \left\{ I_{\parallel} (C_{\parallel} + \Delta C \sin^2 \theta)^2 \tau_{J\parallel} + I_{\perp} (\Delta C)^2 \sin^2 \theta \cos^2 \theta [\tau_{\perp} + \tau_{J\parallel} / (1 + D_{\parallel} \tau_{J\parallel})] + I_{\perp} [(C_{\perp} - \Delta C \sin^2 \theta)^2 + C_{\perp}^2] \tau_{J\perp} \right\} \quad (40)$$

in the limit $D_{\perp} \tau_{J\perp} \ll 1, D_{\perp} \tau_{J\parallel} \ll 1$. Note that Equation (40) reduces to Equation (36) for $\theta=0$.

For spherical top molecules, Equation (36) reduces to

$$\frac{1}{T_{1,\text{sr}}} = \frac{8\pi^2 I_{\text{av}} kT}{\hbar^2} \left(C_{\text{av}}^2 + \frac{2}{9} \Delta C^2 \right) \tau_J \quad (\text{spherical top molecules}) \quad (41)$$

For linear molecules, T_1 may be deduced from Equation (41) by putting C_{\parallel} equal to 0. That is

$$\frac{1}{T_{1,\text{sr}}} = \frac{16\pi^2 C_{\perp}^2 I_{\text{av}} kT}{3\hbar^2} \tau_J \quad (\text{linear molecules}) \quad (42)$$

From hydrodynamics theory,^{53, 54} the angular momentum correlation time may be related to viscosity η as following

$$\tau_{Ji} = \frac{I_i}{8\pi a^3 \eta} \kappa \quad i=x, y, z \quad (43)$$

where a is the molecular radius and κ is the correction factor for slip boundary conditions compared with stick boundary conditions^{18, 19}. In general, the theoretical prediction using slip boundary conditions may agree well with the experimental measurement for small molecular fluids.

From substitution of Equation (43) into Equation (40), we obtain

$$\frac{1}{T_{1,\text{sr}}} = R_{\text{sr}} = \frac{\pi \kappa k T}{3 \hbar^2 a^3 \eta} \left\{ I_{\parallel}^2 (C_{\parallel} + \Delta C \sin^2 \theta)^2 + I_{\perp} (\Delta C)^2 \sin^2 \theta \cos^2 \theta [I_{\perp} + I_{\parallel} / (1 + D_{\parallel} \tau_J)] \right. \\ \left. + I_{\perp}^2 [(C_{\perp} - \Delta C \sin^2 \theta)^2 + C_{\perp}^2] \right\} \quad (44)$$

It is to be expected that

$$T_{1,\text{sr}} \propto \frac{\eta}{T} \quad (45)$$

if the diffusion model is appropriate.

Table 1 summarizes the results for spherical top molecules and linear molecules by two models. Note that for spherical top molecules the coefficient for “ ΔC^2 ” term given by the kinetic model differs from that given by the diffusion model by a factor of 2/5. Bloom’s explanation¹² is that a factor of 1/5 is accounted for by dropping of the oscillating contribution to correlation functions and that the remaining factor of 2 is due to the fact that J_1 and $D_{0,1}$ are statistically dependent for the gases. It might be noted that both models lead to the same result in the limit of linear molecules. In the diffusion model, Equation (42) can be obtained from Equation (41). However, we cannot derive Equation (23) directly from Equation (22).

Table 1 Relaxation times by spin rotation interaction

	Kinetic model	Diffusion model
Spherical top	$\frac{1}{T_{1,\text{sr}}} = \frac{8\pi^2 I_{\text{av}} k T}{\hbar^2} \left(C_{\text{av}}^2 + \frac{4}{45} \Delta C^2 \right) \tau_J$	$\frac{1}{T_{1,\text{sr}}} = \frac{8\pi^2 I_{\text{av}} k T}{\hbar^2} \left(C_{\text{av}}^2 + \frac{2}{9} \Delta C^2 \right) \tau_J$
Linear	$\frac{1}{T_{1,\text{sr}}} = \frac{16\pi^2 C_{\perp}^2 I_{\text{av}} k T}{3\hbar^2} \tau_J$	$\frac{1}{T_{1,\text{sr}}} = \frac{16\pi^2 C_{\perp}^2 I_{\text{av}} k T}{3\hbar^2} \tau_J$

II. Mixing rule for T_1

A mixing rule is developed for T_1 in the binary mixture with components A and B. The resonant nuclei may be ^1H or ^{13}C . For A-B mixtures, there may be two contributions to T_1 , one from resonant nuclei of A and the other from resonant nuclei of B. The log mean T_1 may be described as

$$\text{Log}(T_{1,\text{logmean}}) = F_A \text{Log}(T_{1,A}) + F_B \text{Log}(T_{1,B}) \quad (46)$$

where F_A is the resonant nucleus fraction of A, F_B is the resonant nucleus fraction of B, and $T_{1,A}$ and $T_{1,B}$ are the individual relaxation times of A and B in the mixture. In general, relaxation times of A and B can be given by Equation (1).

The intermolecular dipole-dipole relaxation rate can be given by Equation (3). In the A-B mixture, ν can be calculated as

$$\nu = \nu_A x_A + \nu_B x_B \quad (47)$$

where x_A , x_B are the mole fractions of A and B in the mixture respectively and ν_A , ν_B are the number of resonant nuclei in A and B respectively. The molecular weight MW of the mixture can be calculated as

$$MW = MW_A x_A + MW_B x_B \quad (48)$$

where MW_A , MW_B are the molecular weight of A and B respectively.

The intramolecular dipole-dipole interaction relaxation time can be given by Equation (4). The medium effect may be included in the viscosity term.

It is assumed that the relaxation of both A and B in the mixture may be described by the kinetic model. The relaxation by the spin rotation mechanism for A is caused by A-A collisions and by A-B collisions. It has been theoretically¹⁰ and empirically³³ established that these effects are additive.

$$T_{1, sr, A} = \rho_A \left(\frac{T_{1,A}}{\rho} \right)_{A-A} + \rho_B \left(\frac{T_{1,A}}{\rho} \right)_{A-B} \quad (49)$$

where ρ , ρ_A , and ρ_B are the mass density.

Similar arguments can be made about the relaxation time of B and we obtain

$$T_{1, sr, B} = \rho_A \left(\frac{T_{1,B}}{\rho} \right)_{A-B} + \rho_B \left(\frac{T_{1,B}}{\rho} \right)_{B-B} \quad (50)$$

For the diffusion model of spin rotation interaction, the medium effect may be included in the viscosity term.

III. Applications of theory

3.1. Pure components

3.1.1. Proton spin rotation interaction in methane

Proton NMR relaxation times for methane have been measured by Gerritsma *et al.*²⁵⁻²⁷. The contribution of spin rotational interaction was extracted from proton T_1 data by assuming that gaseous methane relaxes only by spin rotation interaction. We analyzed proton $T_{1, \text{sr}}$ data using both the kinetic model and the diffusion model.

The molecular constants of methane are presented in Table 2.

Table 2 Molecular constants of methane

	value	reference
Moments of inertia (g.cm^2)	$I_A=I_B=I_C=5.33*10^{-40}$	28
^1H spin rotation constants (kHz)	$C_{\text{av}}=10.4$; $\Delta C = 18.5$	29
^{13}C spin rotation constants (kHz)	$C_{\text{av}}=15.94$; $\Delta C = 0$	33
Molecular diameter (10^{-10} m)	3.83	3

The numerical evaluation of Equation (22) and Equation (41) using the values in Table 2 for methane yields

$$\frac{1}{T_{1, \text{sr}}} (^1\text{H}) = 7.240 \times 10^8 T \tau_J \quad (\text{C1, km, cgs}) \quad (51)$$

$$\frac{1}{T_{1, \text{sr}}} (^1\text{H}) = 9.624 \times 10^8 T \tau_J \quad (\text{C1, dm, cgs}) \quad (52)$$

In this report, km represents the kinetic model, dm represents the diffusion model, and cgs represents cgs units. τ_J in the kinetic model can be evaluated by Equation (24). σ_J is available for methane in the literature and is listed in Table 4. So it is possible to predict the contribution of spin rotation interaction in methane by theoretical equations.

Figure 1 shows $T_{1, \text{sr}}/(\rho g(\sigma))$ vs. T plot for methane based on the kinetic model.²⁵ $T_{1, \text{sr}}$ is expressed in sec, ρ is expressed in g/cm^3 , and T is expressed in K. The theoretical prediction by the kinetic model compares well with experimental data. A plot of $T_{1, \text{sr}}$ vs. viscosity/temperature based on the diffusion model is shown in Figure 2.²⁵ It seems that the diffusion model fails to describe spin rotation interaction in methane. The kinetic model is a better model for describing spin rotation interaction in methane.

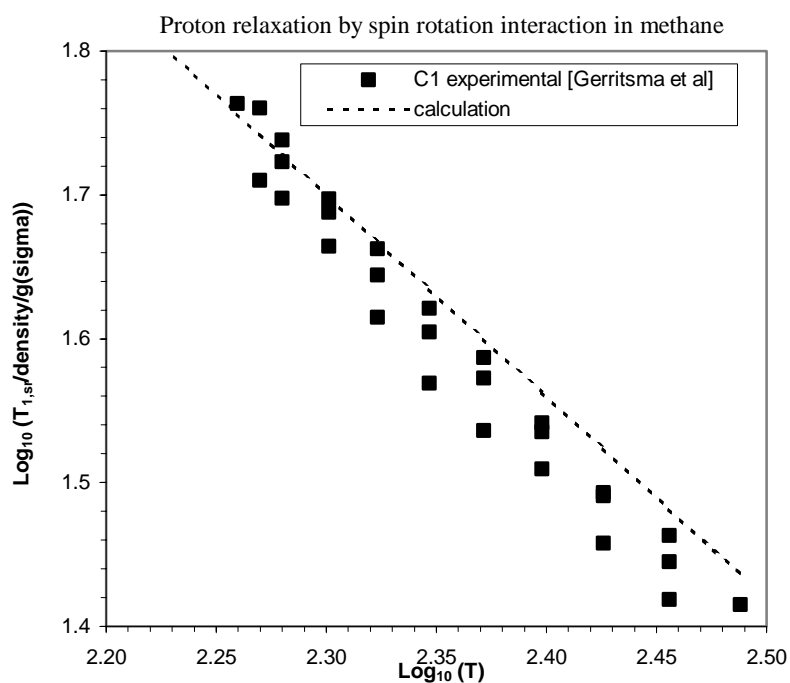


Figure 1 Proton $T_{1, sr} / (\rho g(\sigma))$ vs. T plot in methane based on the kinetic model

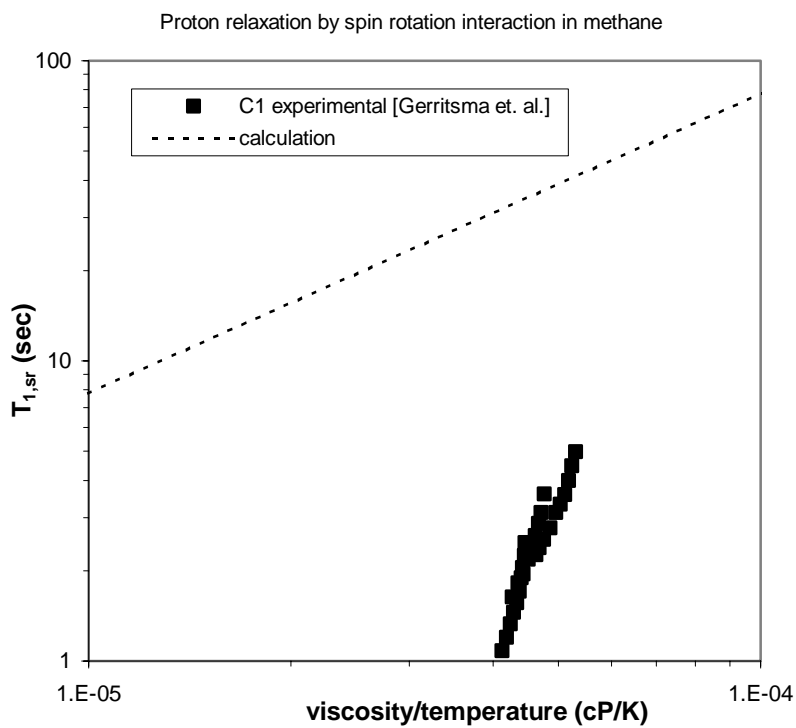


Figure 2 Proton $T_{1, sr}$ vs. η/T plot in methane based on the diffusion model

3.1.2. ^1H and ^{13}C spin rotation interaction in ethane

Proton NMR T_1 for ethane has been measured in the temperature range from 20 to 46 °C. The contribution of spin rotation interaction was extracted from proton T_1 data by assuming that gaseous ethane relaxes only by spin rotation interaction. Whittenburg *et al.*⁴⁰ measured the ^{13}C NMR T_1 for ethane in the temperature range from 172 to 323 K. The contribution of spin rotation interaction was extracted from ^{13}C T_1 data based on NOE measurements. So it is possible to analyze ^1H and ^{13}C $T_{1, \text{sr}}$ data in ethane using both the kinetic model and the diffusion model.

The spin rotation constants for the proton in ethane have not been reported. However, they can be estimated from the average paramagnetic shielding, σ'_p of the proton⁴⁹⁻⁵². We may calculate the spin rotational constants from the well-known relationship between the shielding and the spin rotational constants.^{49, 51}

$$\sigma'_p = \sigma'_{\text{total}} - \sigma'_d = \frac{2\pi}{3\hbar g} \frac{m_p}{m_e} (2C_{\perp} I_{\perp} + C_{\parallel} I_{\parallel}) \quad (53)$$

In this expression, g is the nuclear g factor, m_p and m_e are the mass of the proton and electron respectively, and σ'_d represents the atomic diamagnetic shielding, taken to be a constant 17.77 ppm.⁵⁰ for the proton. We then make use of the equations

$$\sigma'_p = \frac{1}{3} (2\sigma_{\perp} + \sigma_{\parallel}) \quad (54)$$

$$\Delta\sigma = \sigma_{\parallel} - \sigma_{\perp} \quad (55)$$

With $\sigma'_p = 12.2$ ppm and $\Delta\sigma = 2.02$ ppm for ethane,⁴⁸ we obtain values for σ_{\parallel} and σ_{\perp} . Now by equating Equation (53) and Equation (54), we obtain

$$\frac{1}{3} (2\sigma_{\perp} + \sigma_{\parallel}) = 6.23 \times 10^{36} (2C_{\perp} I_{\perp} + C_{\parallel} I_{\parallel}) \quad (56)$$

and therefore

$$\sigma_{\perp} = 3 \times 6.23 \times 10^{36} C_{\perp} I_{\perp} \quad (57)$$

and

$$\sigma_{\parallel} = 3 \times 6.23 \times 10^{36} C_{\parallel} I_{\parallel} \quad (58)$$

from which we obtain $C_{\perp} = 1.46\text{kHz}$ and $C_{\parallel} = 6.95\text{kHz}$.

The molecular constants of ethane are summarized in Table 3.

Table 3 Molecular constants of ethane

	value	reference
Moments of inertia (g.cm^2)	$I_A=1.04 \times 10^{-39}, I_B=I_C= 4.23 \times 10^{-39}$	45, 47
^1H spin rotation constants (kHz)	$C_{\parallel}=6.95; C_{\perp}=1.46$	this work
^{13}C spin rotation constants (kHz)	$C_{\parallel}=13; C_{\perp}=2.2$	40
The angle of C-C-H	111.5°	45, 46, 47
The distance between protons (10^{-10} m)	$r_{01}=r_{02}=1.77;$ $r_{03}=r_{04}=2.55; r_{05}=3.10$	45, 46, 47
Molecular diameter (10^{-10} m)	4.38	3

The numerical evaluation of theoretical equations using the values in Table 3 for ethane yields

$$\frac{1}{T_{1,\text{sr}}} (^1\text{H}) = 3.836 \times 10^8 T \tau_J \quad (\text{C2, km, cgs}) \quad (59)$$

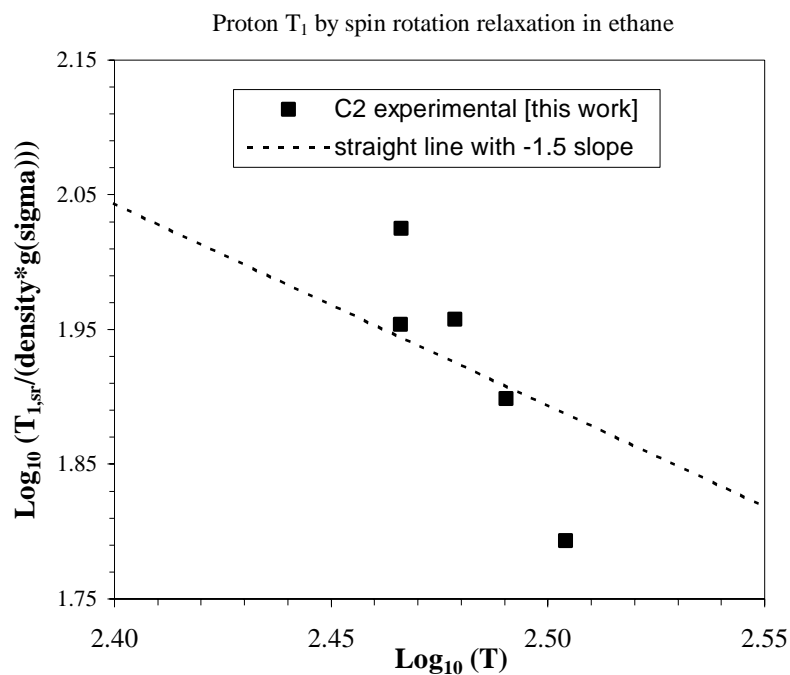
$$\frac{1}{T_{1,\text{sr}}} (^1\text{H}) = T \left[9.255 \times 10^7 \tau_{J\parallel} + 9.018 \times 10^7 (\tau_{J\perp} + 1/D_{\parallel}) + 1.707 \times 10^8 \tau_{J\perp} \right] \quad (\text{C2, dm, cgs}) \quad (60)$$

$$\frac{1}{T_{1,\text{sr}}} (^{13}\text{C}) = 2.694 \times 10^9 T \tau_J \quad (\text{C2, km, cgs}) \quad (61)$$

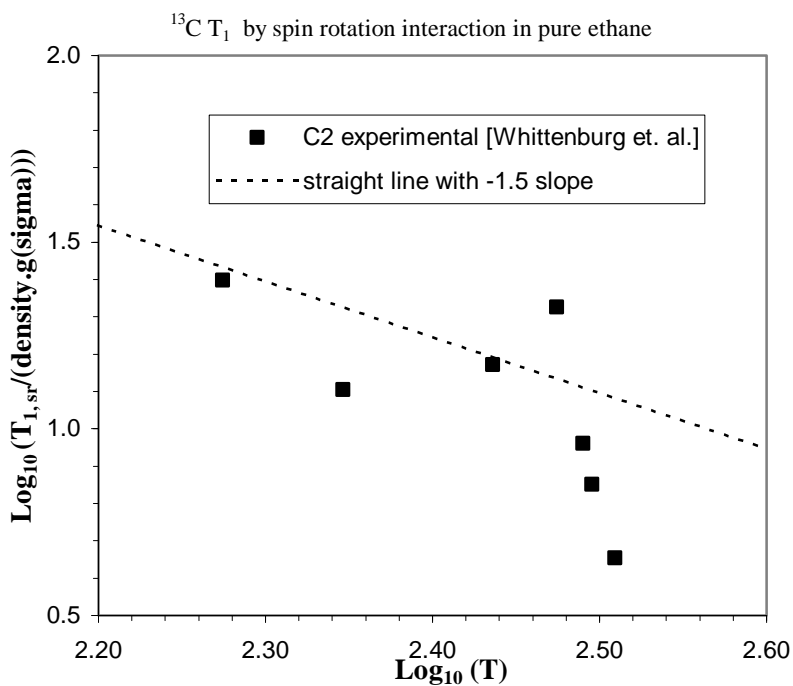
$$\frac{1}{T_{1,\text{sr}}} (^{13}\text{C}) = T \left(5.853 \times 10^8 \tau_{J\parallel} + 1.344 \times 10^8 \tau_{J\perp} \right) \quad (\text{C2, dm, cgs}) \quad (62)$$

The theoretical equations in the diffusion model can predict the linear dependence of $T_{1,\text{sr}}$ on viscosity/temperature. However, the analysis of NMR data indicates that $T_{1,\text{sr}}$ predicted by theoretical equations is almost always bigger than the experimental result. The lack of knowledge of some parameters in interpretation of τ_J by both models causes the difficulty in theoretical prediction of spin rotation interaction in ethane. Alternatively, we draw a straight line with the slope predicted by the models on the log-log plots to investigate the dependence of $T_{1,\text{sr}}$ on density and viscosity. Figure 3 shows $T_{1,\text{sr}}/(\rho g(\sigma))$ vs. T plots for ethane.⁴⁰ The plots of $T_{1,\text{sr}}$ vs. viscosity/temperature are shown in Figure 4.

⁴⁰ It is apparent that ^{13}C and ^1H $T_{1,\text{sr}}$ in ethane does not follow the power law relationship. The kinetic model does not work well for spin rotation interaction in ethane. Both ^1H and ^{13}C $T_{1,\text{sr}}$ data show that the diffusion model is a better model for ethane. Spin rotation interaction in ethane is better explained by the diffusion model while spin rotation interaction in methane is better described by the kinetic model.

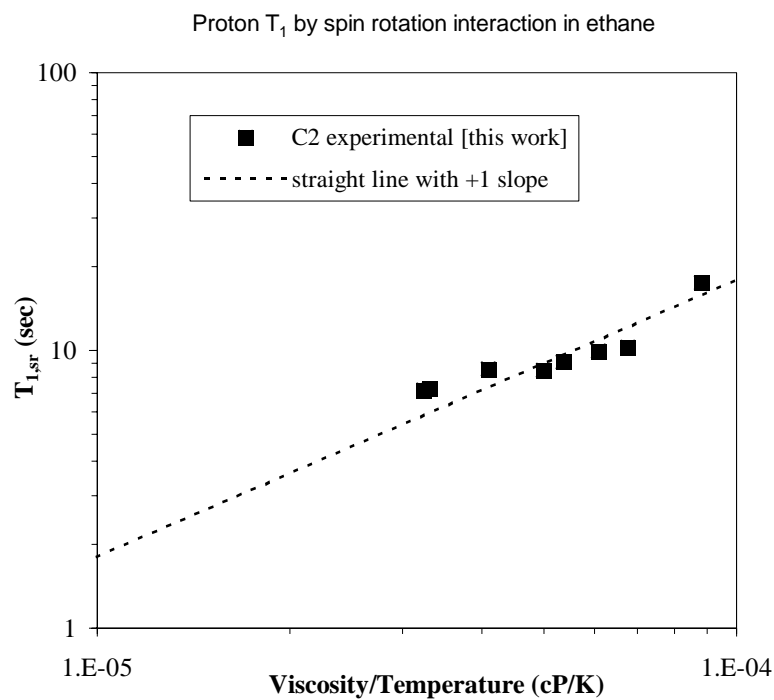


(a) ^1H data

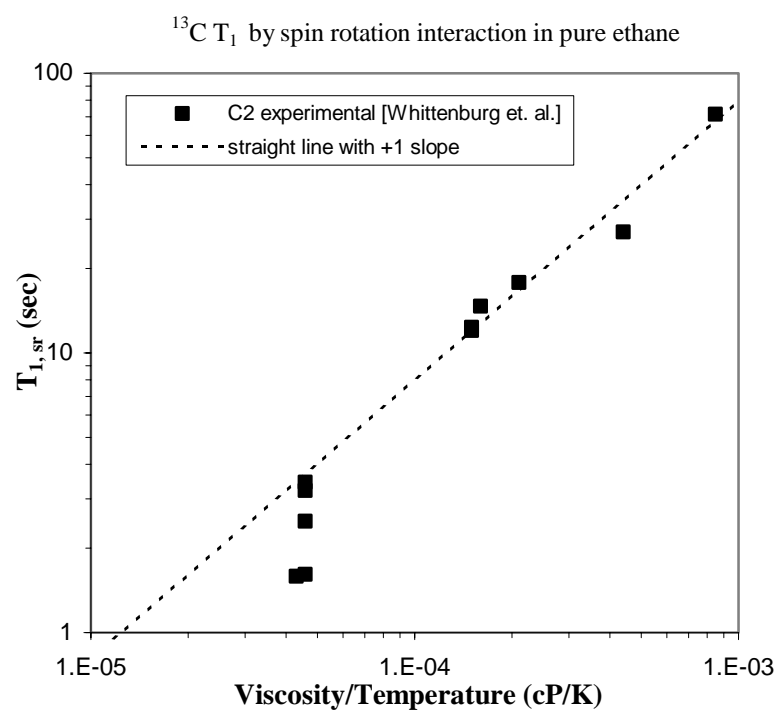


(b) ^{13}C data

Figure 3 $T_{1,\text{sr}}/(\rho g(\sigma))$ vs. T plots in ethane based on the kinetic model



(a) ^1H data



(b) ^{13}C data

Figure 4 $T_{1, sr}$ vs. η/T plots in ethane based on the diffusion model

3.1.3. Proton relaxation in pure ethane

For pure ethane, the total proton relaxation rate is accounted for by three interactions, i. e., the intra- and intermolecular dipole-dipole interactions and the spin rotation interaction. The total relaxation rate can be given by Equation (1).

3.1.3.1. Intermolecular dipole-dipole interaction

In order to use Equation (3) to predict relaxation rate for ethane, we need to make two additional modifications.

Firstly, the effect of the radial distribution function is taken into account. The following equation for intermolecular dipole-dipole interaction in ethane is obtained^{41, 43}

$$\frac{1}{T_{1,\text{inter}}} = R_{\text{inter}} = \frac{8\pi n v \gamma^4 \hbar^2 I(I+1)}{15D\sigma} \left[1 + \frac{\langle r^2 \rangle}{\sigma^2} \left(\frac{5}{12} + 0.0672\Omega' \right) + 0.0521\Omega' \right] \quad (63)$$

where $\langle r^2 \rangle$ is the root mean square distance of the random flight, and Ω' is as following

$$\Omega' = \frac{4}{3} \pi n \sigma^3 \quad (64)$$

For polyatomic molecules, such as ethane, a further effect must be considered. If the spins are not at the center of the molecule, the distance of closest approach of two spins will no longer be σ . In addition, the effect of rotation of the spin-bearing molecules on the purely translational relaxation should be considered. It turns out that these effects compete, the former tending to increase the relaxation rate, the latter decreasing it. Muller *et al.* extended Hubbard's treatment to ethane and derived the following equation for the relaxation time by intermolecular dipole-dipole interaction^{41, 43}

$$\begin{aligned} \frac{1}{T_{1,\text{inter}}} = R_{\text{inter}} = & \frac{8\pi n v \gamma^4 \hbar^2 I(I+1)}{15D\sigma} \left[1 + \frac{\langle r^2 \rangle}{\sigma^2} \left(\frac{5}{12} + 0.0672\Omega \right) + 0.0521\Omega \right] \\ & \cdot \left[1 + \alpha' \left(\frac{2d}{\sigma} \right)^2 + \beta' \left(\frac{2d}{\sigma} \right)^4 + \dots \right] \end{aligned} \quad (65)$$

where d is the distance of protons from the center of the molecule and α' and β' are factors taken from Ref. 42.

The result predicted by Equation (65) with two correction terms is in good agreement with Harmon's liquid ethane data.⁴¹

The numerical evaluation of Equation (65) gives

$$\frac{1}{T_{1,\text{inter}}} = 2.146 \times 10^{-6} \frac{\rho}{D} \left[1 + \left(\frac{5}{12} + 0.0672\Omega' \right) + 0.0521\Omega' \right] \quad (\text{cgs}) \quad (66)$$

3.1.3.2. Intramolecular dipole-dipole interaction

In contrast to the exponential autocorrelation function assumption, Moniz *et al.*⁴⁴ used Gaussian approximation to evaluate the autocorrelation function and then the contribution of intramolecular dipole-dipole interaction to the relaxation rate can be written as

$$\frac{1}{T_{1,\text{intra}}} = R_{\text{intra}} = \frac{3\gamma^4 \hbar^2}{4} \sum_{j=1}^5 r_{ij}^{-6} \left(\frac{\pi I_{\text{av}}}{3kT} \right)^{1/2} \quad (67)$$

Harmon⁴¹ has shown that Equation (67) can give good prediction for intramolecular dipole-dipole interaction in ethane at temperatures higher than 290K.

The numerical evaluation of Equation (67) gives

$$\frac{1}{T_{1,\text{intra}}} = \frac{0.125}{T^{1/2}} \quad (\text{cgs}) \quad (68)$$

3.1.3.3. Spin rotation interaction

The validity of the diffusion model for spin rotation interaction in ethane has been established. T_1 by spin rotation interaction can be found in the form of

$$T_{1,\text{sr}} = C_1 \left(\frac{\eta}{T} \right)^{C_2} \quad (69)$$

where C_1 and C_2 can be found by fitting pure ethane T_1 data if we assume that vapor ethane relaxes only by spin rotation interaction. Figure 5 is the plot. Therefore, $T_{1,\text{sr}}$ of ethane is estimated by

$$T_{1,\text{sr}} = 1.40 \times 10^4 \left(\frac{\eta}{T} \right)^{0.74} \quad (\text{cgs}) \quad (70)$$

The experimental data⁵⁵ of ethane proton relaxation times were compared with the relaxation times of ethane calculated from Equation (1), Equation (66), Equation (68) and Equation (70). The result was shown in Figure 6. The estimation compares closely with experimental results for proton relaxation in ethane.

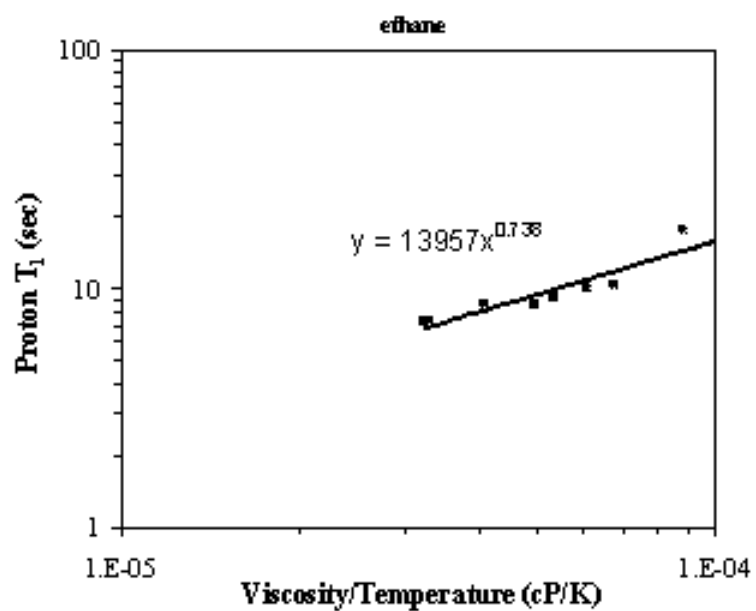


Figure 5 Correlation of spin rotation T_1 , viscosity and temperature for vapor ethane

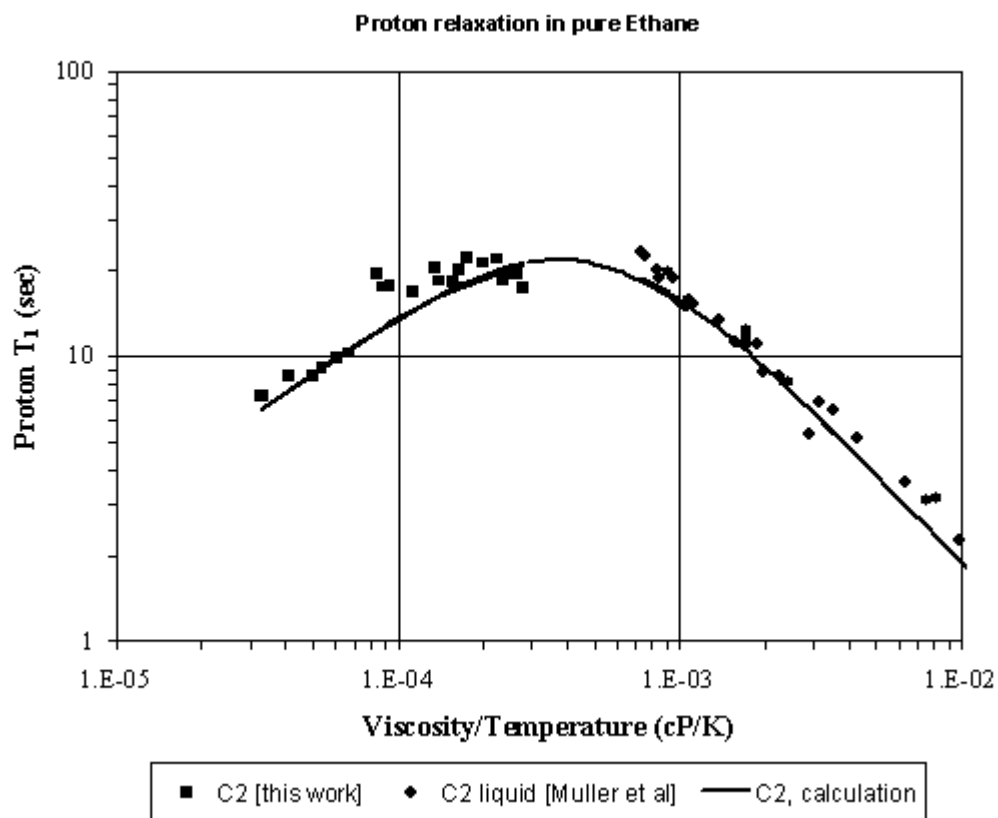


Figure 6 Comparison of experimental results and calculated results for pure ethane

The results of the analysis of our ethane T_1 data were presented in Figure 7. In the gaseous ethane, the contribution of intermolecular dipole-dipole interaction is less than 0.5% and can be negligible. The relaxation rate is mainly accounted for by intramolecular interactions. In particular, spin rotation interaction is the dominant mechanism in gaseous ethane. However, the all three contributions become significant for liquid ethane with increasing viscosity. For liquid ethane at cryogenic temperatures, intermolecular dipole-dipole interaction becomes the dominant relaxation mechanism.

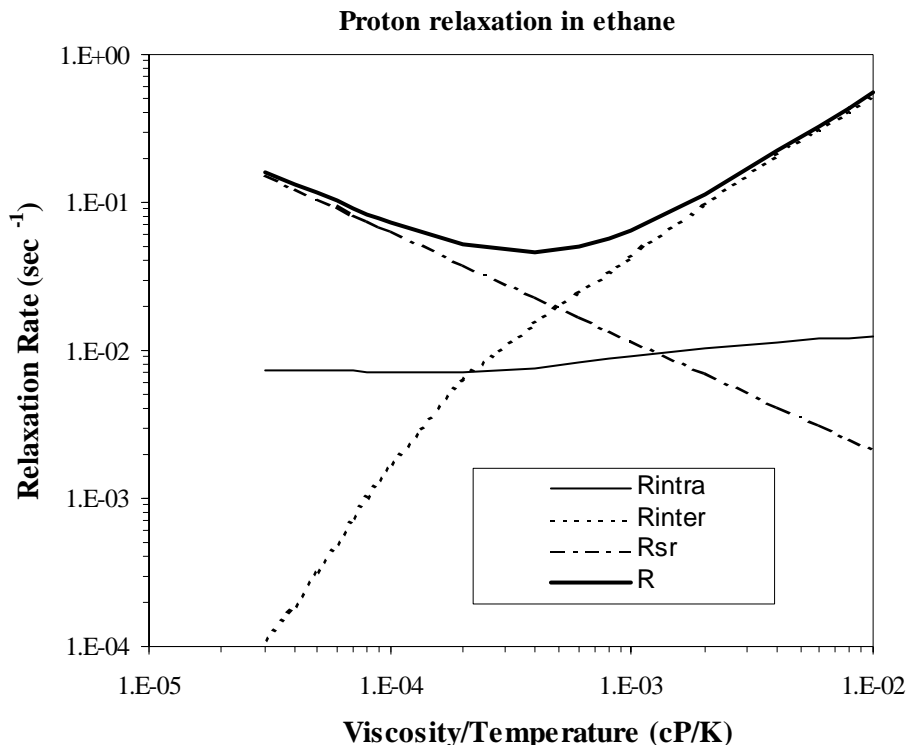


Figure 7 Contributions to the proton relaxation rate of ethane

3.2. Mixtures

3.2.1. Proton relaxation in CH₄ gas mixtures

The mixing rule is tested for five CH₄ gas mixtures, including CH₄-CO₂, CH₄-N₂, CH₄-He, CH₄-Ne and CH₄-Ar gas mixtures³⁰⁻³². In these gas mixtures, only methane contributes to proton relaxation times of the mixtures. The other components contain no protons and are “invisible” in proton NMR relaxation. Previous work indicates that methane molecular motion is still in the gas kinetic limit even at liquid densities.²⁶ It is reasonable to use the kinetic model to predict proton relaxation in methane. It is assumed that spin rotation interaction is the dominant mechanism for gaseous methane. The contribution by dipole-dipole interactions is neglected.

In order to calculate T_1 of CH_4 mixtures using Equation (49) and Equation (51), we need the knowledge of cross sections for angular momentum transfer for CH_4 molecules with various collision partners. In general, the collision cross section for angular momentum transfer can be reasonably represented by a function of the form³⁰⁻³³

$$\sigma_J = \sigma_J(300\text{K}) \left(\frac{T}{300} \right)^m \quad (71)$$

The cross sections for the collisions of CH_4 with CH_4 , CO_2 , N_2 , He, Ne and Ar were listed in Table 4. In particular, cross sections for angular momentum transfer for CH_4 -He and CH_4 -Ne pairs are estimated by fitting the data from NMR measurements³² in the form of Equation (71). Figure 8 and Figure 9 are the plots.

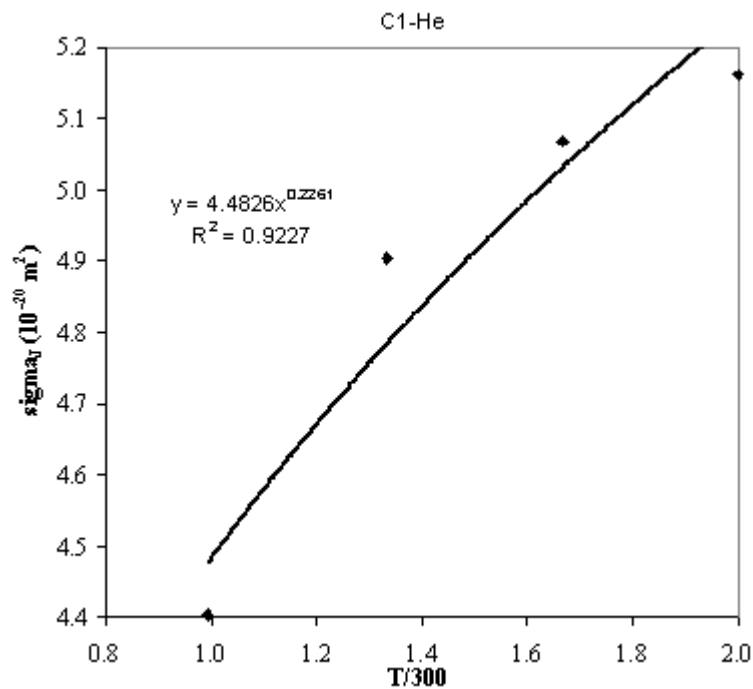


Figure 8 Correlation of cross section for angular momentum transfer by collisions for CH_4 -He

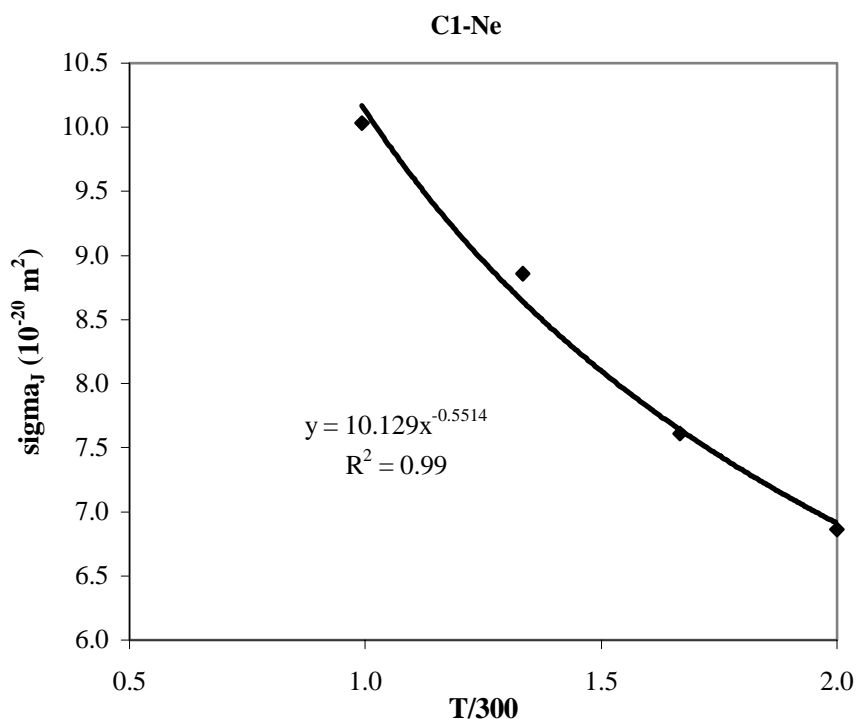


Figure 9 Correlation of cross section for angular momentum transfer by collisions for CH₄-Ne

Table 4 Cross section for angular momentum transfer for CH₄ molecules with various collision partners

pair	$\sigma_J(T), 10^{-20} \text{ m}^2$	reference
CH ₄ -CH ₄	$18.4(T/300)^{-0.90}$	33
CH ₄ -CO ₂	$24.1(T/300)^{-0.98}$	33
CH ₄ -N ₂	$16.3(T/300)^{-0.87}$	33
CH ₄ -He	$4.48(T/300)^{+0.27}$	this work
CH ₄ -Ne	$10.1(T/300)^{-0.55}$	this work
CH ₄ -Ar	$14.4(T/300)^{-0.79}$	33

Using the data from Table 4, we estimated relaxation times of five CH₄ gas mixtures by the mixing rule. Figure 10-14 compared the estimated results with experimental results^{30, 32} for CH₄-CO₂, CH₄-N₂ and CH₄-He, CH₄-Ne and CH₄-Ar gas mixtures respectively. The estimations from the mixing rule compare quite closely with experimental results.

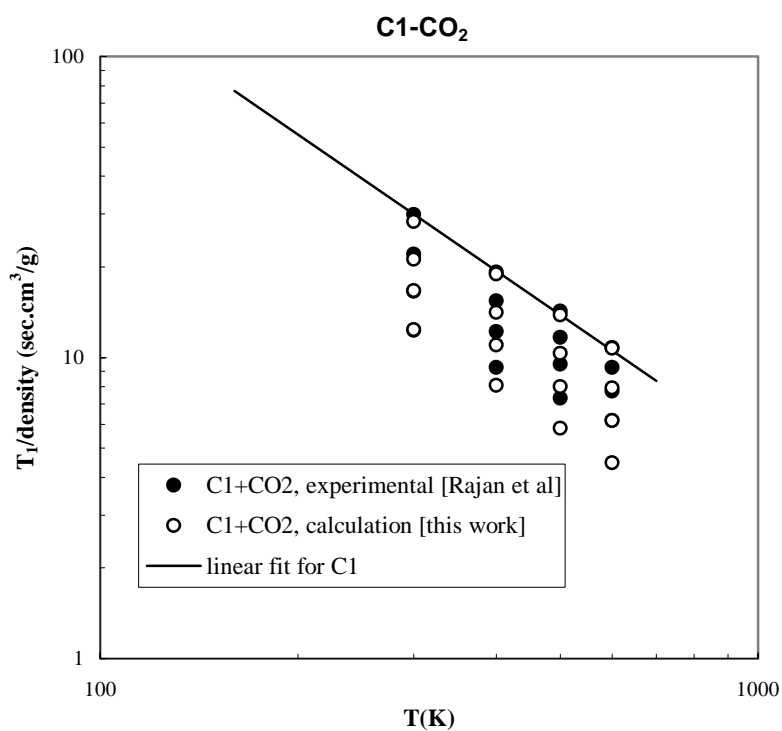


Figure 10 Comparison of experimental results and calculated results for CH₄-CO₂

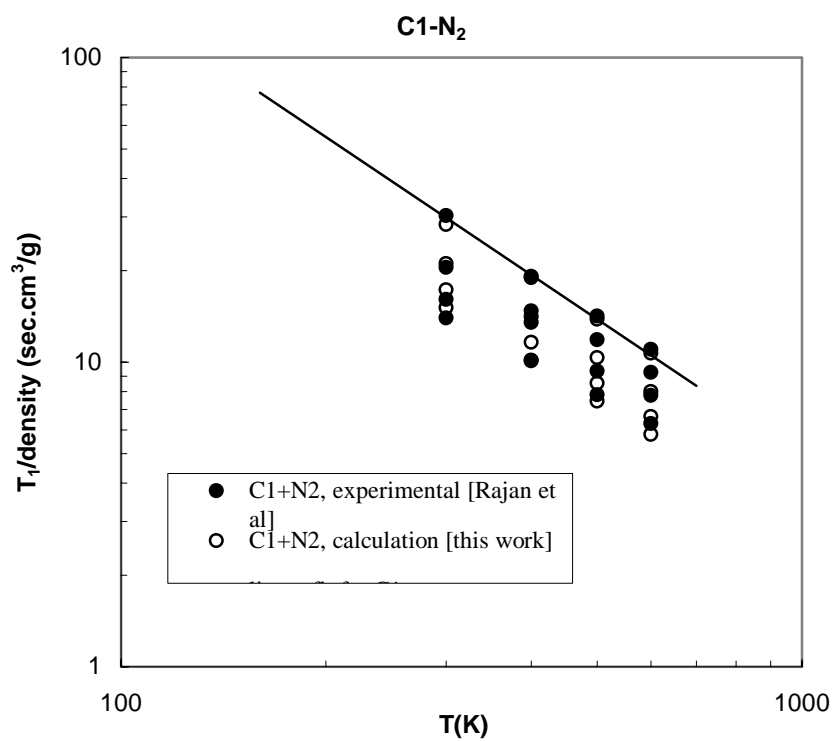


Figure 11 Comparison of experimental results and calculated results for CH₄-N₂

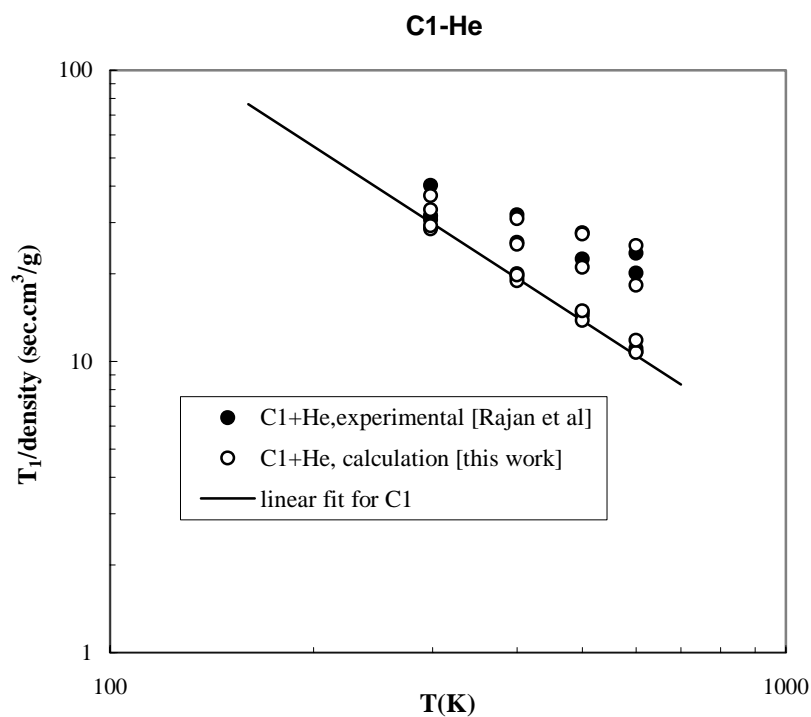


Figure 12 Comparison of experimental results and calculated results for $\text{CH}_4\text{-He}$

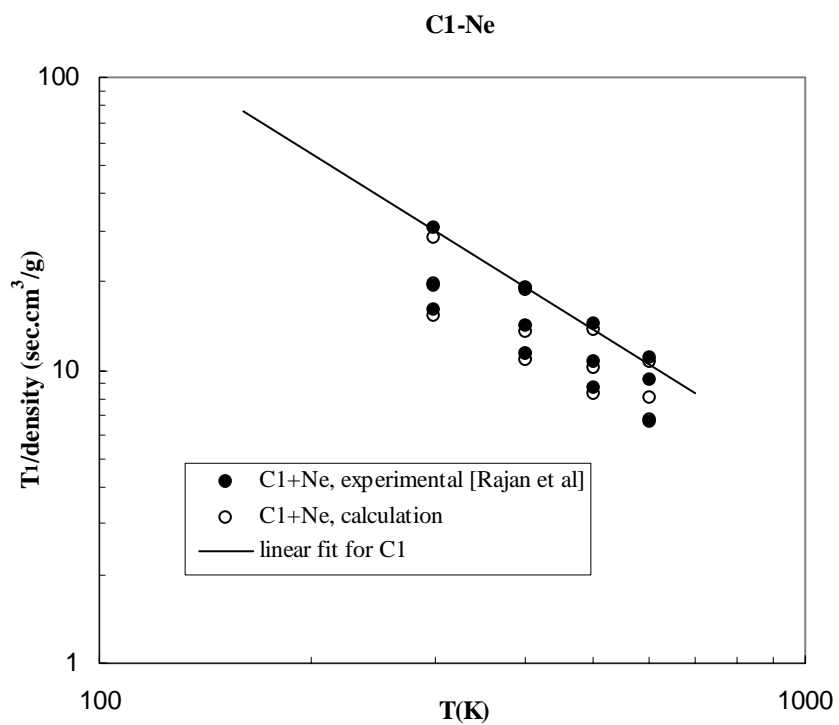


Figure 13 Comparison of experimental results and calculated results for $\text{CH}_4\text{-Ne}$

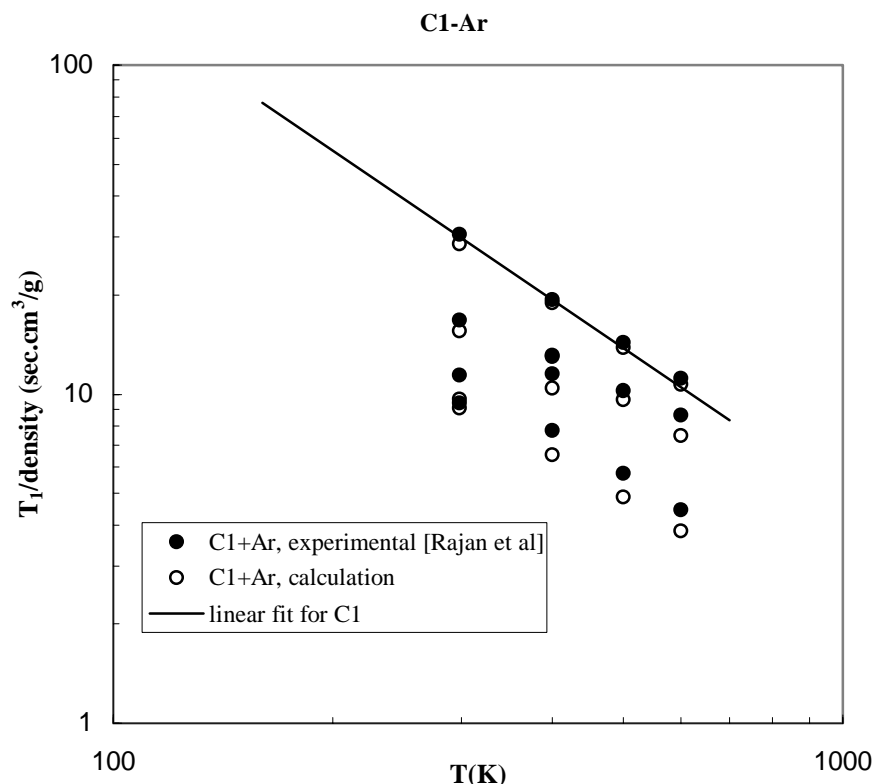


Figure 14 Comparison of experimental results and calculated results for $\text{CH}_4\text{-Ar}$

3.2.2. Proton relaxation in $\text{CH}_4\text{-C}_2\text{H}_6$ gas mixtures

In CH_4 (A)- C_2H_6 (B) gas mixtures, there are two contributions to proton T_1 , one from protons of methane and the other from protons of ethane. The log mean T_1 may be described by Equation (46). It is assumed that the spin rotation interaction is the dominant interaction for both methane and ethane in the dilute gas mixtures. It has been established that the relaxation of methane can be described by the kinetic model while the relaxation of ethane can be described by the diffusion model. The relaxation by the spin rotation mechanism for methane may be given by Equation (49) and Equation (51). The relaxation by the spin rotation mechanism for ethane may be calculated by Equation (70).

The cross section for angular momentum transfer for the collisions between methane molecules and ethane molecules is not available. Currently, it is difficult to apply the mixing rule to $\text{CH}_4\text{-C}_2\text{H}_6$ mixtures. However, the collision cross section for angular momentum transfer can be estimated from NMR T_1 data of the mixtures. It is expected that NMR relaxation times will be measured for $\text{CH}_4\text{-C}_2\text{H}_6$ gas mixtures by this lab. Then the mixing rule can be tested for $\text{CH}_4\text{-C}_2\text{H}_6$ gas mixtures.

IV. Conclusions

The theory about relaxation mechanisms in gases and liquids was summarized. It was found that $T_{1,\text{sr}}/n$ has a $T^{3/2}$ temperature dependence in the kinetic model while $T_{1,\text{sr}}$ is proportional to η/T in the diffusion model. The proton spin rotation interaction constants were calculated for ethane, and the results were $C_{\perp} = 1.46\text{kHz}$ and $C_{\parallel} = 6.95\text{kHz}$. Spin rotation interaction in methane is better described by the kinetic model while spin rotation interaction in ethane is better explained by the diffusion model. The estimation based on Equation (1), Equation (66), Equation (68) and Equation (70) compares closely with experimental results for proton relaxation in ethane. Spin rotation interaction is shown to be the main contribution in gaseous ethane. At liquid densities, intra- and intermolecular dipole-dipole interactions and spin rotation interaction all have significant contributions. The general mixing rule for T_1 was proposed. The estimations by the mixing rule agree well with experimental results for $\text{CH}_4\text{-CO}_2$, $\text{CH}_4\text{-N}_2$, $\text{CH}_4\text{-He}$, $\text{CH}_4\text{-Ne}$ and $\text{CH}_4\text{-Ar}$ gas mixtures.

V. References

1. McConnell, J., *The Theory of Nuclear Magnetic Relaxation in Liquids*, Cambridge University Press, New York, 1987.
2. Abragam, A., *The Principles of Nuclear Magnetism*, Oxford University Press, London, 1961.
3. Hirschfelder, J. O., Curtiss, C. F., and Bird, R. B., *Molecular Theory of Gases and Liquids*, John Wiley & Sons, New York, 1954.
4. Bartoli, F. J. and Litovitz, T. A., "Raman Scattering: Orientational Motions in Liquids", *J. Chem. Phys.*, Vol. 56, p. 413-425 (1972).
5. Alms, G. R., Bauer, D. R., Brauman, J. I., and Pecora, R., "Depolarized Rayleigh Scattering and Orientational Relaxation of Molecules in Solution. I. Benzene, Toluene, and para-Xylene", *J. Chem. Phys.*, Vol. 58, p. 5570-5578 (1973).
6. Alms, G. R., Bauer, D. R., Brauman, J. I., and Pecora, R., "Depolarized Rayleigh Scattering and Orientational Relaxation of Molecules in Solution. II. Chloroform and Nitrobenzene", *J. Chem. Phys.*, Vol. 59, p. 5310-5320 (1973).
7. Alms, G. R., Bauer, D. R., Brauman, J. I., and Pecora, R., "Depolarized Rayleigh Scattering and Orientational Relaxation of Molecules in Solution. III. Carboxylic Acids", *J. Chem. Phys.*, Vol. 59, p. 5321-5328 (1973).
8. Bauer, D. R., Brauman, J. I., and Pecora, R., "Depolarized Rayleigh Scattering and Orientational Relaxation of Molecules in Solution. IV. Mixtures of Hexafluorobenzene with Benzene and with Mesitylene", *J. Chem. Phys.*, Vol. 63, p. 53-59 (1975).
9. Evans, G. T. and Kivelson, D., "The Orientational-Correlation Time Intercept in Liquids", *J. Chem. Phys.*, Vol. 84, p. 385-390 (1986).

10. Gordon, R. G., "Kinetic Theory of Nuclear Spin Relaxation in Gases", *J. Chem. Phys.*, Vol. 44, p. 228-234 (1966).
11. Gordon, R. G., "Nuclear Spin Relaxation and Collision Frequency in Dense Gases", *J. Chem. Phys.*, Vol. 48, p. 2655-2657 (1968).
12. Bloom, M., Bridges, F., and Hardy, W. N., "Nuclear Spin Relaxation in Gaseous Methane and Its Deuterated Modifications", *Can. J. Phys.*, Vol. 45, p. 3533-3554 (1967).
13. Dong, R. Y. and Bloom, M., "Determination of Spin Rotation Interaction Constants in Fluorinated Methane Molecules by Means Of Nuclear Spin Relaxation Measurements", *Can. J. Phys.*, Vol. 48, p. 793-804 (1970).
14. Armstrong, R. L. and Courtney, J. A., "A Nuclear Spin Relaxation Study of the Spin-Rotation Interaction in Spherical Top Molecules", *Can. J. Phys.*, Vol. 50, p. 1252-1261 (1972).
15. Armstrong, R. L. and Courtney, J. A., "A Nuclear Spin Relaxation Study of the Spin-Rotation Interaction in Symmetric Top Molecules", *Can. J. Phys.*, Vol. 50, p. 1262-1272 (1972).
16. Dymond, J. H., "Hard-sphere Theories of Transport Properties", *Chem. Soc. Rev.*, Vol. 14, p.317-356 (1985).
17. Carnahan, N. F. and Starling, K. E., "Equation of State for Nonattracting Rigid Spheres", *J. Chem. Phys.*, Vol. 51, p. 635-636 (1969).
18. McClung, R. E. D. and Kivelson, D., "ESR Linewidths in Solution. V. Studies of Spin-Rotational Effects Not Described by Rotational Diffusion Theory", *J. Chem. Phys.*, Vol. 49, p. 3380-3391 (1968).
19. Hu, C. and Zwanzig, R., "Rotational Friction Coefficients for Spheroids with The Slipping Boundary Condition", *J. Chem. Phys.*, Vol. 60, p. 4354-4357 (1974).
20. Wang, C. H., "Anisotropic-Rotational Diffusion Model Calculation of T_1 Due to Spin-Rotation Interaction in Liquids", *J. Magn. Reson.*, Vol. 9, p.75-83 (1973).
21. McClung, R. E. D., "Rotational Diffusion of Symmetric Top Molecules in Liquids", *J. Chem. Phys.*, Vol. 57, p.5478-5491 (1972).
22. Wang, C. H., Grant, D. M., and Lyster, J. R., "Spin-Rotational Relaxation Time in Liquids of Symmetric-Top Molecules", *J. Chem. Phys.*, Vol. 55, p. 4674-4675 (1971).
23. Hubbard, P. S., "Theory of Nuclear Magnetic Relaxation by Spin-Rotational Interactions in Liquids", *Phys. Rev.*, Vol. 131, p. 1155-1165 (1963).
24. Blicharski, J. S., "Spin Rotational Magnetic Relaxation for Nonlinear Molecules", *Acta Physica Polonica*, Vol. XXIV, p. 817-821 (1963).
25. Oosting, P. H. and Trappeniers, N. J., "Proton-Spin-Lattice Relaxation and Self-Diffusion in Methanes II. Experimental Results for Proton Spin Lattice Relaxation-Spin-Lattice Relaxation Times", *Physica*, Vol.51, p.381-394 (1971).
26. Gerritsma, C. J., Oosting, P. H. and Trappeniers, N. J., "Proton-Spin-Lattice Relaxation and Self-Diffusion in Methanes III. Interpretation of Proton Spin Lattice Relaxation Experiments", *Physica*, Vol.51, p. 395-417 (1971).

27. Lo, S. W., "Correlations of NMR Relaxation Time with Viscosity/Temperature, Diffusion Coefficient and Gas/Oil Ratio of Methane-Hydrocarbon Mixtures," Ph.D. dissertation, Rice University, Houston, Texas (1999).
28. Bovey, L. F. H., "Rotation-Vibration Spectra of Diatomic and Simple Polyatomic Molecules with Long Absorbing Paths. X. The Spectrum of Tri-Deuteromethane in The Photographic Infrared", *J. Chem. Phys.*, Vol. 21, p. 830-836 (1953).
29. Yi, P. N., Ozier, I., and Ramsey, N. F., "Low-Field Hyperfine Spectrum of CH₄", *J. Chem. Phys.*, Vol. 55, p. 5215-5227 (1971).
30. Rajan, S. and Lalita, K., "Intermolecular Potentials from NMR Data: I. CH₄-N₂ and CH₄-CO₂", *Can. J. Phys.*, Vol. 53, p. 1624-1630 (1975).
31. Rajan, S. and Lalita, K., "Intermolecular Potentials from NMR Data: II. CH₄, CF₄, and SiF₄", *Can. J. Phys.*, Vol. 53, p. 1631-1634 (1975).
32. Rajan, S. and Lalita, K., "Nuclear Spin-Lattice Relaxation in CH₄-Inert Gas Mixtures", *J. Magn. Reson.*, Vol. 16, p. 115-129 (1974).
33. Jameson, C. J., Jameson, A. K., Smith, N. C., Hwang, J. K., and Zia, T., "¹³C and ¹H Spin Relaxation in CH₄ in the Gas Phase", *J. Phys. Chem.*, Vol. 95, p. 1092-1098 (1991).
34. Johnson, C. J. and Waugh, J. S., "Nuclear Relaxation in Gases: Mixtures of Methane and Oxygen", *J. Chem. Phys.*, Vol. 35, p. 2020-2024 (1961).
35. Tward, E. and Armstrong, R. L., "Spin-Lattice Relaxation in Dilute Gases. I. Proton Relaxation in HCl, HBr, and HI", *J. Chem. Phys.*, Vol. 47, p. 4068-4071 (1967).
36. Armstrong, R. L. and Tward, E., "Spin-Lattice Relaxation in Dilute Gases. II. ¹⁹F Relaxation in CF₄ and SiF₄", *J. Chem. Phys.*, Vol. 48, p. 332-334 (1967).
37. Armstrong, R. L. and Hanrahan, T. A. J., "Spin-Lattice Relaxation in Dilute Gases. III. ¹H Relaxation in NH₃ and ¹⁹F Relaxation in BF₃", *J. Chem. Phys.*, Vol. 49, p. 4777-4780 (1968).
38. Armstrong, R. L. and Courtney J. A., "Spin-Lattice Relaxation in Dilute Gases. IV. Proton Relaxation in PH₃", *J. Chem. Phys.*, Vol. 51, p. 457-461 (1969).
39. Courtney J. A. and Armstrong, R. L., "Spin-Lattice Relaxation in Dilute Gases. V. ¹⁹F Relaxation in Fluorine Gas", *J. Chem. Phys.*, Vol. 52, p. 2158-2159 (1970).
40. Whittenburg, S. L., Evilia, R. F., and Robert, J. R., "Studies of Rotational Relaxation Times at Low Viscosity: Ethane", *J. Mol. Liquids*, Vol. 51, p. 115-122 (1992).
41. Harmon, J. F., "Molecular Motion in Liquid Ethane, An NMR Study", Ph.D. dissertation, University of Wyoming, 1968.
42. Muller, B. H., "Comment on The Articles: 'Nuclear Magnetic Relaxation by Intermolecular Dipole-Dipole Interactions', and 'Nuclear Spin Relaxation in Liquid and Solid Methane: Isotope Effects' ", *Can. J. Phys.*, Vol. 44, p. 2511-2513 (1966).
43. Harmon, J. F. and Muller, B. H., "Nuclear Spin Relaxation by Translational Diffusion in Liquid Ethane", *Phys. Rev.*, Vol. 182, p. 400-410 (1969).

44. Moniz, W. B., Steele, W. A., and Dixon, J. A., "Nuclear Spin Relaxation in Liquids. Spheroidal Molecules", *J. Chem. Phys.*, Vol. 38, p. 2418-2426 (1963).
45. Kuchitsu, K., "Comparison of Molecular Structures Determined by Electron Diffraction and Spectroscopy. Ethane and Diborane", *J. Chem. Phys.*, Vol. 49, p. 4456-4462 (1968).
46. Lafferty, W. J. and Plyler, E., "Molecular Parameters of Ethane", *J. Chem. Phys.*, Vol. 37, p. 2688-2692 (1962).
47. Hirota, E., Endo, Y., and Saito, S., "Microwave Spectra of Deuterated Ethanes: Internal Rotation Potential Function and r_z Structure", *J. Mol. Spectrosc.*, Vol. 89, p. 285-295 (1981).
48. Kaski, J., Lantto, P., Vaara, J., and Jokisaari, J., "Experimental and Theoretical *ab Initio* Study of The ^{13}C - ^{13}C spin-spin Coupling and ^1H and ^{13}C Shielding Tensors in Ethane, Ethene, and Ethyne", *J. Am. Chem. Soc.*, Vol. 120, p. 3993-4005 (1998).
49. Flygare, W. H., "Spin-Rotation Interaction and Magnetic Shielding in Molecules", *J. Chem. Phys.*, Vol. 41, p. 793-800 (1964).
50. Flygare, W. H. and Goodisman, J., "Calculation of Diamagnetic Shielding in Molecules", *J. Chem. Phys.*, Vol. 49, p. 3122-3124 (1968).
51. Deverell, C., "Nuclear Magnetic Relaxation by Spin-Rotation Interaction. Determination of Spin-Rotation Interaction Constants from Nuclear Magnetic Shielding Constants", *Mol. Phys.*, Vol. 18, p. 319-325 (1970).
52. Rigny, P. and Virlet, J., "Molecular Motion and ^{19}F Relaxation in The Liquid Hexafluorides of Molybdenum, Tungsten, and Uranium", *J. Chem. Phys.*, Vol. 47, p. 4645-4652 (1967).
53. Debye, P. *Polar Molecules*, The Chemical Catalog Company, Inc., New York, 1929.
54. McConnell, J., *Rotational Brownian Motion and Dielectric Theory*, Academic Press, New York, 1980.
55. Muller, B. H. and Noble, J. D., "Proton Spin-Lattice Relaxation in Pure Liquid Ethane and Some of Its Deuterated Modifications" *J. Chem. Phys.*, p.777-779 (1962).

Relaxation Time and Diffusivity of Hydrocarbon Mixtures

G. J. Hirasaki and S.-W. Lo

Abstract

The relation between the relaxation time and diffusivity distributions of hydrocarbon mixtures is examined. The system investigated is mixtures of *n*-hexane and squalene, a 30-carbon hydrocarbon. The results verify the assumption made in the “constituent viscosity model.”

Introduction

Interpretation of NMR well logs are often complicated by relaxation time distributions of hydrocarbons which overlap the relaxation time distribution of the water. The water has a distribution of relaxation times because of the surface relaxation by the pore walls. Several methods have been introduced to distinguish between the oil and water [Akkurt (1999), Looyestijn (1996), and Slijkerman, et al. (1999)]. These methods rely on the magnetic field gradient of the logging tool and the difference in diffusivity (diffusion coefficient) between the oil and water. Freedman, et al. (2000) introduced the constituent viscosity model (CVM) to distinguish the oil and water. “In the CVM, each hydrocarbon molecule in the mixture is assumed to relax and diffuse like it would in the pure-state liquid except the macroscopic pure-state viscosity is replaced by the microscopic constituent viscosity.” This implies that the relaxation time distribution and diffusivity distribution are coupled through a common “constituent viscosity.” The expressions for the mixture and the constituent relaxation time, diffusivity, and viscosity are as follows.

$$\begin{aligned} T_{2,LM} &= \frac{aT}{\eta}, & T_{2,k} &= \frac{aT}{\eta_k}, & T_{2,LM} &= \prod_{k=1}^N T_{2,k}^{f_k} \\ D_{LM} &= \frac{bT}{\eta}, & D_k &= \frac{bT}{\eta_k}, & D_{LM} &= \prod_{k=1}^N D_k^{f_k} \\ \frac{D_{LM}}{T_{2,LM}} &= \frac{D_k}{T_{2,k}} = \frac{b}{a} \\ \eta &= \prod_{k=1}^N \eta_k^{f_k} = \frac{aT}{T_{2,LM}} = \frac{bT}{D_{LM}} \\ \sum_{k=1}^N f_k &= 1 \end{aligned}$$

The parameter, f_k , is the proton fraction the k -th molecular constituent. The parameters, a and b , were determined from measurements of the relaxation time and diffusivity of pure components and mean value of mixtures. The ratio of b/a is equal to 5.28×10^{-6} (cm²/s²) for alkanes and 1.26×10^{-5} (cm²/s²) for crude oils. This model assumes that relaxation time and diffusivity distributions are coupled with each constituent having a common proportionality constant, b/a .

The relation between the relaxation rate and viscosity of *n*-hexane and *n*-hexadecane mixtures was the subject of investigation by Zega, et al. (1990). They found the mole fraction weight-average relaxation rate to be proportional to the viscosity as in pure fluids. The proton fraction average relaxation rate was not exactly proportional. Lo, et al. (2000) found that the individual-component relaxation times of *n*-hexane and *n*-hexadecane were quite different but the proton fraction weighted geometric mean relaxation time was a good approximation to the relaxation time – viscosity relation for pure alkanes. The diffusivity distribution of *n*-hexane and *n*-hexadecane mixtures overlapped too much to determine if the diffusivity distribution corresponded to the relaxation time distribution. Freedman, et al. (2000) used mixtures of *n*-hexane (C₆H₁₄) and squalene (C₃₀H₅₀) to demonstrate the relation between the relaxation time and diffusivity distributions for this mixture. Publication space limitations did not permit detail discussion of those results so they are presented here.

Materials and Experimental Methods

The *n*-hexane and squalene were deoxygenated by freezing, applying vacuum and thawing under nitrogen. The NMR measurements were made on a 2 MHz MARAN-2 spectrometer. T_2 was measured by the Carr-Purcell-Meiboom-Gill (CPMG) method and the diffusivity was measured by the pulsed field gradient (PFG) method. Mixtures of *n*-hexane and squalene were prepared with hexane proton fraction, H(C6), equal to 0.38, 0.50, and 0.69.

Results and Discussion

The relaxation time and diffusivity distributions are shown in Figs. 1 and 2, respectively, and summarized in Table 1. The values in the tables are the bi-exponential fit results. The light vertical line on each plot is the relaxation time estimated by fitting the CPMG response to a bi-exponential model. H(C6) is the proton fraction of hexane in the mixture. A(C6) is the fraction of the area attributed to hexane. There is good agreement between H(C6) and A(C6). The peaks of the diffusivity distributions are broader than those for the T_2 distributions. This can be explained by the difference in signal/noise for the two measurements. The T_2 is determined from 8,000 echoes of the CPMG method while the diffusivity is determined from 58 different gradient pulse time intervals. Fig. 3 are plots of the constituent relaxation time and diffusivity, respectively. There is about an order of magnitude change in the relaxation time and diffusivity of squalene. The change for *n*-hexane is less. Fig. 4 is a plot of the ratio of diffusivity/relaxation time for squalene and *n*-hexane. The dashed line is the ratio, b/a , determined for pure and mixtures of alkanes. The average absolute deviation of the ratio, D/T_2 from the independently determined value of b/a is 27%. It is clear that the deviation could be reduced if b/a was determined specifically for the *n*-hexane and squalene mixture. Fig. 5 is the correlation between the pure and constituent diffusivity and relaxation time for the *n*-hexane and squalene systems. The measured points compare well with the correlation that was independently developed from pure alkanes and mixture of alkanes.

Conclusions

The measurements of relaxation time and diffusivity for the pure materials and mixtures of *n*-hexane and squalene verify the coupling between the relaxation time and

diffusivity of constituents in a mixture. The area fractions in the distributions correspond to the proton fraction of the corresponding constituent.

References

- Akkurt, R., Marschall, D., Eyvazzadeh, R. Y, Gardner, J. S., Mardon, D, and Dunn, K. J., (1999) "Determination of Residual Oil Saturation by Use of Enhanced Diffusion," *SPE Reservoir Eval. & Eng.* 2 (3) 303-309.
- Freedman, R., Sezginer, A., Flaum, M., Matteson, A., Lo, S-W., and Hirasaki, G. J. (2000) "A New NMR Method of Fluid Characterization in Reservoir Rocks: Experimental Confirmation and Simulation Results," 2000 SPE ATCE, Dallas, TX, Oct. 1-4.
- Lo, S.-W., Hirasaki, G. J., House, W. V. and Kobayashi, R. (2000) "Correlations of NMR Relaxation Time with Viscosity, Diffusivity, and Gas/Oil Ratio of Methane/Hydrocarbon Mixtures," 2000 SPE ATCE, Dallas, TX, Oct. 1–4.
- Looyestijn, W. J. (1996) "Determination of Oil Saturation from Diffusion NMR Logging," paper SS, SWPLA 37th Ann. Logging Symp., New Orleans, LA, June 16-19.
- Slijckerman, W.F.J., Looyestijn, W.J., and Hofman, J.P. (1999) "Processing of Multi-Acquisition NMR Data," SPE 56768, SPE ATCE, Houston, TX, Oct. 3-6.
- Zega, J. A., House, W. V., and Kobayashi, R. (1990), "Spin-Lattice Relaxation and Viscosity in Mixtures of *n*-Hexane and *n*-Hexadecane," *I&EC Research*, 29, 909-912.

Nomenclature

- a parameter in relaxation time - viscosity correlation, s·cp/K
- $A(C6)$ area fraction attributed to hexane
- b parameter in diffusivity – viscosity correlation, cm²·cp/(K·s)
- D diffusivity, cm²/s
- f proton fraction of component k
- $H(C6)$ proton fraction of hexane
- T temperature, K
- η viscosity, cp

Table 1 Relaxation time and diffusivity of <i>n</i> -hexane and squalene mixtures				
H(C6)	$T_2(C6)$, s	$T_2(C30)$, s	$D(C6)$, cm ² /s	$D(C30)$, cm ² /s
0.00		0.294		1.01E-06
0.38	4.59	0.90	1.27E-05	3.47E-06
0.50	5.75	1.18	1.70E-05	4.94E-06
0.69	7.52	1.69	3.02E-05	9.89E-06
1.00	9.78		4.60E-05	

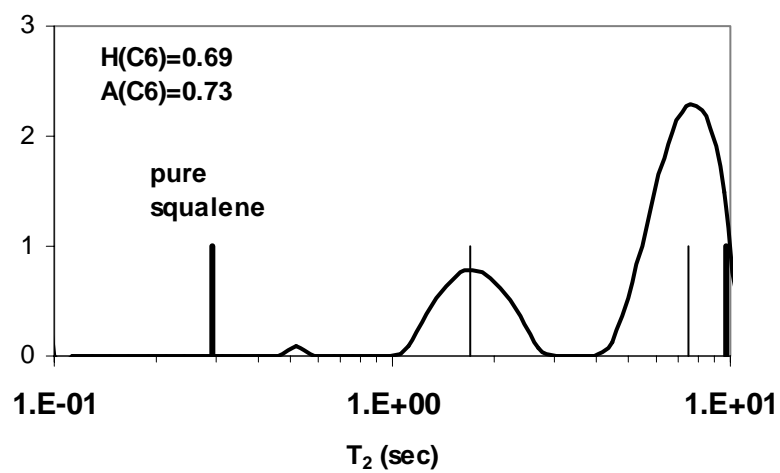
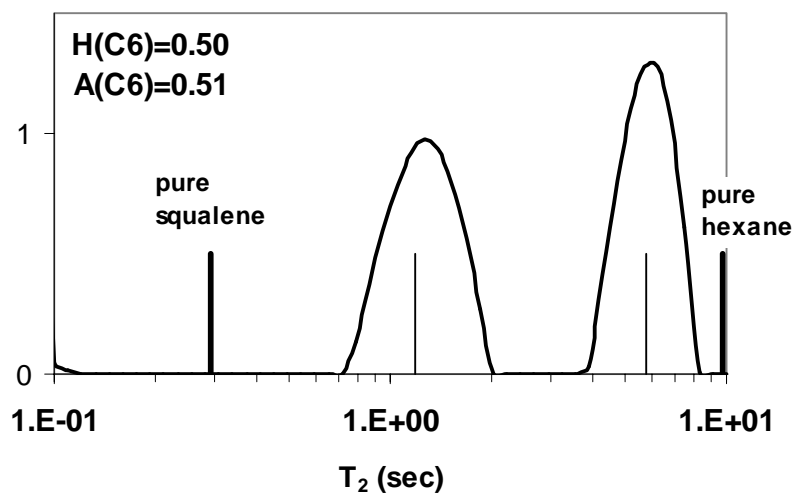
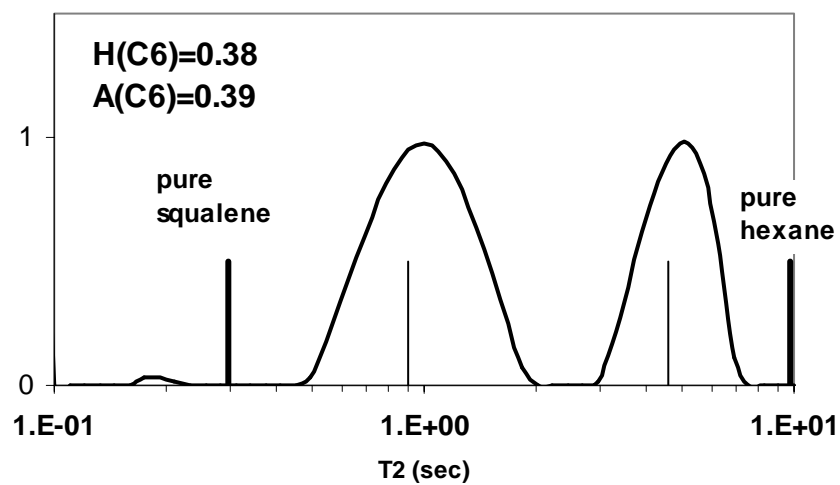


Fig. 1. Relaxation time distributions of *n*-hexane and squalene mixtures. Thin line is estimate from bi-exponential fit.

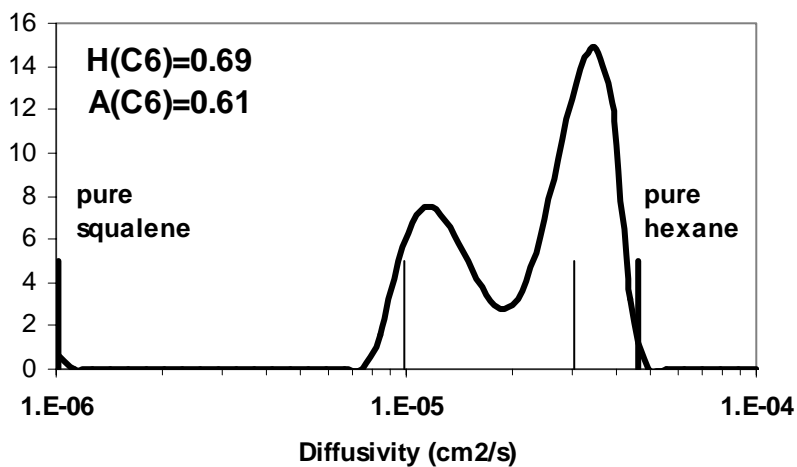
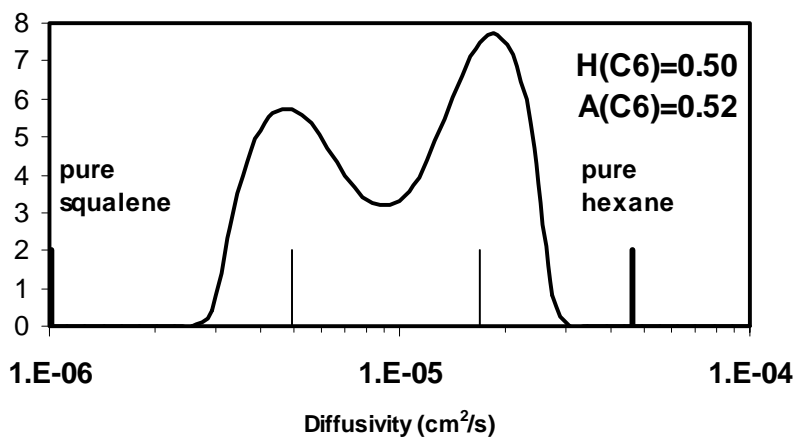
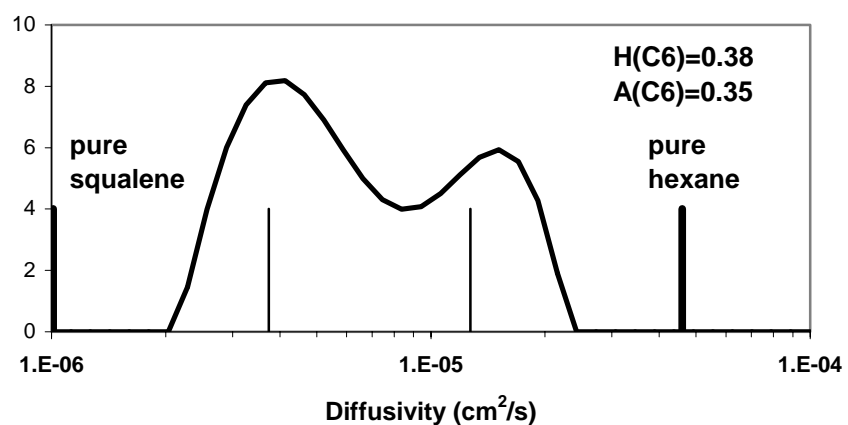


Fig. 2 Diffusivity of *n*-hexane and squalene mixtures.

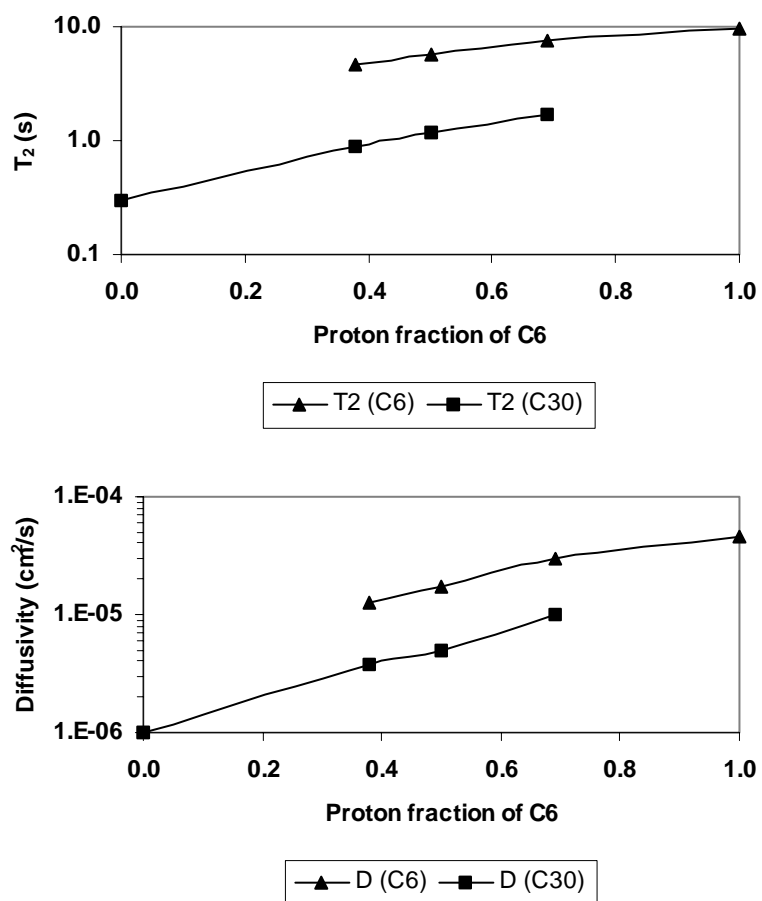


Fig. 3. Constituent relaxation time and diffusivity as a function of concentration.

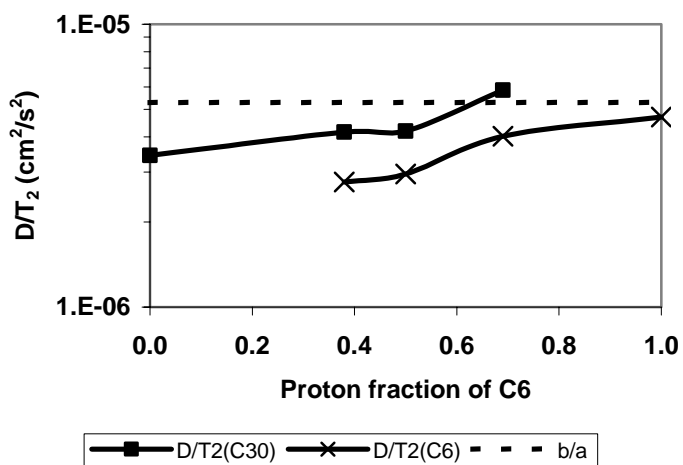


Fig. 4. Ratio of constituent diffusivity and relaxation time compared to the correlation.

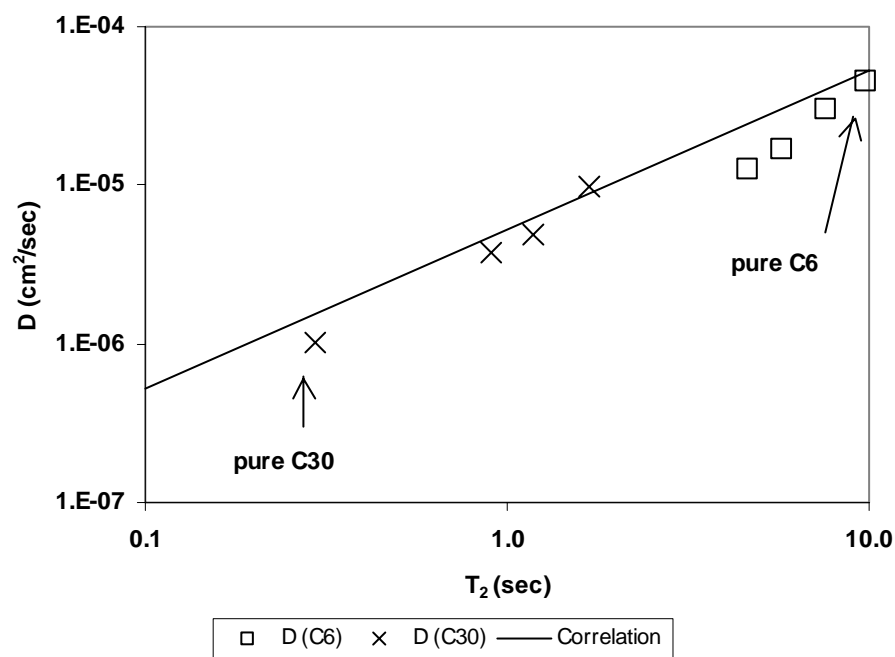


Fig. 5 Correlation between constituent diffusivity and relaxation time of *n*-hexane and squalene. The line is the correlation developed independently from pure and mixture of alkanes.

Relaxation Time Distribution of Asphaltenic Oils

G.J. Hirasaki, K. McCann, A. Vinegar, and Y. Zhang

ABSTRACT

Heavy and moderate gravity oils have a relaxation time distribution that overlaps with that of the capillary bound water. The ratio of the log mean T_1/T_2 is a function of the oil viscosity and asphaltene content and the Larmor frequency of the NMR spectrometer.

INTRODUCTION

Morris, et al. (1997) showed that the T_2 relaxation time distribution of crude oils can have a significant overlap with that of the capillary bound water (e.g. below 33 ms) for crude oils with a viscosity even under 10 cp. In addition, they showed that oils with viscosity greater than 800 cp had the entire relaxation time distribution in the region of capillary bound water.

Vinegar, et al. (1991) measured the T_1 of a number of crude oils with a 80 MHz NMR spectrometer and found that the log mean T_1 had a minimum value of about 100 ms for crude oil with viscosity greater than about 100cp. LaTorraca et al. (1998,1999) measured both T_1 and T_2 of viscous oil with a 2 MHz NMR spectrometer and found the two measurements had significant deviation above a viscosity of about 1,000 cp.

The T_1 and T_2 relaxation times for a number of crude oils and pure hydrocarbons are plotted as a function of viscosity and Larmor frequency (ω_0) in Fig. 1. The correlation of Morris, et al. (1997) is shown as the straight line. The pure alkanes differ from the low viscosity crude oils. However, if the alkanes remain saturated with air, the relaxation times of the alkanes reduce to values that are consistent with that of the light crude oils, Fig. 2. The interesting aspect of Fig. 1 is the difference between T_1 and T_2 for the viscous oils and the frequency dependence of this difference.

Relaxation Time Distributions

The T_1 and T_2 distributions of a number of crude oils were measured at 30°C with a 2 MHz NMR spectrometer. The T_2 was measured with $TE=0.24$ ms. Fig. 3-6 are representative relaxation time distributions of crude oils of decreasing API gravity. The T_1 and T_2 distributions of a 39° API gravity oil overlay each other and the distributions are symmetrical. A crude oil with 29° API gravity has a distribution that is skewed to short relaxation times and the T_2 distribution is slightly shorter than the T_1 distribution. The 19° API gravity crude oil has a T_2 distribution has a range of relaxation time that is clearly shorter than the T_1 distribution. The M14 oil was so viscous that the density and viscosity were not measured. The T_1 and T_2 distributions of this oil have separated.

Correlation of T_1/T_2

Our data was combined with that of LaTorraca, et al. and the ratio of the log mean T_1 and T_2 was correlated. The correlation shown in Fig. 7 has a correlation coefficient of 0.96. The ratio of the peaks of the distributions correlated with the asphaltene content is shown in Fig. 8. These latter two correlations are for NMR measurements at a ω_0 of 2

MHz. Vinegar, et al. only measured the T_1 relaxation time at a ω_0 of 80 MHz. However, if we assume that the T_2 is independent of ω_0 then the ratio T_1/T_2 , is dependent on both the viscosity and ω_0 .

The viscosity and frequency dependence of the ratio, T_1/T_2 , may be due to the relationship between the correlation time of molecular motions, τ_c , and ω_0 , Cowan (1997). In the limit of fast motions as in the case of low viscosity fluids, $\tau_c \omega_0 \ll 1$ and T_1 and T_2 are equal. When the molecular motions are slow as in high viscosity fluids or in macromolecules and/or the Larmor frequency is high, then $\tau_c \omega_0 \gg 1$ and T_1 will increase with increase in τ_c while T_2 will decrease. The T_1 data of Vinegar, et al. reaches a plateau with viscosity greater than about 100 cp. This may be because crude oils are mixtures of many components and have a distribution of correlation times.

CONCLUSIONS

Light oils have identical T_1 and T_2 relaxation time distributions. However, heavy or asphaltic crude oils have different T_1 and T_2 distribution with the ratio increasing with increasing viscosity, asphaltene content, and Larmor frequency.

REFERENCES

- Cowan, B. (1997), *Nuclear Magnetic Resonance and Relaxation*, Cambridge University Press, New York, pp. 232.
- Kleinberg, R.L. and Vinegar, H.J. (1996), "NMR Properties of Reservoir Fluids," *The Log Analyst*, Nov.-Dec., 20-32.
- LaTorraca, G.A., Dunn, K.J., Webber, P.R., and Carlson, R.M., (1998), "Low-Field NMR Determination of the Properties of Heavy Oils and Water-in -Oil Emulsions," *Magn. Resn. Imaging*, Vol. 16, No. 5/6, 659-662.
- LaTorraca, G.A., Stonard, S.W., Webber, P.R., Carlson, R.M., and Dunn, K.J. (1999) SPWLA 40th Ann. Logging Symp., May 30-June 3, paper PPP.
- Lo, S.-W., (1999) *Correlations of NMR Relaxation Time with Viscosity/Temperature, Diffusion Coefficient and Gas/Oil Ratio of Methane-Hydrocarbon Mixtures*, Ph.D. Thesis, Rice University.
- Morris, C.E., Freedman, R., Straley, C., Johnson, M., Vinegar, H.J., and Tutunjian, P.N. (1997), "Hydrocarbon Saturation and Viscosity Estimation from NMR Logging in the Belridge Diatomite," *The Log Analyst*, March-April, 44-59.
- Vinegar, H.J., Tutunjian, P.N., Edelstein, W.A., and Roemer, P.B. (1991), "Whole Core Analysis by ^{13}C NMR," *SPE Formation Evaluation*, (June), 183-189.

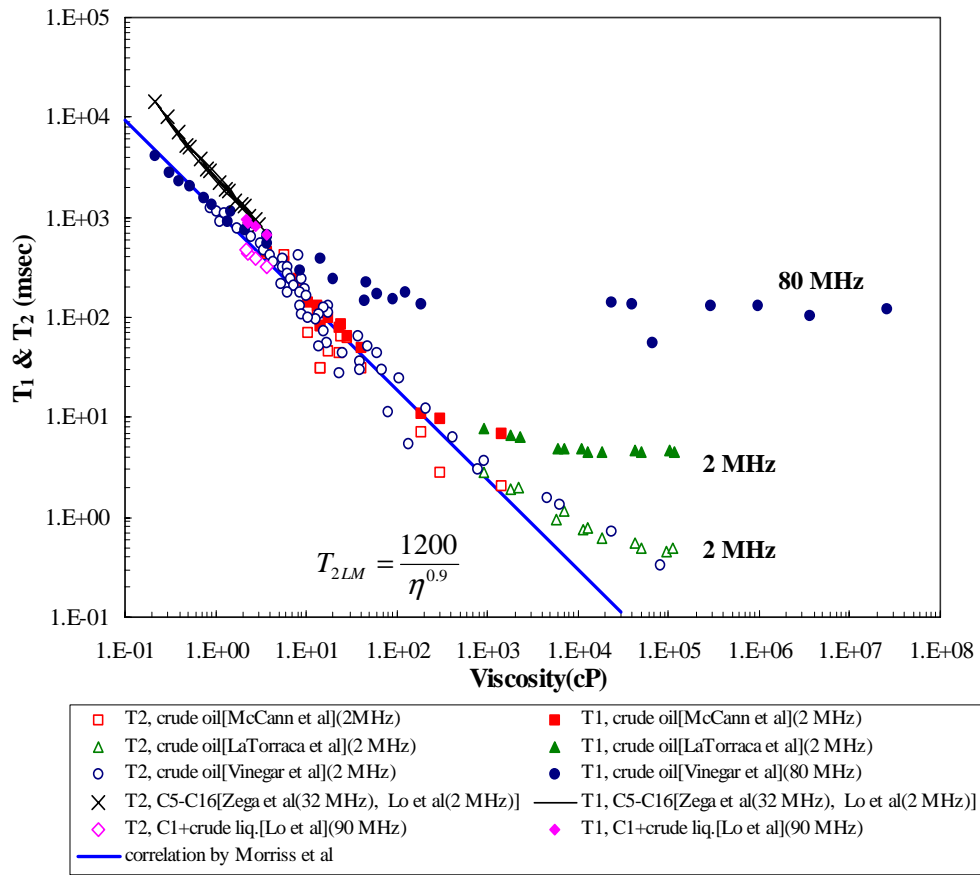


Fig. 1. T_1 and T_2 relaxation times as a function of viscosity and frequency.

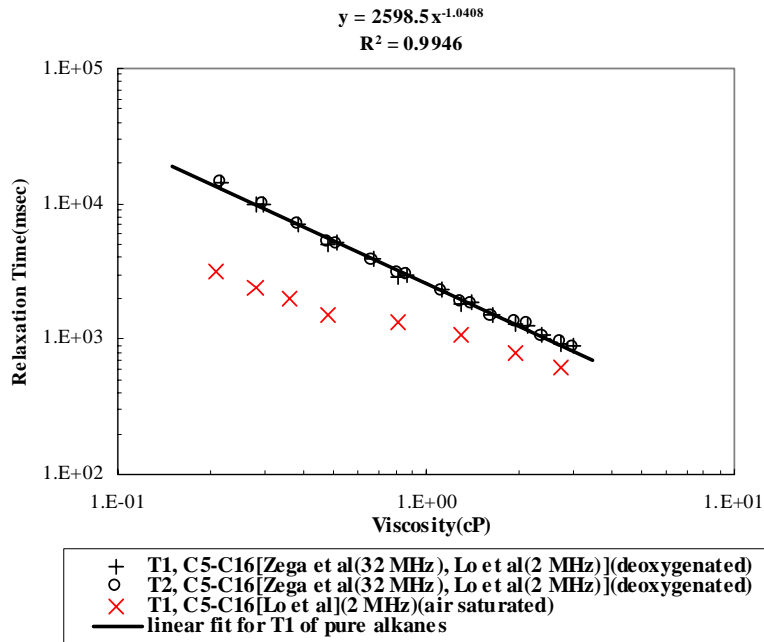


Fig. 2 Effect of oxygen on relaxation time of alkanes.

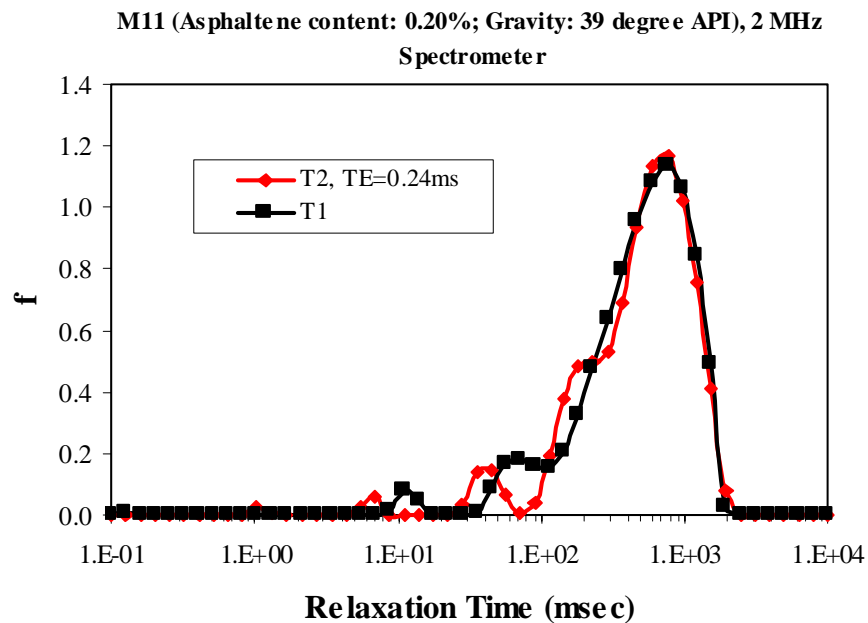


Fig. 3. Relaxation time distributions of a light oil.

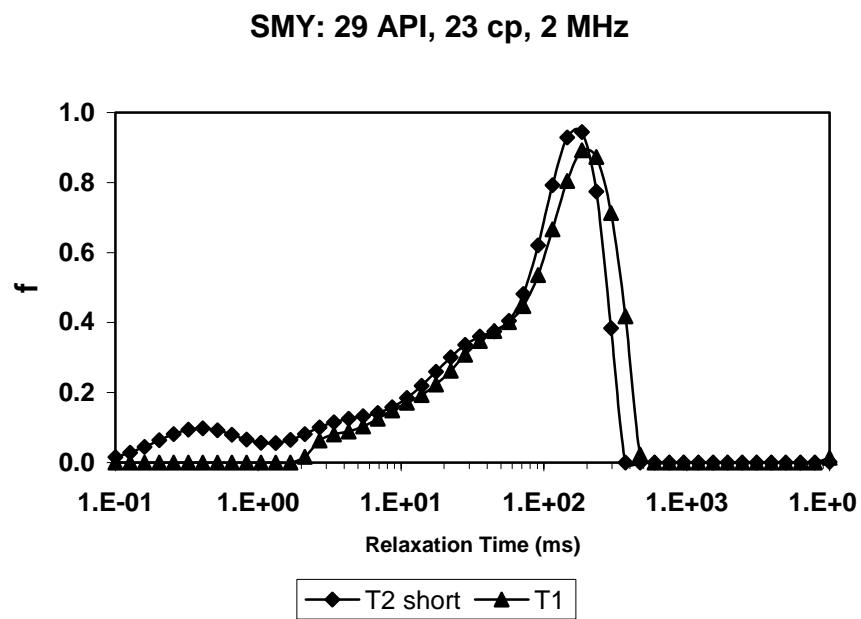


Fig. 4. Relaxation time distributions of a moderate gravity oil.

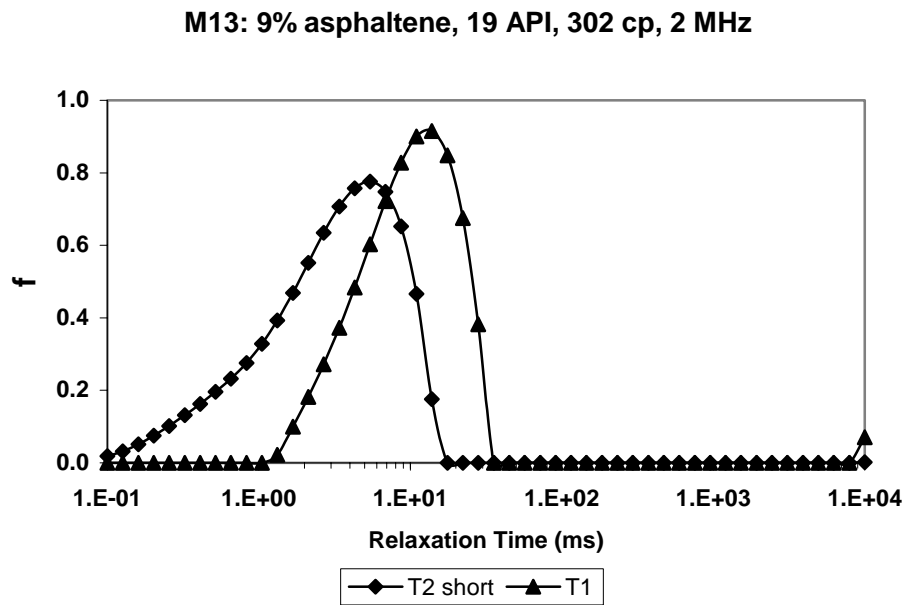


Fig. 5. Relaxation time distributions for a viscous oil

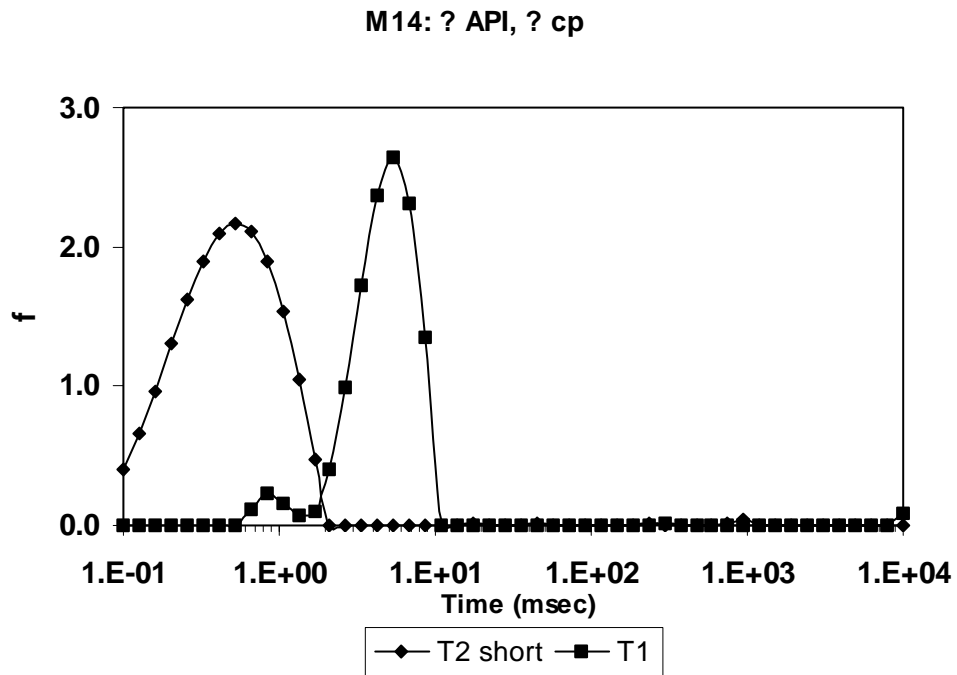


Fig. 6. Relaxation time distributions of a very heavy oil.

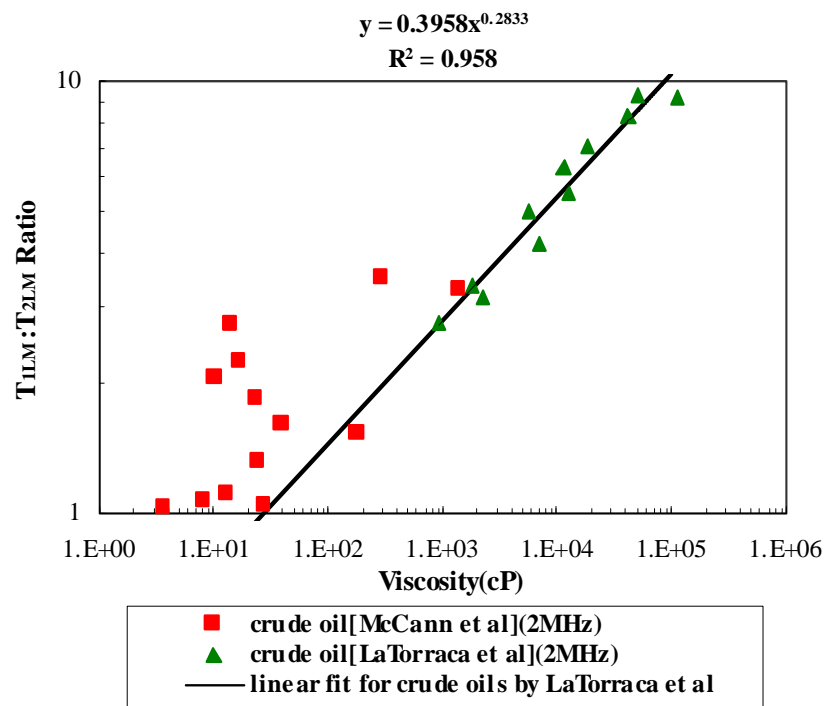


Fig. 7. Correlation of log mean T_1/T_2 with oil viscosity, 2 MHz

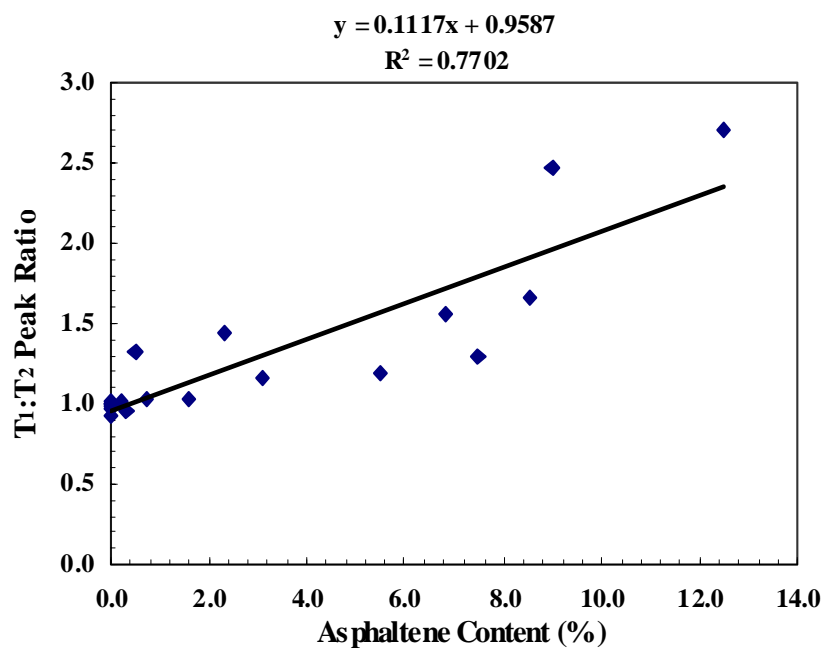


Fig. 8. Correlation of the peaks of the distributions with the asphaltene content, 2 MHz.

Task 2.0 Fluid-Rock Interactions

Study of slow diffusion in NMR relaxation of water in porous media

Jiansheng Chen

Abstract

In this paper, the Brownstein-Tarr theory is used to illustrate quantitatively the effects of slow diffusion in NMR relaxation of water in porous media. In the fast-diffusion region, the molecules diffuse so fast that the magnetization density remains uniform in the whole space of each single-pore and there is only one characteristic relaxation time for this pore. But in the slow-diffusion region, there exist several relaxation times for a single-pore, and calculation show that the sum of the relative intensities corresponding to the higher order ($n > 1$) relaxation times is about 17%, 25% and 32% for slab, cylinder and sphere geometry, respectively. When we consider the bulk relaxation in calculating the relaxation times, T_2 depends on another dimensionless group $a/(\rho \cdot T_{2B})$. When $a/(\rho \cdot T_{2B})$ is large, T_2 is equal to T_{2B} independent of the value of $\rho a/D$.

Introduction

The relaxation time of water in porous media is much shorter than that of bulk water due to surface relaxation. According to K. R. Brownstein and C. E. Tarr^(1,2), the magnetization decay of fluid in a single-pore can be described as a diffusion process characterized by the pore size parameter a (a is half the length between two slabs in the case of slab geometry and the radius in the case of cylinder and sphere geometry), surface relaxivity ρ and the self-diffusivity of the fluid D , the total magnetization $M(t)$ for a sample of volume V of water and surface S can be expressed as ⁽¹⁾:

$$M(t) = \iiint_V m(X, t) dV = M(0) \sum_{n=1}^{\infty} I_n \cdot \exp\left(-\frac{t}{T_n}\right) \quad (1)$$

$$T_n = \frac{a^2}{D \lambda_n^2} \quad (2)$$

Where $m(X, t)$ is the magnetization density and X is the z direction perpendicular to the surface (for slab) or the radial direction r (for cylinder and sphere). T_n are the relaxation times and I_n are the relative intensities.

For slab geometry:

$$m(z, t) = m_0 \cdot \sum_{n=1}^{\infty} \frac{4 \sin \lambda_n}{2\lambda_n + \sin 2\lambda_n} \cos\left(\frac{\lambda_n z}{a}\right) \exp\left(-\frac{D\lambda_n^2}{a^2} t\right) \quad (3)$$

$$I_n = \frac{4 \sin^2 \lambda_n}{\lambda_n (2\lambda_n + \sin 2\lambda_n)} \quad (4)$$

For cylindrical geometry:

$$m(r, t) = m_0 \cdot \sum_{n=1}^{\infty} \frac{2J_1(\lambda_n) \cdot J_0(\lambda_n r/a)}{\lambda_n (J_0^2(\lambda_n) + J_1^2(\lambda_n))} \exp\left(-\frac{\lambda_n^2 D}{a^2} t\right) \quad (5)$$

$$I_n = \frac{4J_1^2(\lambda_n)}{\lambda_n^2 (J_0^2(\lambda_n) + J_1^2(\lambda_n))} \quad (6)$$

For spherical geometry:

$$m(r, t) = m_0 \cdot \sum_{n=1}^{\infty} \frac{4(\sin \lambda_n - \lambda_n \cos \lambda_n)}{\lambda_n (2\lambda_n - \sin 2\lambda_n)} \frac{a \sin(\lambda_n r/a)}{r} \exp\left(-\frac{\lambda_n^2 D}{a^2} t\right) \quad (7)$$

$$I_n = \frac{12(\sin \lambda_n - \lambda_n \cos \lambda_n)^2}{\lambda_n^3 (2\lambda_n - \sin 2\lambda_n)} \quad (8)$$

The above results are given in reference (1) and are based on the assumption of constant surface relaxivity ρ and self-diffusivity D and without bulk relaxation. If we consider the bulk relaxation rate r_B , then the relaxation times become⁽³⁾

$$T_n = \left(r_B + \frac{D\lambda_n^2}{a^2} \right)^{-1} \quad (9)$$

In equation (2) to (9), λ_n are the eigenvalues such that⁽¹⁾

$$\text{for slab geometry} \quad \lambda_n \cdot \tan \lambda_n = \frac{\rho a}{D} \quad (10)$$

$$\text{for cylindrical geometry} \quad \frac{\lambda_n \cdot J_1(\lambda_n)}{J_0(\lambda_n)} = \frac{\rho a}{D} \quad (11)$$

$$\text{for spherical geometry} \quad 1 - \lambda_n \cdot \cot(\lambda_n) = \frac{\rho a}{D} \quad (12)$$

K. R. Brownstein and C. E. Tarr⁽¹⁾ showed that there exists three regions which depend on the dimensionless group $\rho a/D$:

- (a). fast-diffusion region: $\rho a/D \ll 1$.
- (b). intermediate-diffuison region: $1 < \rho a/D < 10$
- (c). slow-diffusion region: $\rho a/D \gg 10$

Low field NMR is a powerful and noninvasive technique in determining reservoir properties such as porosity, permeability, irreducible water saturation and pore size distribution. In the connection of relaxation time distribution with pore size distribution, it is usually assumed that it is in the fast-diffusion region, then for simple geometry,

$$\frac{1}{T_{1,2}} = r_B + \rho_{1,2} \frac{S}{V} = r_B + d \frac{\rho_{1,2}}{a} \quad (13)$$

Where $d=1, 2, 3$ for slab, cylindrical and spherical geometry, respectively. For spin-spin relaxation time T_2 , here it is assumed that field gradient and fluid diffusion effects are negligible. The same method can be used to determine the emulsion drop size distribution if the fast diffusion assumption holds. However, because of the diversity of the porous media with respect to surface relaxivity and pore dimensions, there are cases where we are in the slow-diffusion region or intermediate-diffusion region. The purpose of this paper is to see quantitatively the effects of slow diffusion using the Brownstein-tarr theory as illustrated above.

T_1, T_2 relaxation time distribution in slow diffusion region

Since the theoretical analysis in the introduction part applies to both T_1 and T_2 , here we only discuss T_2 and similar results apply to T_1 .

There exists T_2 relaxation time distribution for a rock sample because of pore size distribution even if each of the single-pore is in the fast-diffusion region. Similarly, for a single pore in the slow-diffusion region, there exists T_2 relaxation time distribution as shown in Figure 1 (a) and (b). In this case, the sum of the relative intensities corresponding to the higher order relaxation is about 17%, 25% and 32% for slab, cylinder and sphere geometry, respectively (Figure 2), so we can not use equation (13) to determined the pore size distribution.

Shown in Figure 3 (a), (b) and (c) is the Log Mean T_2 versus surface relaxivity, pore radius and fluid diffusivity, respectively. We can see that for small surface relaxivity (Figure 3 (a)), large pore radius (Figure 3 (b)) or small fluid diffusivity (Figure 3(c)), Log Mean T_2 is dominated by bulk relaxation time T_{2B} . Log Mean T_2 goes to a constant value when surface relaxivity becomes very large at fixed pore radius and fluid diffusivity (Figure 3 (a)) or when fluid diffusivity becomes very large at fixed surface relaxivity and pore radius (Figure 3 (c)). The Log Mean T_2 relaxation time is calculated by

$$T_{2LM} = \exp\left(\sum_{n=1}^m I_n \cdot \ln(T_{2n})\right) \quad (18)$$

Where I_n is the same as in equation (1), m is the number of terms we need to consider which depends on $\rho a/D$. The larger $\rho a/D$, the more terms are needed.

We can make Log Mean T_2 dimensionless by multiplying $(\rho \frac{S}{V} + \frac{1}{T_{2B}})$, after some calculations, we can get,

$$T_{2LM,D} = \exp\left(\sum_{n=1}^m I_n \cdot \ln\left(\frac{d + \frac{a}{\rho T_{2B}}}{\frac{a}{\rho T_{2B}} + \frac{D \lambda_n^2}{\rho a}}\right)\right) \quad (19)$$

Where T_{2B} is the bulk fluid relaxation time, the meaning of other parameters is the same as before. We found out that when we consider the bulk relaxation in calculating the decay times, the dimensionless Log mean T_2 depends on another dimensionless group $a/(\rho \cdot T_{2B})$ which is the ratio of bulk relaxation rate to surface relaxation rate.

Figure 4 and 5 shows the dimensionless Log Mean T_2 versus $\rho a/D$ and $a/(\rho \cdot T_{2B})$, respectively. Figure 6 is the corresponding contour plot. From Figure 4, 5 and 6 we can see that for each geometry, when $a/(\rho \cdot T_{2B})$ is large, which means that bulk relaxation dominates, the dimensionless Log Mean T_2 is equal to unity independent of the value of $\rho a/D$. When $a/(\rho \cdot T_{2B})$ is small, the dimensionless Log Mean T_2 increases with $\rho a/D$, which means that the higher order relaxation times become more and more important in calculating the dimensionless Log Mean T_2 . In Figure 6, there exist four regions in which different relaxation mechanism (bulk relaxation, diffusion and surface relaxation) dominates in different region. Detailed explanation is shown below the plot.

Conclusions

1. In the slow-diffusion region ($\rho a/D \gg 10$), there exists T_1 , T_2 relaxation time distribution for a single-pore, the sum of the relative intensities corresponding to the higher order relaxation times is about 17%, 25% and 32% for slab, cylinder and sphere geometry, respectively.
2. When we consider the bulk relaxation in calculating the decay times, the dimensionless Log mean T_2 depends on another dimensionless group $a/(\rho \cdot T_{2B})$. When $a/(\rho \cdot T_{2B})$ is large, the dimensionless Log Mean T_2 is equal to unity independent of the value of $\rho a/D$.

Reference:

1. K. R. Brownstein and C. E. Tarr, "Spin-Lattice relaxation in a system governed by diffusion," *J. Magn. Reson.* 26(17), 1977.
2. K. R. Brownstein and C. E. Tarr, "Importance of classic diffusion in NMR studies of water in biological cells," *Physical Review A*, 19 (6), 1979.
3. David J. Wilkinson, David Linton Johnson, and Lawrence M. Schwartz, "Nuclear magnetic relaxation in porous media: the role of the mean life time $\tau(\rho, D)$," *Physical Review B*, 44(10), 1991.
4. Tee-Lin Chuah. "Estimation of relaxation time distribution for NMR CPMG measurements". *MS Thesis*, Rice University, 1996.

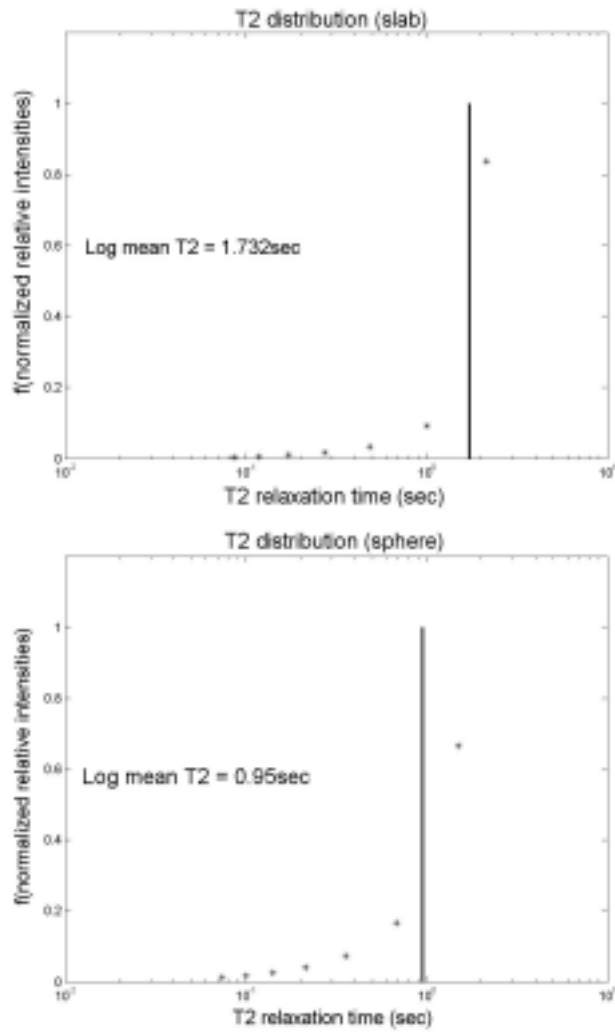


Figure 1 (a). T_2 relaxation time distribution calculated from analytical solution for a single-pore in the slow-diffusion region ($\rho a/D = 50$), the perpendicular line corresponds to Log Mean T_2 value calculated by equation (18).
 $a = 0.3\text{mm}$; $\rho = 416.7 \mu\text{m/sec}$;
 $D = 2.5 \times 10^{-5} \text{ cm}^2/\text{sec}$; $T_{2B} = 2.5\text{sec}$.

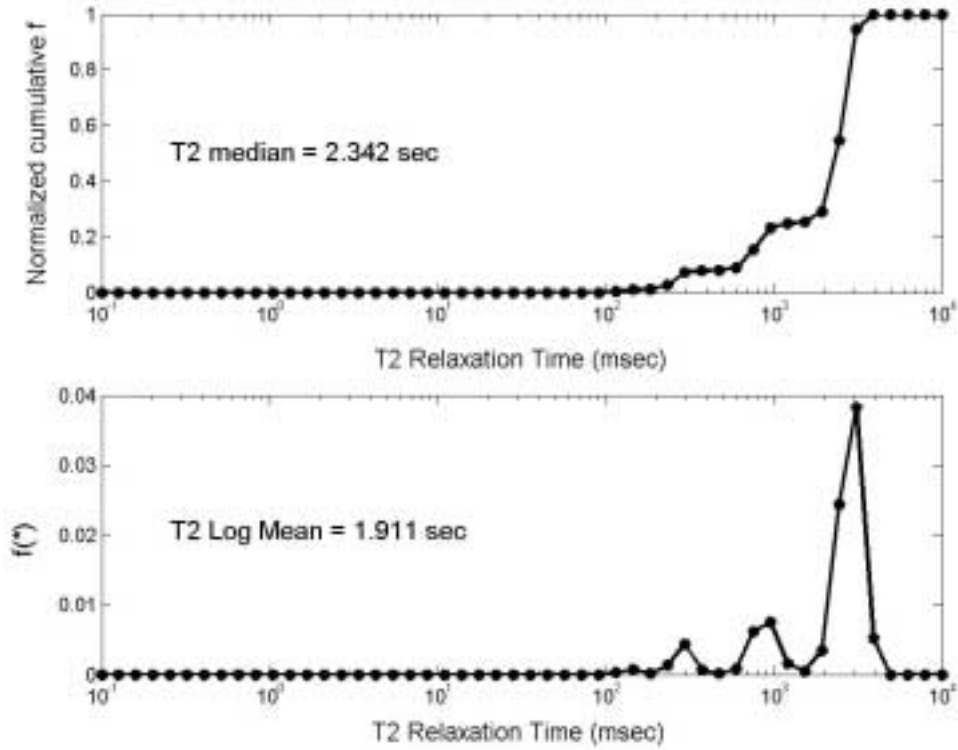


Figure 1(b) T_2 relaxation time distribution calculated by a non-negative non-linear least square inversion method developed in our laboratory⁽⁴⁾ for a single spherical pore in the slow-diffusion region ($\rho a/D=60$). Noise 0.00105%, Log Mean $T_2 = 1.911$ s and T_2 median =2.342s. $a = 0.3$ mm; $D = 2.5 \times 10^{-5}$ cm²/sec; $\rho = 500$ μ m/sec; $T_{2B}=2.5$ sec.

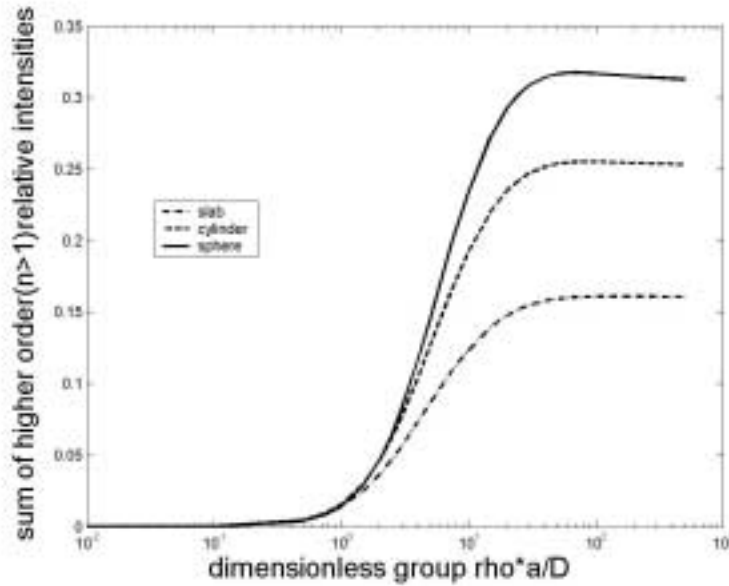
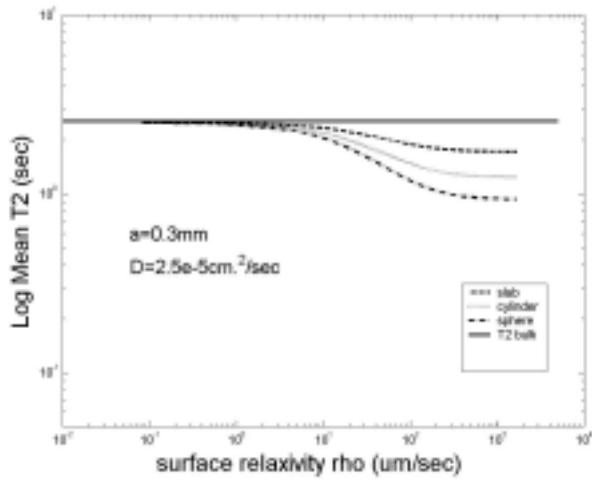
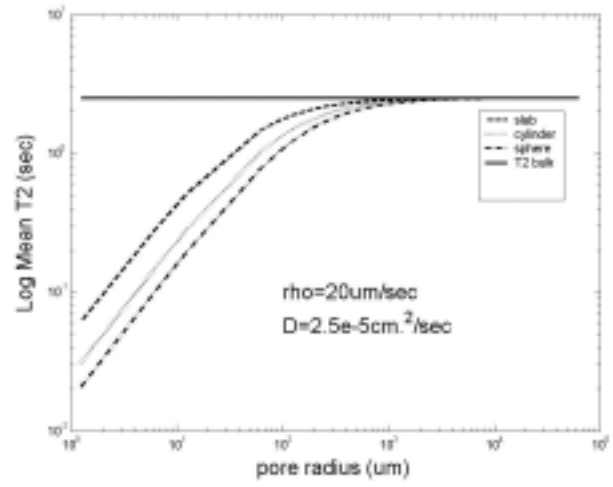


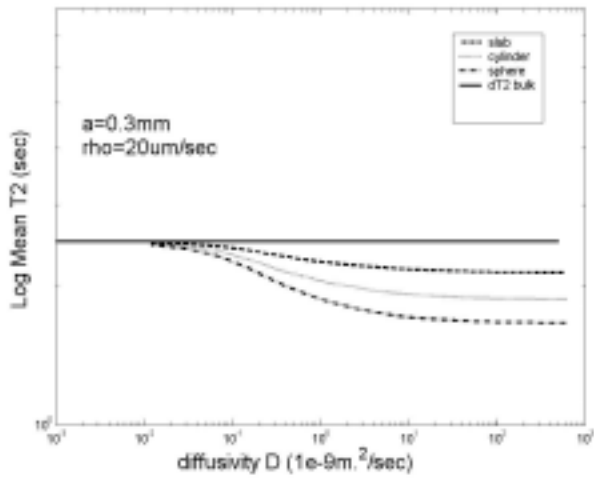
Figure 2. Sum of higher order relative intensities versus $\rho a/D$



(a)

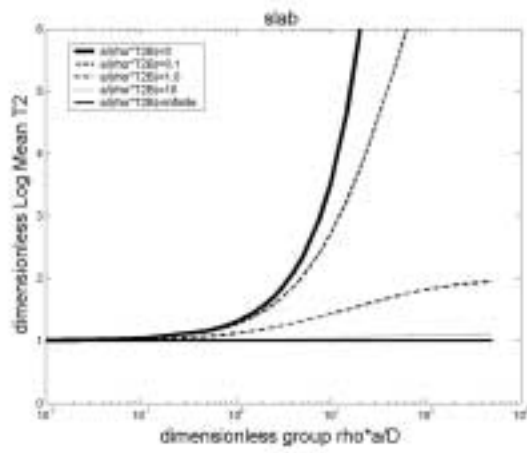


(b)

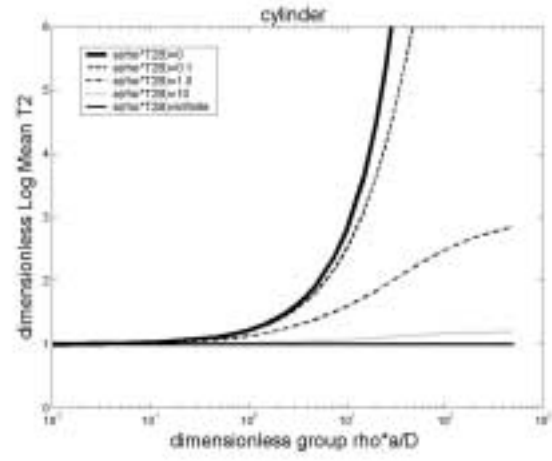


(c)

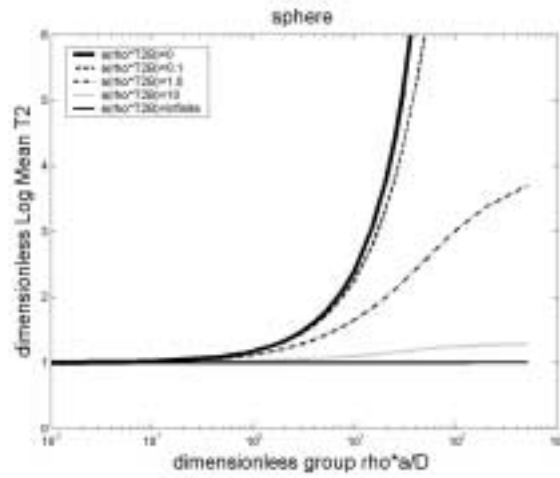
Figure 3. Log Mean T_2 versus surface relaxivity (a), pore radius (b) and diffusivity (c). The solid line corresponds to bulk relaxation time of water. $T_{2B} = 2.5\text{sec}$.



(a)

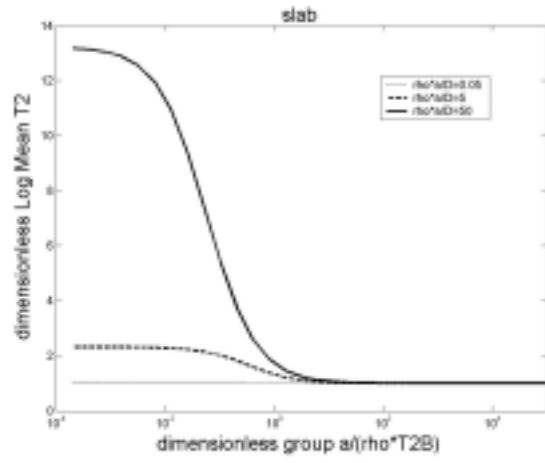


(b)

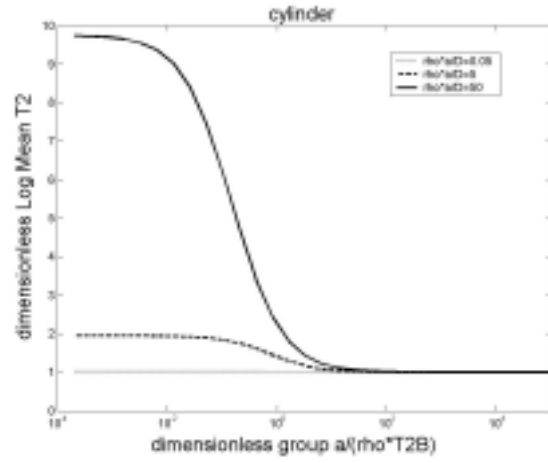


(c)

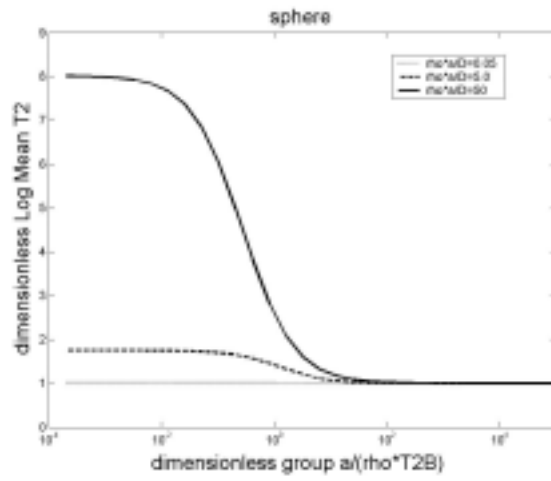
Figure 4. Dimensionless Log Mean T_2 versus $\rho a/D$. (a), (b), (c) corresponds to slab, cylinder and sphere geometry, respectively.



(a)

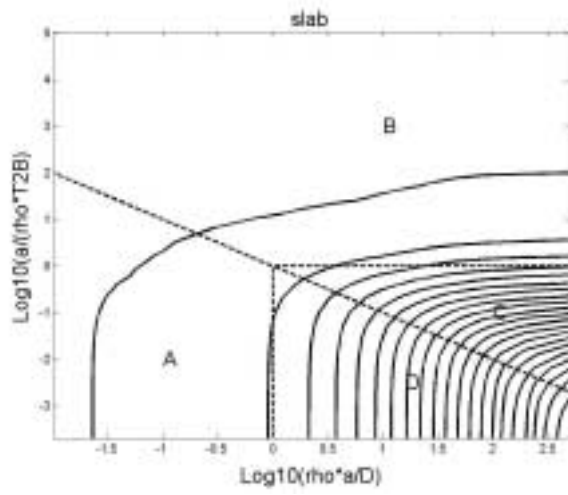


(b)

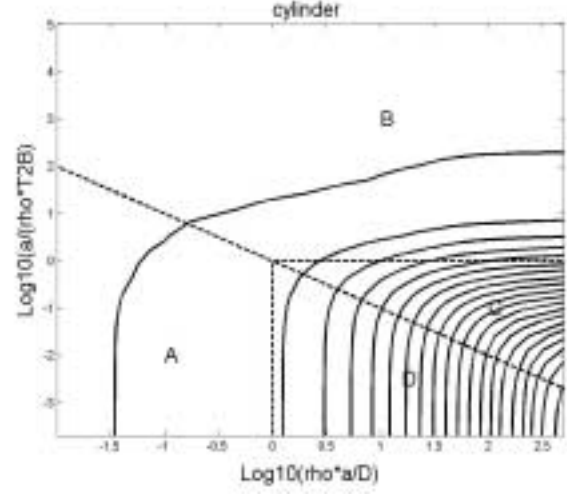


(c)

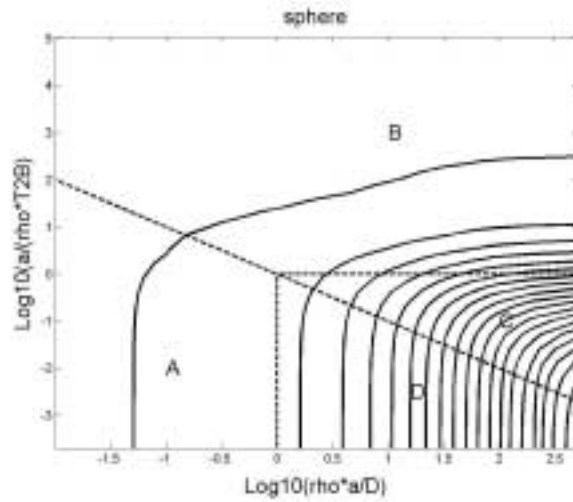
Figure 5. Dimensionless Log Mean T_2 versus dimensionless group $a/(\rho \cdot T_{2B})$. (a), (b), (c) corresponds to slab, cylinder and sphere geometry, respectively.



(a)



(b)



(c)

Figure 6. Contour plot of Dimensionless Log Mean T_2 with respect to dimensionless group $\rho a/D$ and $a/(\rho^* T_{2B})$. (a), (b), (c) corresponds to slab, cylinder and sphere geometry, respectively. In each plot, the dimensionless Log mean T_2 goes to unity (the first line at the top corresponds to $T_{2LM,D} = 1.01$) when approaching upper and left sides and it geometrically (geometric ratio is 1.2589) goes to big values when approaching lower right corner. The center dash line corresponds to characteristic diffusion time equals bulk relaxation time ($a^2/(D^* T_{2B})=1$), the perpendicular dash line corresponds to characteristic diffusion time equals surface relaxation time ($\rho a/D=1$) and the parallel dash line corresponds to bulk relaxation time equals surface relaxation time ($a/(\rho^* T_{2B})=1$). These three lines divide the plot into four regions. A, D: diffusion rate dominates bulk relaxation rate and from A to D surface relaxation becomes more and more important. B, C: bulk relaxation rate dominates diffusion rate and from B to C surface relaxation becomes more and more important.

CPMG Relaxation by Diffusion with Constant Magnetic Field Gradient in a Restricted Geometry: Numerical Simulation and Application

ABSTRACT

Carr-Purcell-Meiboom-Gill (CPMG) measurements are the primary NMR technique used for evaluating formation properties and reservoir fluids in well logging and laboratory sample analysis. The estimation of bulk volume irreducible (BVI), permeability, and fluid typing relies on the accurate interpretation of the T_2 distribution. The problem is complicated when diffusion in an inhomogeneous field and restricted geometry becomes dominant. The combined effects of field gradient, diffusion, and restricted geometry are not easily evaluated analytically. We used a numerical method to evaluate the dependence of free and restricted diffusion on the system parameters in the absence of surface relaxation, which usually can be neglected for the non-wetting fluids (e.g., oil or gas). The parameter space that defines the relaxation process is reduced to only two dimensionless groups: D^* and τ^* . Three relaxation regimes: free diffusion, localization, and motionally averaging regimes are identified in the $(\log_{10} D^*, \log_{10} \tau^*)$ domain. The hypothesis that the dimensionless normalized magnetization ϕ^* relaxes as a single exponential with a constant dimensionless relaxation time T_2^* is justified for most regions of the parameter space. The analytical and numerical solutions are compared from the contour plots of T_2^* . The location of the boundaries between different relaxation regimes defined in the analytical analysis is challenged by the numerical results. After adjustment of boundaries, numerical simulation results and analytical solutions match each other for every relaxation regime except for near the boundaries. The parameters, fluid diffusivity and pore length, can be estimated from analytical solutions in the free diffusion and motionally averaging regimes, respectively. Estimation of the parameters near the boundaries of the regimes may require numerical simulation.

INTRODUCTION

Carr-Purcell-Meiboom-Gill (CPMG) pulse sequence, as shown in Fig. 1, is widely used to measure spin-spin relaxation time T_2 . After the initial $\frac{\pi}{2}$ pulse, spins at different locations rotate around the z axis by differing amounts due to the field inhomogeneity. A π pulse is applied (around the rotating imaginary axis) at time τ to refocus the spins, which leads to the formation of the “Hahn” echo at time 2τ . Then further application of π pulses at 3τ , 5τ ..., the odd multiples of τ , leads to formation of the CPMG echoes at 4τ , 6τ ..., the even multiples of τ . Only when spins are not diffusing, can CPMG completely compensate the dephasing of spins due to local magnetic field inhomogeneity.

Many researchers studied the decay of the CPMG spin echo amplitude resulting from the combined effects of field gradients, diffusion, and restricted geometries

(Kleinberg and Horsfield, 1990, Le Doussal and Sen, 1992, Brown and Fantazzini, 1993, Bergman and Dunn, 1995, Bergman et al., 1995, and Axelrod and Sen, 1998).

Axelrod and Sen (1998) worked out various limiting cases, as well as intermediate cases for CPMG signals based on eigen function expansion.

Hürlimann (1998) showed that the pores can be classified into large or small pores, by comparing the pore size to $\sqrt{D_0/\gamma\Delta\chi B_0}$. Only the contributions from the large pores show a significant increase of the CPMG decay rate with echo spacing TE.

Sen et al. (1999) studied the influence of restriction on CPMG spin echo response of magnetization of spins diffusing in a bounded region in the presence of a constant magnetic field gradient. Depending on three main length scales: L_D diffusion length, L_g dephasing length, and L_s system length, three main regimes of decay have been identified: free diffusion, localization and motionally averaging regimes. They conducted numerical simulations to investigate how spins pass from one regime of relaxation to another, and more particularly the passage from the localization regime to the motionally averaging regime. In this intermediate regime, they observed large oscillations in the CPMG signal as a function of the echo number for certain specific values of the time between pulses and the magnetic field gradient.

In this paper, we will conduct numerical simulation to study the combined effects of field gradient, diffusion, and restricted geometry on NMR measurements.

NUMERICAL METHOD

System of Study

The internal field gradient induced from the magnetic susceptibility difference between pore fluids and solid matrix can have a very complicated distribution in natural sandstones (Zhang et al., 2000). Thus, determination of the NMR response of the magnetization of spins for real systems is a very difficult task. We need to first restrict ourselves to the most fundamental yet important case, i.e., a 1-D system in a magnetic field with constant gradient. Only after thorough understanding of such ideal system, should we proceed to more realistic systems.

Therefore, as illustrated in Fig. 2, we define our system of study as a 1-D pore (i.e., a slab) along x (real) axis. The pore is divided into m grid blocks, each represented by a grid point. Also, we only consider a magnetic field with a constant gradient, i.e., $B_z = B_0 + gx$. Spins are free to diffuse through the pore space.

System of Equations

We can get the following equation only after a few mathematical manipulations on the original Torrey's equations (Torrey, 1956):

$$\frac{\partial M}{\partial t} = -i\gamma B_z M - \frac{M}{T_2} + D_0 \nabla^2 M \quad [1]$$

where M is magnetization expressed as a complex variable, $M = M_x + iM_y$. Let $M = \varphi \cdot e^{\left(-i\omega_0 t + \frac{-t}{T_{2B}}\right)}$, then φ represents the magnetization with the precession at Larmor frequency, $\omega_0 = \gamma B_0$, and bulk relaxation, T_{2B} , factored out.

In addition, introduce normalized magnetization $\varphi^* = \frac{\varphi}{\varphi_0}$, where φ_0 is the magnetization at time zero. Then, at $t = 0$, $\varphi^* = 1$. Hence Eq. [1] becomes:

$$\frac{\partial \varphi^*}{\partial t} = -i\gamma(B_z - B_0)\varphi^* + D_0 \nabla^2 \varphi^* \quad [2]$$

For our system of study, i.e., a 1-D pore with constant gradient and spin diffusion, Eq. [2] becomes:

$$\frac{\partial \varphi^*}{\partial t} = -i\gamma g x \varphi^* + D_0 \frac{\partial^2 \varphi^*}{\partial x^2} \quad \text{for } -\frac{L_s}{2} < x < \frac{L_s}{2} \text{ and } t > 0 \quad [3]$$

Let $x^* = \frac{x}{L_s}$, where L_s is system length, and $t^* = \frac{t}{t_0}$. The characteristic time, t_0 , is also called the dephasing time and it is defined as $t_0 \equiv \frac{1}{\gamma g L_s}$, in unit of time/radian. t_0 represents the time it takes for the spins at $x^* = -\frac{1}{2}$ and $x^* = \frac{1}{2}$ to dephase by 1 radian due to the magnetic field inhomogeneity. A typical value of t_0 is 1.5 msec/radian (with $\gamma = 2.675 \times 10^8$ radians/(Tesla*sec), $g = 25$ gauss/cm, and $L_s = 10 \mu\text{m}$).

Eq. [3] is now

$$\frac{\partial \varphi^*}{\partial t^*} = -ix^* \varphi^* + \frac{D_0}{\gamma g L_s^3} \cdot \frac{\partial^2 \varphi^*}{\partial x^{*2}} \quad [4]$$

We introduce a dimensionless group D^* , defined as:

$$D^* \equiv \frac{D_0}{\gamma g L_s^3} = \frac{1}{\gamma g L_s} \cdot \frac{1}{\left(\frac{L_s^2}{D_0}\right)} = \frac{\text{"dephasing time"}}{\text{"diffusion time"}}$$

It is the ratio of dephasing time in an inhomogeneous field and diffusion time across a pore of length L_s .

With the definition of D^* , Eq. [4] becomes:

$$\frac{\partial \varphi^*}{\partial t^*} = -ix^* \varphi^* + D^* \frac{\partial^2 \varphi^*}{\partial x^{*2}} \quad [5a]$$

The initial condition is:

$$\varphi^*(x^*, t^* = 0) = 1 \quad [5b]$$

For boundary condition, we assume completely reflective pore walls for the time being. That is, there is no surface relaxation. This assumption is usually true for non-wetting fluids (e.g., oil or gas). Then the boundary condition is:

$$\frac{\partial \varphi^*}{\partial x^*} = 0 \quad \text{at } x^* = -\frac{1}{2} \text{ and } \frac{1}{2} \quad [5c]$$

Since CPMG pulse sequence has π pulses at odd numbers of τ : $\tau, 3\tau, \dots$, we introduce another dimensionless group τ^* , defined as $\tau^* = \frac{\tau}{t_0} = \tau \gamma g L_s$. Then, at $t^* = \tau^*$, $3\tau^*, \dots$, a π pulse is applied.

At each π pulse, the spins are rotated 180° about the y' (rotating imaginary) axis, thus immediately after the π pulse every spin has the same imaginary component, while negative real component, as it has immediately before the π pulse. Therefore, the effect of a π pulse can be expressed as the negative of complex conjugate, i.e.:

$$\varphi_{\pi_+}^* = -\overline{(\varphi_{\pi_-}^*)} \quad [5d]$$

where π_- and π_+ stand for at time immediately before and after a π pulse.

Thus far, the diffusion problem is completely mathematically formulated by system of equations [5a] to [5d].

Finite Difference

For numerical stability and second order convergence, we use Crank-Nicholson finite difference method to solve the system of equations [5a] to [5d].

In simple matrix form, Eq. [5a] combined with boundary condition [5c] for all the grid blocks is:

$$A \varphi^{*N+1} = B \varphi^{*N} \quad [6]$$

where A and B are $m \times m$ tri-diagonal matrices and φ^{*N+1} and φ^{*N} are $m \times 1$ matrices at time step t_{N+1}^* and t_N^* , respectively. Eq. [6] is fully expanded as:

$$\begin{bmatrix}
\frac{h^2}{\Delta t^*} + \theta \cdot i h^2 x_1^* + D^* \theta & -D^* \theta & & & \\
& \dots & & & \\
& & -D^* \theta & \frac{h^2}{\Delta t^*} + \theta \cdot i h^2 x_j^* + 2D^* \theta & -D^* \theta \\
& & & \dots & \\
& & & & -D^* \theta & \frac{h^2}{\Delta t^*} + \theta \cdot i h^2 x_m^* + D^* \theta
\end{bmatrix}
\begin{bmatrix}
\varphi_1^{*N+1} \\
\varphi_2^{*N+1} \\
\dots \\
\varphi_{m-1}^{*N+1} \\
\varphi_m^{*N+1}
\end{bmatrix} =
\begin{bmatrix}
\frac{h^2}{\Delta t^*} - (1-\theta) i h^2 x_1^* - D^*(1-\theta) & D^*(1-\theta) & & & \\
& \dots & & & \\
& & D^*(1-\theta) & \frac{h^2}{\Delta t^*} - (1-\theta) i h^2 x_j^* - 2D^*(1-\theta) & D^*(1-\theta) \\
& & & \dots & \\
& & & & D^*(1-\theta) & \frac{h^2}{\Delta t^*} - (1-\theta) i h^2 x_m^* - D^*(1-\theta)
\end{bmatrix}
\begin{bmatrix}
\varphi_1^{*N} \\
\varphi_2^{*N} \\
\dots \\
\varphi_{m-1}^{*N} \\
\varphi_m^{*N}
\end{bmatrix}$$

where, $h = \Delta x^* \equiv x_{j+1}^* - x_j^* = \frac{1}{m}$, $\Delta t^* = t_{N+1}^* - t_N^*$, and $\theta = 0.5$.

To save computational time, we follow the same procedure as in Sen's paper (Sen et al., 1999) to skip calculating φ^* at the intermediate micro steps but rather calculate φ^* at echo time $t^* = 2n\tau^*$, where n is echo number starting from 1.

Rewrite Eq. [6] as: $\varphi^{*N+1} = U\varphi^{*N}$, where $U = A^{-1}B$, the time evolution matrix for a single micro time step $\Delta t^* = t_{N+1}^* - t_N^*$. Let the number of micro steps in each τ^* (or τ) interval be N_τ , i.e., $N_\tau = \frac{\tau^*}{\Delta t^*}$. The dimensionless normalized magnetization immediately before the first π pulse is: $\varphi^{*N_\tau} = U^{N_\tau} \varphi^{*0}$, where $\varphi^{*0} = 1$ is the initial condition. Define $V_1 = U^{N_\tau}$ and $V_2 = \overline{(U^{N_\tau})}$. The effect of a π pulse is negative conjugate and we assume that the pulse length is infinitesimally small. Then, at $t^* = 2\tau^*$, when the Hahn echo forms, $\varphi^{*2N_\tau} = U^{N_\tau} \left[-\overline{(\varphi^{*N_\tau})} \right] = V_1 V_2 (\varphi^{*0})$. Similarly, the recursive formula for all the echoes is:

$$\varphi^{*n} = V_1 V_2 (\varphi^{*n-1})$$

where n is echo number starting from 1. Therefore the matrix $V_1 V_2$ needs to be computed only once and it multiplies the solution from one echo to the next.

It is obvious from the system of equations that CPMG in 1-D system with constant gradient and spin diffusion is solely governed by two dimensionless groups: D^* and τ^* . We choose a domain of D^* (ranging from 10^{-4} to 10^2) and τ^* (ranging from 10^{-1} to $10^{1.5}$), which covers typical combinations of the dimensional parameters: D , g , L_S , and τ that are often encountered in real systems. A mesh grid of 121 by 121 points on the $(\log_{10} D^*, \log_{10} \tau^*)$ domain is chosen.

To get accurate numerical simulation results, we need to have large numbers of grid blocks and small time step size in order to reach acceptable levels of spatial and time truncation errors for the whole $(\log_{10} D^*, \log_{10} \tau^*)$ domain. It is founded that 99 grid blocks and 512 time steps in each τ^* interval are sufficient for all regions on the $(\log_{10} D^*, \log_{10} \tau^*)$ domain.

REGIMES OF THE PARAMETER SPACE

By the way we define the system of equations, there are only two dimensionless groups: D^* and τ^* in the parameter space. Whereas, in the literature (deSwiet and Sen, 1994, Helmer et al., 1995, and Hürlimann et al., 1995), NMR signal of nuclear magnetization due to restricted diffusion in an inhomogeneous magnetic field is often characterized by three length scales. They are: the system length, L_s , the diffusion length

$L_D \equiv \sqrt{D_0 \tau}$, and the dephasing length $L_g \equiv \left(\frac{D_0}{\gamma g} \right)^{\frac{1}{3}}$. The diffusion length is a measure of the distance traveled by a spin in the half echo time τ . The dephasing length is the length over which a spin has to diffuse to dephase by 1 radian. In this way, three ratios of these three length scales will be needed to completely describe the diffusion problem. Therefore, we reduce the number of parameters from three to two, which is an important improvement that makes the problem much more simple and direct.

Three relaxation regimes based on the smallest length scales are identified and their governing analytical equations are given in the literature. A brief summary of these analytical results is given below, where the original analytical equations are expressed in our newly-defined two parameters: D^* and τ^* .

1. Free diffusion regime:

L_D is the smallest of the three length scales. Spins are undergoing unrestricted, free diffusion (applies only to the shortest times), as described by Hahn's formula (Hahn, 1950):

$$\frac{M(2n\tau)}{M(0)} = e^{-(2/3)nD^*\tau^{*3}} \quad [7]$$

When considering short times after a few spins make contact with the pore walls, Hahn's formula needs to be corrected to the first order due to the wall effect (deSwiet and Sen, 1994 and Sen et al., 1999):

$$\frac{M(2n\tau)}{M(0)} = e^{-(2/3)D^*\tau^{*3} \left[n + C(n)\sqrt{D^*\tau^*} \right]} \quad [8]$$

where $C(n)$ are numerical constants and depend on the echo number n .

2. Localization regime:

L_g is the smallest of the three length scales. The main characteristic of this regime is that the net signal comes principally from the spins which are within one dephasing length of the boundaries. The attenuation of nuclear magnetization in this regime is given by (deSwiet and Sen, 1994, Hürlimann et al., 1995, and Sen et al., 1999):

$$\frac{M(2n\tau)}{M(0)} = p(n)D^{*3}e^{-a_1nD^{*\frac{1}{3}}\tau^*} \quad [9]$$

where the numerical constants $p(n)$ are for the values of gradient away from the branch points (Stroller et al., 1991).

3. Motionally averaging regime:

L_s is the smallest of the three length scales. The spins typically diffuse several times the pore size, and any magnetic field inhomogeneities are averaged out by their motion. The signal decays according to (Sen et al., 1999):

$$\frac{M(2n\tau)}{M(0)} = \exp\left\{-\frac{n}{60}\frac{\tau^*}{D^*}\times\left[1-\frac{17}{112}\frac{2n+1}{3n}\frac{1}{D^*\tau^*}\right]\right\} \quad [10]$$

One advantage of expressing the diffusion problem with two (D^*, τ^*) dimensionless groups instead of three (L_D, L_g, L_s) length scales is that these three relaxation regimes can be easily shown on the $(\log_{10} D^*, \log_{10} \tau^*)$ domain. As illustrated in Fig. 3, three lines, that correspond to the equality between any two length scales (Table 1), divide the domain into six regions and they intersect at point $O(0,0)$ (in log-log scale). The inequality of the three length scales is listed for each region on the figure. Region BCDO has L_D as the smallest length scale, so it is the free diffusion regime described by Eqs. [7] & [8]. Region ABOG has L_g as the smallest, so it is the localization regime governed by Eq. [9]. Region GODEF has L_s as the smallest, so it is the motionally averaging regime expressed by Eq. [10]. The boundaries between different regimes are marked as solid lines, while dashed lines are extension of these boundaries. Table 2 summarizes these results.

NUMERICAL RESULTS

People usually study the decay of magnetization along time scale or as a function of echo number (Sen et al., 1999). Then contour plots of φ^* need to be created at a series values of time to understand the whole relaxation process. Alternatively, we hypothesize that φ^* relaxes exponentially with t^* , characterized by a constant relaxation time T_2^* :

$$\varphi^*(t^*) = e^{-\frac{t^*}{T_2^*}}$$

where T_2^* is not apparent relaxation time in FID measurement. It is defined as the dimensionless relaxation time with respect to the dephasing time, i.e., $T_2^* = \frac{T_2}{t_0}$. This T_2^* is solely due to the diffusion relaxation mechanism. This is because the bulk relaxation is factored out in the beginning to get ϕ from M and in the current study, we assume there is no surface relaxation on the pore wall.

If T_2^* does not change with time, then the relaxation of magnetization can be described by a single exponential. Figure 4 compares contour lines of T_2^* at two different times. Solid curves are at $t^* = 80$, while dashed curves are ten times later in time, i.e., at $t^* = 800$. Remarkably, except for the left portion of region ABOG, the contour lines of T_2^* at these two times overlay on each other very well. This means that for most region in the domain, ϕ^* decays single exponentially. The significance of this finding is that now only one single contour plot of T_2^* , no matter at what time, is enough to describe the whole relaxation process.

The contour lines of T_2^* at $t^* = 400 \times (2\tau_{\min}^*) = 80$, the solid curves on Fig. 4, will represent the numerical simulation results referred to in later discussion. This time is when the bottom of the domain, CDE, has the 400th echo. Ten contour lines are picked logarithmically from $T_2^* = 10$ to $T_2^* = 10000$. Small T_2^* value means fast relaxation and large T_2^* value corresponds to slow relaxation. Three boundaries between the free diffusion, localization, and motionally averaging regimes are also shown as solid lines.

The contour lines of T_2^* are V-shaped over most of the domain. In the region of BCDO, at smaller D^* , straight lines with slope about $-\frac{1}{2}$ are observed. Then at larger D^* , contour lines turn and curve up. The left portion of region ABOG has wiggling curves, while the right portion has vertical and equally spaced curves that curve a little at the bottom to connect with the curves in region BCDO. In region GODEF, there are curves that almost vertical throughout the τ^* range.

COMPARISON OF NUMERICAL SIMULATION RESULTS WITH ANALYTICAL SOLUTION

In the section REGIMES OF THE PARAMETER SPACE, we listed the analytical equations (Eq. [7] to [10]) that describe the three asymptotic regimes of relaxation. In this section we will compare our numerical simulation results with each of them. Contour lines of T_2^* from analytical equation will be shown only for the region where it applies and in the central main plot, while the numerical simulation results will be shown for comparison at the corner.

Figure 5 compares the contour lines of T_2^* from Eq. [7], which is for the free diffusion regime in region BCDO, and those from numerical simulation results. Contour

lines of T_2^* from analytical equation are straight lines with slope $-\frac{1}{2}$. By overlaying with the numerical simulation results, it can be concluded that the straight line portion of the numerical results matches very well with the analytical solution.

Eq. [8] of the free diffusion regime also applies to region BCDO, where L_D is the smallest. It is the first order correction to Eq. [7] to account for the partial wall effect. Figure 6 shows the contour lines of T_2^* from Eq. [8] for region BCDO and the numerical simulation results. At smaller D^* , the straight line part of Eq. [8] is similar to that of Eq. [7] but with a slope not exactly equal to $-\frac{1}{2}$. Then at larger D^* , the contour lines begin to curve up. Eq. [8] reaches its limit of validity near boundary OD. When comparing numerical simulation results with analytical solution, the contour lines qualitatively match with each other with numerical simulation predicting turning points at smaller D^* values.

Figure 7 shows the contour lines of T_2^* from Eq. [9] plotted for the localization region ABOG and those from numerical simulation. Unlike analytical solution, contour lines of numerical simulation results curve up at larger D^* . There is apparent discrepancy between the numerical result and analytical solution.

Figure 8 plots contour lines of T_2^* from Eq. [10] for region GODEF and those from numerical simulation. Vertical lines with slight curvature at the bottom are observed. Numerical result and analytical solution match with each other very well.

ADJUSTMENT OF BOUNDARIES BETWEEN RELAXATION REGIMES

Thus far, only region ABOG has apparent discrepancy between numerical result and analytical solution of Eq. [9].

Let us examine Fig. 7 more carefully. Suppose we draw a dividing line in region ABOG of the numerical simulation results, shown as the dashed line, it can be observed that the left portion of this region looks similar to the analytical solution with wiggling contour lines. In addition, the right portion of this region looks like the extension of the motionally averaging regime showing the same feature of vertical, equally spaced contour lines with slight curvature at the bottom to meet curves in the free diffusion regime. Therefore, we hypothesize that the region of motionally averaging regime should be extended to smaller D^* values.

What is this line then? Can we justify the position of it? Recall that the numerical constants $p(n)$ in Eq. [9] are for the values of gradient away from the branch points. Briefly speaking, with magnetic field gradient $g = 0$, the eigenvalues of the diffusion problem, Eq. [5a], are real. As g increases along the positive real axis, eigenvalues shift, and successive pairs of real-valued eigenvalues coalesce at branch points to form complex conjugate pairs. The branch points occur at special values of the gradient, which

in our notation, correspond to certain values of D^* , i.e., $\log_{10} D^* = [-1.257 \ -2.363 \ -2.829 \ -3.123 \ -3.358 \ -3.522 \ -3.667]$.

Figure 9 plots these vertical branch point lines on the $(\log_{10} D^*, \log_{10} \tau^*)$ domain. Notice that the line we proposed that Eq. [10] should be extended to coincides with the first branch point, i.e., $\log_{10} D^* = -1.257$. The remaining branch point lines are to the left side of this line.

Previous researchers (Stoller et al., 1991 and deSwiet and Sen, 1994) have found that oscillations in the echo signal become large near branch points. In the left portion of region ABOG which is densely distributed with branch point lines, we also observe wiggling contour lines from numerical simulation. Therefore, our numerical simulation is consistent with other researchers' observation.

Figure 4 in Sen's paper (Sen et al., 1999) also supports our hypothesis that the portion of region ABOG that is to the right side of the first branch point line should be motionally averaging regime instead of localization regime. In that figure, Sen had $\log_{10} D^* = -0.984$ greater than the first branch point value of -1.257 . He also had the parameters chosen such that L_g is the smallest length scale. So, in our notation, the point he calculated lies within the localization region ABOG and to the right of the first branch point line. However, his simulation result matched perfectly well with the analytical equation for the motionally averaging regime, instead of that for the localization regime. Thus, this gives support to our hypothesis that Eq. [10] should be used to the right of the first branch point line.

As the final support to our hypothesis, Fig. 10 shows the contour lines of T_2^* from Eq. [10] up to the first branch point line HI. The numerical simulation results are also shown for comparison at the lower left hand corner. By comparing the two and seeing that they match with each other very well, we can conclude that the region of the motionally averaging regime should be extended to the first branch point line HI.

Looking at the numerical results in Fig. 10, we can further challenge the original boundary between the free diffusion regime and the motionally averaging regime by proposing a line through the vertices of the V-shaped contour lines. The boundary between the free diffusion regime and the localization regime also moves upward to intersect the other two boundaries. The upper plot in Fig. 11 shows the newly-adjusted boundaries imposed on the numerical simulation results. Line B'O' has the same slope as the old one, that is, $-\frac{1}{3}$. It appears to be tangent to the contour line of $T_2^* = 10$. Line G'O' is the first branch point line. Line D'O' goes through the vertices of the contour lines and has a slope of -1 . These three new boundaries intersect at point O' $(-1.257, 0.565)$.

With these newly-adjusted boundaries, contour lines of T_2^* from four analytical equations are shown in the lower four plots of Fig. 11. Compared with original boundaries, the new ones yield a much better matching between the numerical results and analytical solutions. Also, with the new boundaries, the previous problem that analytical

equation [8] reaches its limit of validity in some transitional region is avoided. Most importantly, each analytical solution is valid only in a limited region, while numerical simulation predicts relaxation time for every region in the $(\log_{10} D^*, \log_{10} \tau^*)$ domain.

APPLICATION: DETERMINATION OF D AND L_s

The numerical simulator, together with the analytical equations, can be used to determine fluid diffusivity and pore length for systems relaxing at different relaxation regimes.

Figure 12 plots $1/T_2^*$ over a range of τ^* on a log-log scale at fixed D^* . Alternatively, $1/T_2$ can be plotted over a range of τ on a log-log scale. The only difference between these two plots will be a common up-down or left-right shift ($\log_{10} t_0$) of the curves while keeping the same shape. Six solid lines are for $\log_{10} D^*$ values of $[-4 -3.5 -3 -2.5 -2 -1.5]$. As τ^* increases (at fixed D^*), nuclear magnetization first relaxes in the free diffusion regime then in the localization regime. So at smaller τ^* , straight lines with slope 2 are observed, then wiggling curves are seen at larger τ^* . Three dashed lines are for $\log_{10} D^*$ values of $[-1 -0.5 0]$. They are in the transitional region between free diffusion regime and motionally averaging regime. So, they first have a straight line part (slope 2) then gradually level off. Four dotted lines are for $\log_{10} D^*$ values of $[0.5 1 1.5 2]$. Magnetization relaxes in the motionally averaging regime and the relaxation rate is independent of τ^* . Therefore, horizontal lines are observed.

In practice, T_2 measurements at different echo spacings with applied constant tool gradient are often performed. Thus, Fig. 12 can be prepared with the $(1/T_2, \tau)$ data pairs. (Note: only consider the relaxation rate due to diffusion mechanism.) Depending on the shape of the resultant curve, fluid diffusivity, D , and system length, L_s , can be determined.

If a straight line with slope 2 is observed, then magnetization decays in the free diffusion regime. From analytical equation [7], the dimensionless relaxation rate is:

$$\frac{1}{T_2^*} = \frac{1}{3} D^* \tau^{*2} \quad [11a]$$

Thus, fluid diffusivity can be determined from T_2 , half echo spacing τ , and tool gradient G as :

$$D = \frac{3}{T_2 (\gamma \tau G)^2} \quad [11b]$$

If a horizontal line is observed, then magnetization decays in the motionally averaging regime as described by Eq. [10]. Since relaxation rate is independent of τ^* in this regime, the second term of the exponent can be ignored. Thus,

$$\frac{1}{T_2^*} = \frac{1}{120D^*} \quad [12a]$$

Therefore, the system length can be determined from D , tool gradient G , and T_2 .

$$L_s = \left(\frac{120D}{\gamma^2 G^2 T_2} \right)^{\frac{1}{4}} \quad [12b]$$

If magnetization decays in the transitional region, then numerical simulator is needed. Just as analytical equations [11a] and [12a] where T_2^* is explicitly expressed as a function of D^* and τ^* , numerical simulator implicitly expresses T_2^* as a function of the same two parameters. Thus in principle, D and L_s can be determined.

CONCLUSIONS

Numerical method for simulating CPMG with diffusion was systematically developed. The parameter space that defines the relaxation process can be reduced to only two dimensionless groups: D^* and τ^* , instead of as ratios of three length scales. Three relaxation regimes: free diffusion, localization, and motionally averaging regimes are identified in the $(\log_{10} D^*, \log_{10} \tau^*)$ domain. The hypothesis that the dimensionless normalized magnetization ϕ^* relaxes as a single exponential with a constant dimensionless relaxation time T_2^* is justified for most regions of the parameter space.

The analytical and numerical solutions are compared from the contour plots of T_2^* . The location of the boundaries between different relaxation regimes defined in the analytical analysis is challenged by the numerical results. After adjustment of boundaries, numerical simulation results and analytical solutions match each other for every relaxation regime except for near the boundaries.

The parameters, fluid diffusivity and pore length, can be estimated from analytical solutions in the free diffusion and in the motionally averaging regime, respectively. Estimation of the parameters near the boundaries of the regimes may require numerical simulation.

ACKNOWLEDGEMENT

The authors wish to thank for the financial support from Department of Energy, Energy and Environmental Systems Institute of Rice University, and an industrial consortium of Arco, Baker Atlas, Chevron, ExxonMobil, GRI, Halliburton/NUMAR, Marathon, Norsk Hydro, Phillips, Saga, Schlumberger, and Shell. ...

REFERENCE

- Kleinberg, R. L. and Horsfield, M. A., 1990, *Journal of Magnetic Resonance*, Vol. 88, No. 1, p. 9-19.
- Le Doussal, P. and Sen, P. N., 1992, *Physical Review B*, Vol. 46, p. 3465
- Brown, R. J. S. and Fantazzini, P., 1993, *Physical Review B*, Vol. 47, No. 22, p. 14823-14834.
- Bergman, D. J. and Dunn, K. J., 1995, *Physical Review E*, Vol. 51, p. 3401.
- Bergman, D. J., Dunn, K. J., and LaTorraca, G. A., 1995, *Bulletin of the American Physical Society*, Vol. 40, No. 1, p. 695.
- Axelrod and Sen, 1998 (need to find out!)
- Hürlimann, M. D., 1998, *Journal of Magnetic Resonance*, Vol. 131, p. 232.
- Sen, P. N., André, A., and Axelrod, S., 1999, *Journal of Chemical Physics*, Vol. 11, No. 14, p. 6548-6555.
- Zhang, G. Q., Hirasaki, G. J. and House, W. V. paper ???, Society of Professional Well Log Analysts 41st Annual Logging Symposium, Dallas, TX, June 4-7, 2000.
- Torrey, H. C., 1956, *Physical Review*, Vol. 104, p. 563.
- deSwiet, T. M. and Sen, P. N., 1994, *Journal of Chemical Physics*, Vol. 100, p. 5597.
- Helmer, K. G., Hürlimann, M. D., de Swiet, T. M., Sen, P. N., and Sotak, C. H., 1995, *Journal of Magnetic Resonance A*, Vol. 115, p. 257.
- Hürlimann, M. D., Helmer, K. G., de Swiet, T. M., Sen, P. N., and Sotak, C. H., 1995, *Journal of Magnetic Resonance A*, Vol. 113, p. 260.
- Hahn, E. L., 1950, *Physics Review*, Vol. 80, p. 580.
- Stoller, S. D., Happer, W., and Dyson, F. J., 1991, *Physical Review A*, Vol. 44, p. 7459

Table 1. The boundary between different relaxation regimes.

L domain	D^* , τ^* domain
$L_D = L_S$	$\log_{10} \tau^* = -\log_{10} D^*$
$L_D = L_g$	$\log_{10} \tau^* = -\frac{1}{3} \log_{10} D^*$
$L_g = L_S$	$0 = \log_{10} D^*$

Table 2. Summary of the partition of the $(\log_{10} D^*, \log_{10} \tau^*)$ domain into regions of three relaxation regimes.

Smallest L	Regime	Region	Equation
L_D	free diffusion	BCDO	7 & 8
L_g	localization	ABOG	9
L_S	motionally averaging	GODEF	10

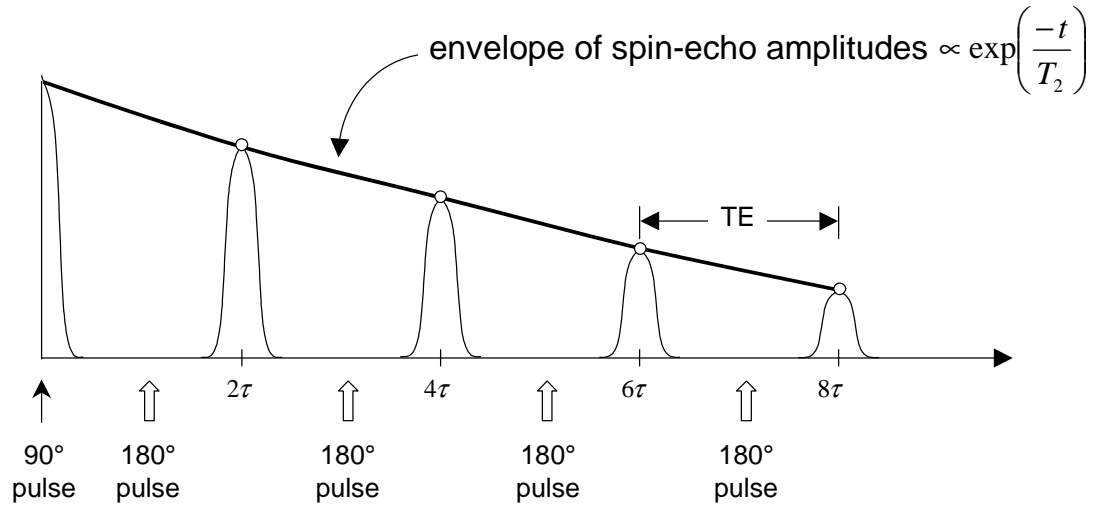


FIG. 1. CPMG pulse sequence. It begins with a 90° pulse followed by a series of 180° pulses. The first two pulses are separated by a time period τ , whereas the remaining pulses are spaced 2τ apart. Echoes occur halfway between 180° pulses at $2\tau, 4\tau \dots$, where 2τ equals TE, the echo spacing. Spin echo amplitudes decay with the time constant T_2 .

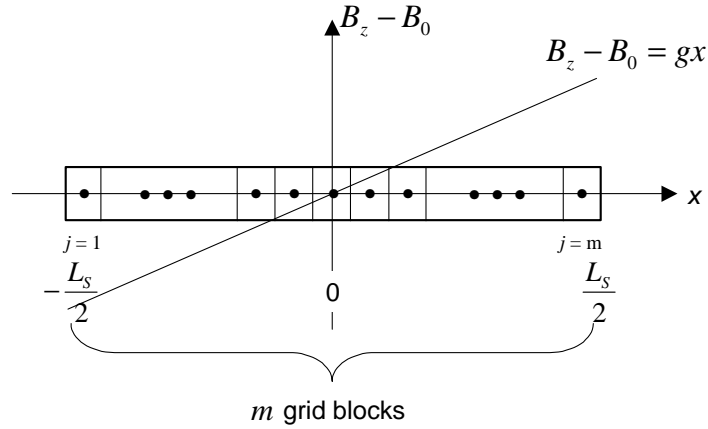


FIG. 2. System of study. A 1-D pore divided into m grid blocks with total length L_s . It is in the presence of a magnetic field with constant gradient g .

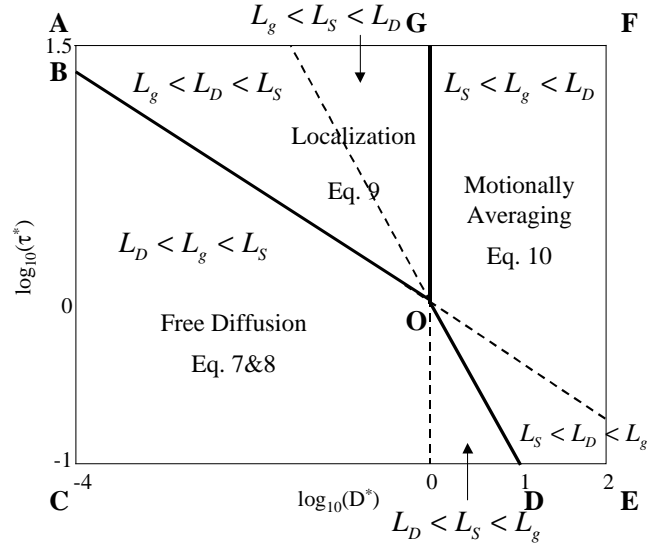


FIG. 3. Partition of the $(\log_{10} D^*, \log_{10} \tau^*)$ domain into three relaxation regimes: region BCDO for the free diffusion regime (L_D the smallest, Eqs. [7] & [8]), region ABOG for the localization regime (L_g the smallest, Eq. [9]), and region GODEF for the motionally averaging regime (L_S the smallest, Eq. [10]).

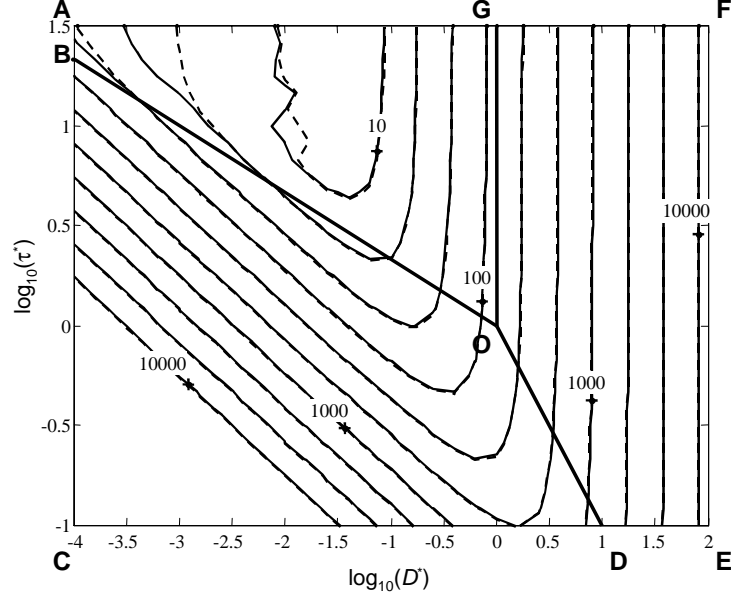


FIG. 4. Comparison of contour lines of T_2^* at $t^* = 80$, solid curves, and at $t^* = 800$, dashed curves.

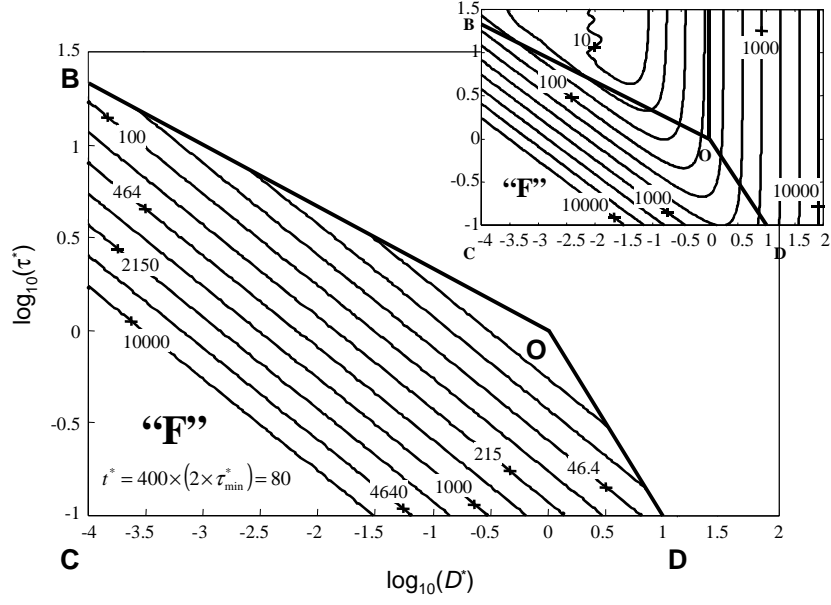


FIG. 5. Contour lines of T_2^* from Eq. [7] plotted for region BCDO. Straight lines with slope $-\frac{1}{2}$ are observed. Numerical results are shown for comparison at the upper right hand corner.

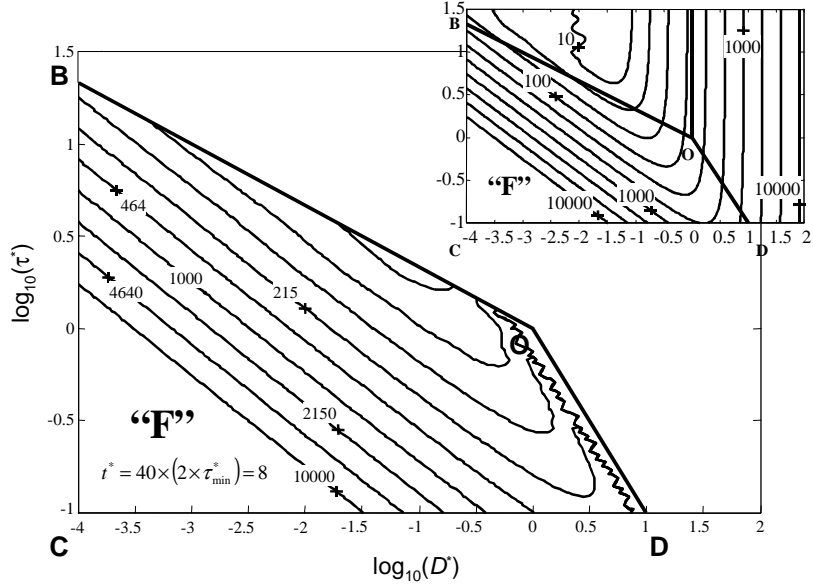


FIG. 6. Contour lines of T_2^* from Eq. [8] plotted for region BCDO. Straight contour lines with slope around $-\frac{1}{2}$ are observed for smaller D^* . Contour lines begin to curve up at larger D^* . Numerical results are shown for comparison at the upper right hand corner.

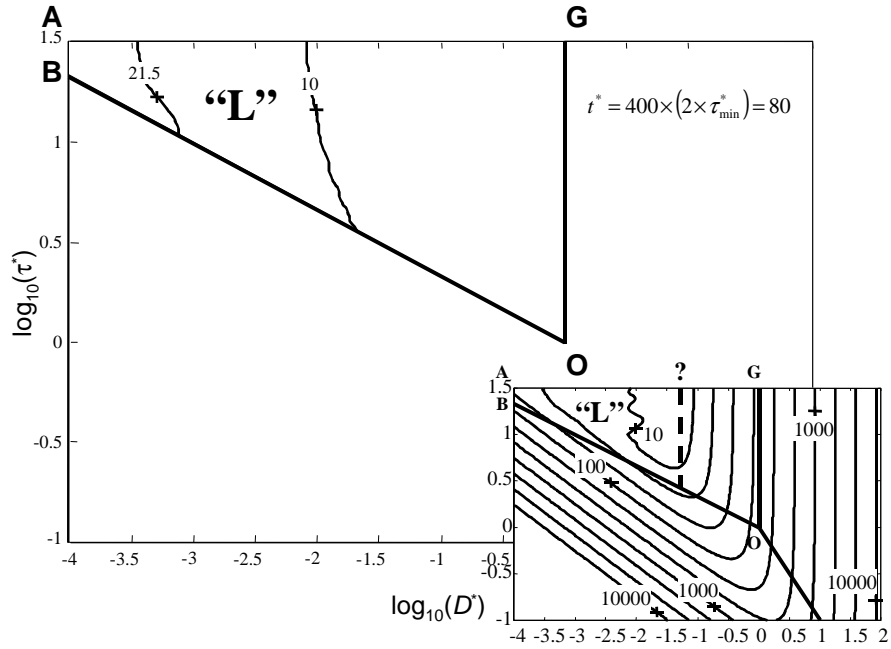


FIG. 7. Contour lines of T_2^* from Eq. [9] plotted for region ABOG. Numerical results are shown for comparison at the lower right hand corner.

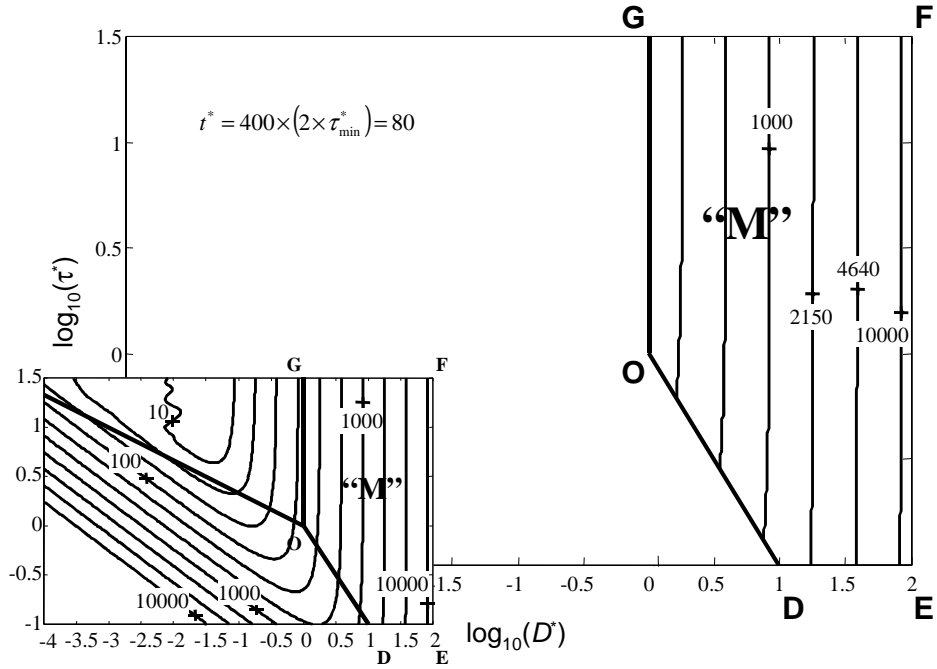


FIG. 8. Contour lines of T_2^* from Eq. [10] plotted for region GODEF. Vertical lines with slight curvature at the bottom are observed. Numerical results are shown for comparison at the lower left hand corner.

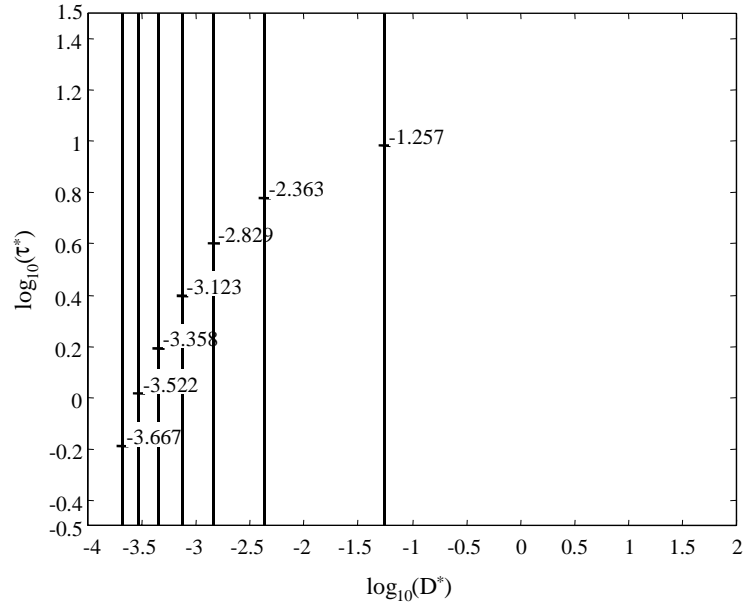


FIG. 9. Vertical branch point lines on the $(\log_{10} D^*, \log_{10} \tau^*)$ domain. The first branch point line at $\log_{10} D^* = -1.257$ coincides to our proposed dividing line between the motionally averaging regime and the localization regime.

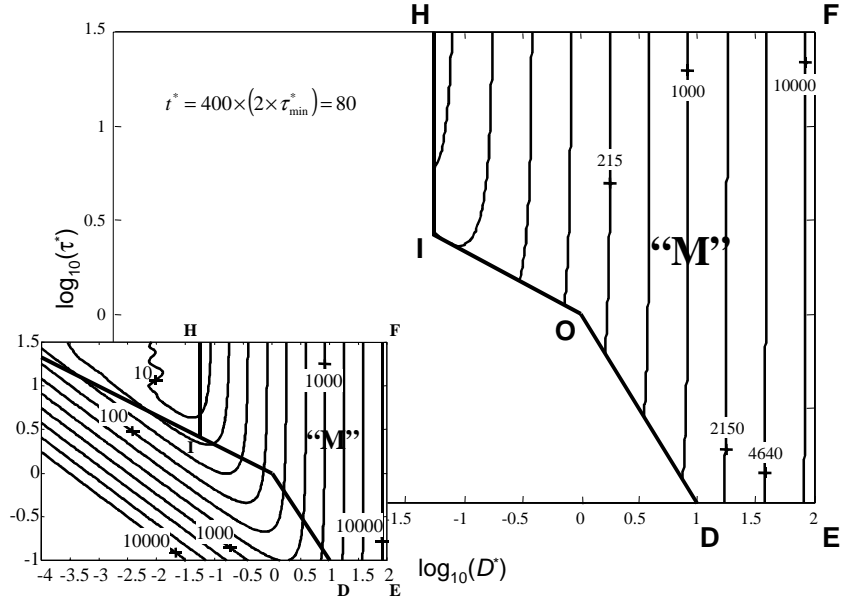


FIG. 10. Contour lines of T_2^* from Eq. [10] with boundary between the localization regime and the motionally averaging regime moved to the first branch point line HI. Numerical results are shown for comparison at the lower left hand corner.

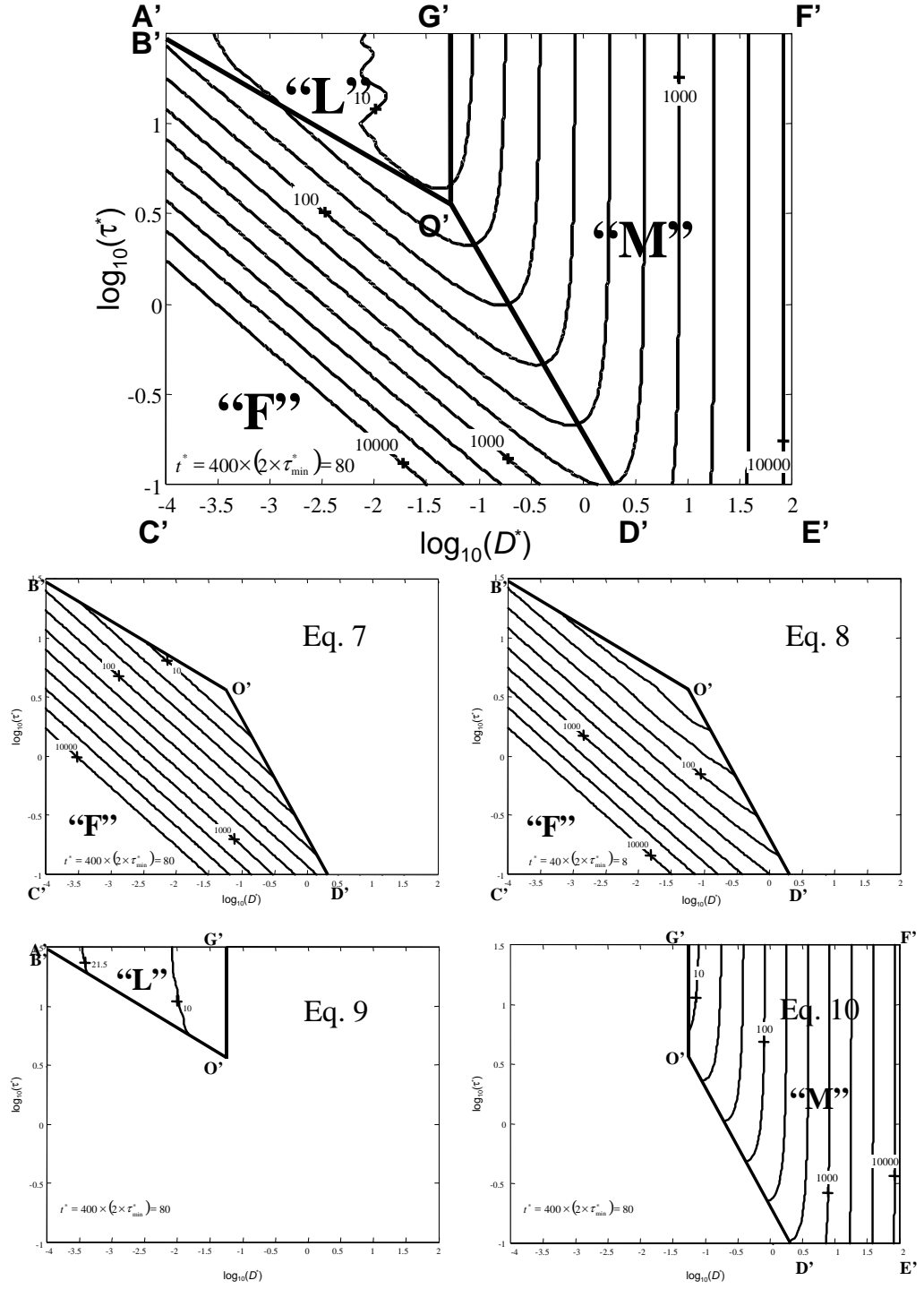


FIG. 11. Comparison of numerical simulation results with analytical solutions with newly-adjusted boundaries.

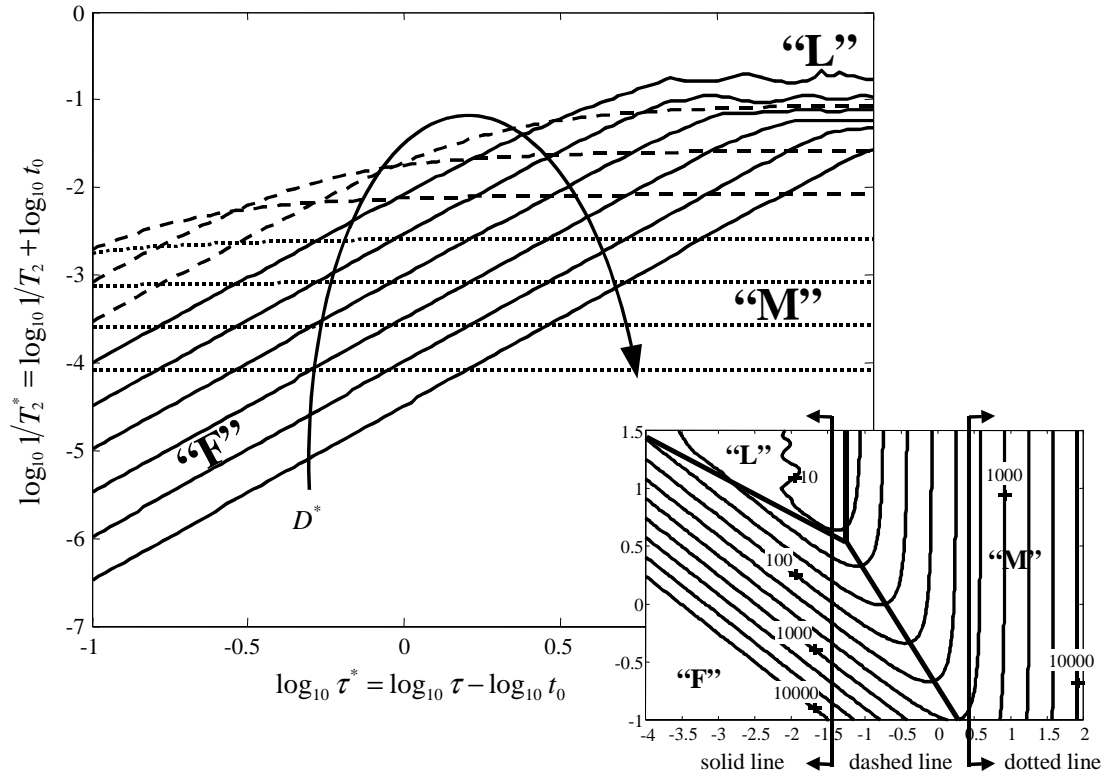


FIG. 12. Relaxation rate vs. half echo spacing on a log-log plot. Straight lines with slope 2 are observed for free diffusion regime and horizontal lines for motionally averaging regime.

Laboratory Technique for CPMG Gradient Measurements

Mark Flaum and George J. Hirasaki

Introduction

In NMR well logging, nearly all NMR-based measurements consist of CPMG determination of T_2 distributions. The CPMG results can be used to calculate or predict a number of properties of the formation, including porosity and permeability [1]. It has also been shown that these T_2 results are valid in the presence of strong static magnetic field gradients when the echo spacing is adequately short [2]. To facilitate tool design and to take advantage of the added sensitivity to diffusion presented by field gradients, logging tools are designed with static field gradients.

In laboratory spectrometers, field homogeneity is more easily achieved, so static gradients are in general not present. In order for a laboratory to contribute to the development of down-hole techniques to take further advantage of the fixed gradient, it is necessary to create an equivalent to the fixed gradient field to carry out experiments. One laboratory NMR spectrometers that operates in the low field is the Resonance Instruments (RI) MARAN spectrometer. The MARAN field gradient is supplied by an electromagnetic coil that provides a gradient field when powered. To mimic a static field gradient, the MARAN gradient coil must perform what is termed a pseudo-static gradient measurement. In that measurement, the gradient coil is powered for the duration of the echo train, so that all acquisition and radio-frequency pulses take place in a constant gradient.

This paper will review a number of steps that should be taken to improve the quality of fixed-gradient measurements in the laboratory. Some of the issues addressed here will be specific to the MARAN-Ultra spectrometer, others apply to gradient CPMG measurements in general. A number of results published by Hürlimann in [3] are reproduced here using the MARAN. The experiments in [3] were carried out in the fringe field of a high-field NMR spectrometer. Experiments here will be carried out with a pseudo-static field gradient.

Maintaining Temperature Stability

With any electromagnet-based gradient system, the operation of the gradient coils produces a great deal of heat, which must be eliminated to avoid heating the magnet up and changing the Larmor frequency. RI provides a cooling system to perform this function, but the cooling process faces limitations that must be taken into account when planning an experiment. The probe discussed here is the 40mm model, and the gradient amplifier was supplied by RI.

RI provided information about the allowable duty cycles for the gradient coils. This duty cycle limits the amount of time the gradient can be used for without risking overheating the gradient coil. Duty cycle is calculated by dividing the pulsing time (number of echoes multiplied by echo spacing) by the sum of the pulsing time and the wait time. These limits can be quite restrictive; for example the 51mm gradient coil functioning at 25 G/cm has a duty cycle of only 0.11. The fuse provided for the gradient amplifier may not be adequate to allow some pulse sequences within the duty cycle of the

gradient coil. There is a temperature cut off on the surface of the gradient coils which will terminate the pulse sequence and cut off current to the gradient coil if temperatures rise too high (above approximately 80°).

Even an experiment within the restrictions of the duty cycle may encounter problems with temperature control. Heat removal through the coolant stream may not be adequate for some pulse sequences. If the temperature of the sequence drifts over time, the Larmor frequency of the probe is likely to drift. Furthermore, the diffusivity of the sample might also increase, leading to results that are very difficult to interpret. It is possible to monitor temperature of the system by checking for changes in the frequency offset (O1, determined on the MARAN through the script AUTOO1) at the end of every measurement. For a one-second echo train at a duty cycle of 0.09 and a gradient strength of 16.8 G/cm, the offset reached an equilibrium within 3 hours of pulsing. For higher gradient strengths, the equilibrium requires more time. Figure 1 shows the frequency offset as a function of pulsing time for three different gradient strengths, all with a duty cycle of 0.09 and one-second echo collection time. Note that the equilibration times depend upon the duty cycle of the pulse sequence and the heat removal supplied. Figure 1 indicates it will be necessary to perform extra experiments to bring the spectrometer to equilibrium before gradient CPMG data can be collected.

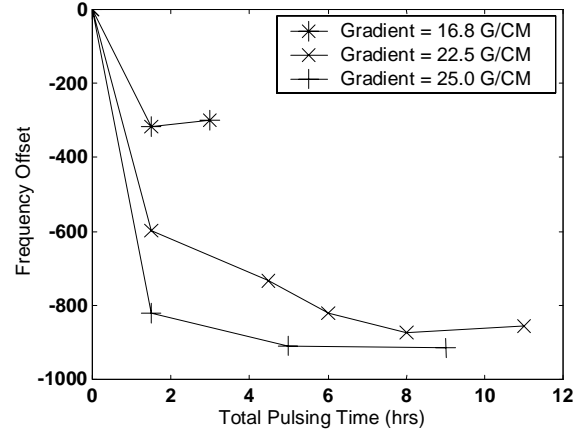


Figure 1: Frequency drift as a function of total pulsing time. The echo train is 1 second long, and the duty cycle is 0.09.

Optimizing Echo Shapes in the Gradient CPMG

In a homogeneous field, only a single coherence pathway contributes to the echo [3]. In a field gradient, on the other hand, multiple pathways contribute to the echo [2]. It is possible to calculate the contribution of any given pathway, but the computation required to solve for all the coherence pathways of a complete sequence is not feasible [4]. In practice, it is possible to assume that echoes beyond the third have converged to what is referred to as the asymptotic echo [5], meaning the echo shape

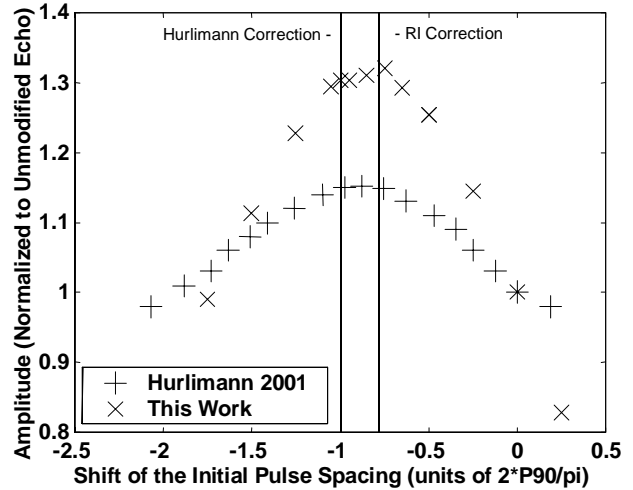


Figure 2. Pulse Spacing Shift

reaches a constant after only a few echoes.

It has been proposed that there is an optimal echo shape, achievable by reducing the initial pulse spacing (between the initial $\pi/2$ pulse and the first π pulse) of the CPMG from the usual value equal to the Carr-Purcell time (τ_{cp}). Hürlimann [3] reports an increase in signal-to-noise of 15% when the τ_{cp} is reduced by a time equal to the ninety degree pulse length (P90) divided by $\pi/2$, i.e. $P90/(\pi/2)$. Furthermore, the symmetry of the echo is greatly increased through this procedure.

A number of gradient CPMG measurements were carried out with a sample of pure water in a pseudo-static gradient using the MARAN spectrometer. The results are shown in Figures 2 and 3. Figure 2 shows an optimization of the shift of the initial pulse spacing compared to data from Hürlimann. The X axis represents the shifted timings of the initial pulse spacing, so that the recommended value takes place at -1. The Y axis is the average magnitude (over 3rd through 50th echoes), normalized to the average echo magnitude with no modification to the initial pulse spacing. In both cases curve reaches a gradual maximum not far from the predicted value. The results from our laboratory show a distinctly higher peak, indicating the difference between our modified and unmodified results is greater than that observed by Hürlimann. We suspect instrumental and sampling differences would account for this difference of shape. It should be noted that the pulse sequence included with the MARAN spectrometer has a modified first pulse spacing which corresponds to $P90/2$, which is very close to Hürlimann's recommended value of $P90/(\pi/2)$.

Figure 3 shows the effect of modifying the first pulse spacing on subsequent

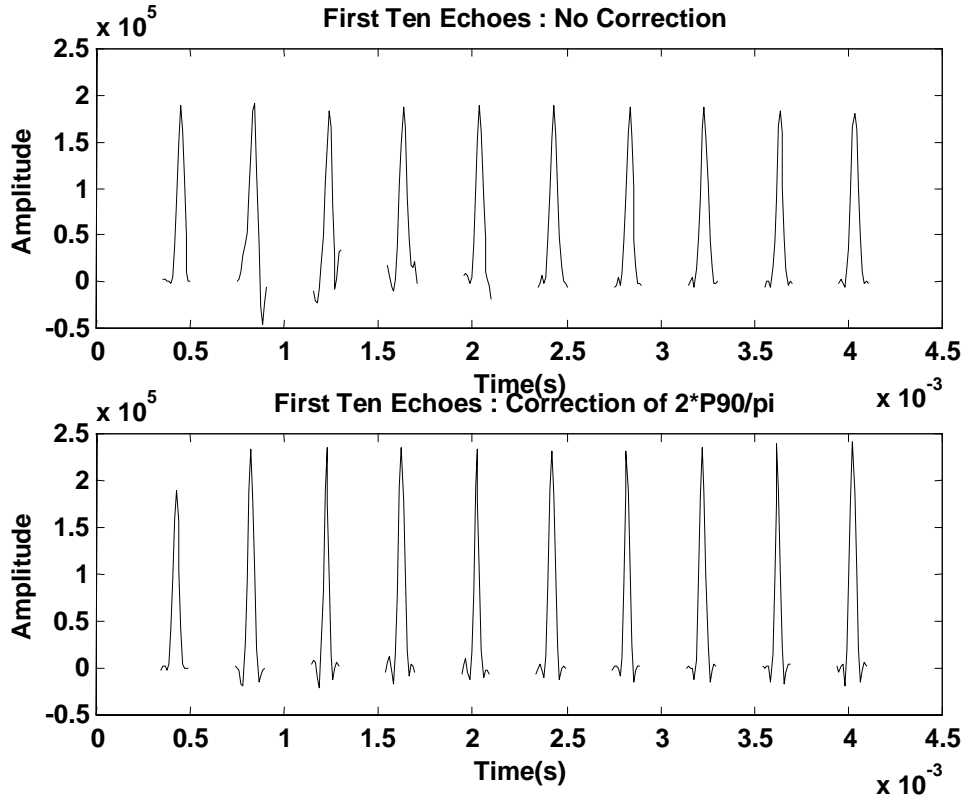


Figure 3: First ten echoes. The upper subplot shows these echoes without the optimization, the lower figure with the optimal correction predicted in [4].

echoes. A very similar figure appears in [3]. The echoes have improved in amplitude and symmetry. Note that the 20% increase in amplitude only occurs on echoes after the first, and that the first echo is not affected by the modified timing.

Sampling Technique

In any gradient CPMG measurement, the echo is significantly narrower than in a gradient-free measurement. The sampling technique chosen thus becomes significantly more important.

The first factor that must be ensured is that the sampling window is well centered on the peak of the echo. The built-in single point sampling technique does not ensure the single point is sampled from the center of the echo. In fact, the timing for a sixteen point-per-echo measurement requires an offset to place the echo in the center of the window. Figure 4 plots the echoes from two measurements against the sample points across the echo. The first measurement includes no offset to the pulse sequence, while the second includes a small offset equal to the dwell time to better center the echo. The results in Figure 4 are for water at a gradient strength of 16.8 G/cm, with 16 points separated by a dwell time of 10 μ s and an echo spacing of 0.4 ms. With most sampling methods, it is valuable to ensure the entire echo has been sampled, or at least as much of the echo as possible.

There are several ways to sample the echo. The simplest is to simply choose the center point, and to ensure this point is indeed the peak of the echo. This technique has the advantage of not risking the inclusion

of noise from outside the echo itself, but it does not take advantage of the entire area of the echo to increase the signal to noise ratio.

The second technique of choice would be to integrate across the entire echo, or to simply sum all of the sampled points. This method takes full advantage of the amplitude of the echo, but also includes parts of the sampling window that include little or no signal. The end result is that a great deal more signal is sampled, but the noise has increased as well.

Perhaps the optimal technique for sampling the echoes is the

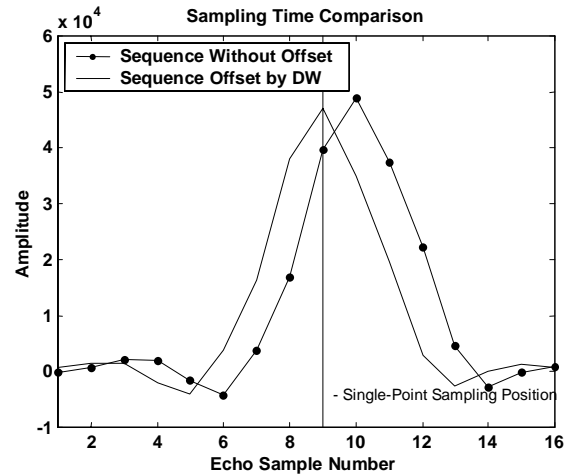


Figure 4: Centering of the Sampling Window

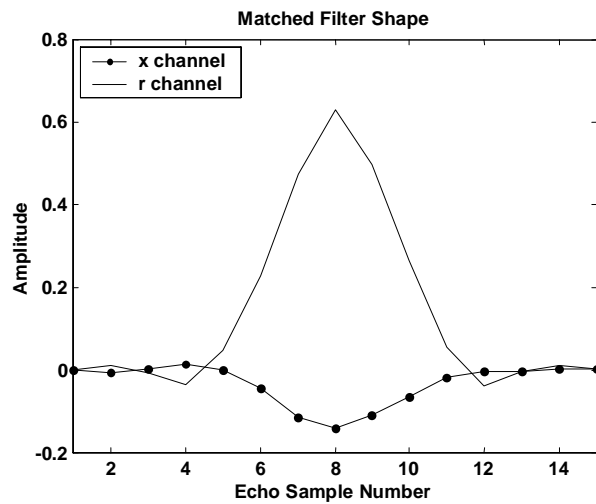


Figure 5: Matched Filter Data

matched filter. For this technique, the asymptotic or average echo is determined, and then each echo is summed using the shape of the asymptotic echo as a weighted sum. Therefore the peak of the echo gets the greatest weight, while regions with little or no amplitude contribute little to the sum. This is the technique used in [3]. In this study, the matched filter was prepared as an average over the first 60 echoes, excluding the first few to ensure asymptotic shape has been achieved. The matched filter data is plotted in Figure 5.

Signal-to-noise ratios for these techniques obtained from a water sample at 16.8 G/cm and 500 repetitions are summarized in Table 1.

Sampling Technique	S/N Ratio
Single Point	270
Echo Sum	172
Matched Filter	345

Summary

Performing a gradient CPMG measurement in the laboratory is an important part of supporting oilfield NMR logging tools as well as investigating new NMR methods. These measurements may face complications in the laboratory, but those issues can be overcome to provide useful information. Three aspects of the measurement are addressed here, and solutions are presented. The data quality of a gradient CPMG can be enhanced and ensured following these guidelines for maintaining and monitoring temperature control, optimizing echo shape, and echo sampling.

Table 1: Signal-to-noise ratio from different sampling techniques. S/N is calculated as the maximum signal divided by the standard deviation of the noise.

Acknowledgments

The authors would like to acknowledge the assistance of Martin Hürlimann, Charles Flaum, John Gardner, and Bob Freedman for their advice and assistance with these results.

References

- [1]: C. Straley, D. Rossini, H. Vinegar, P. Tutunjian, C. Morriss, "Core Analysis by Low Field NMR", *Log Analyst*, 38 2 (1997)
- [2]: G. Goelman, M. Prammer, "The CPMG Pulse Sequence in Strong Magnetic Field Gradients with Applications to Oil-Well Logging", *Journal of Magnetic Resonance A*, 113, 11-18 (1995)
- [3]: M. Hürlimann, "Optimizing of timing in the Carr-Purcell-Meiboom-Gill sequence", *Magnetic Resonance Imaging*, 19, 375-378 (2001)
- [4]: M. Hürlimann, "Diffusion and Relaxation Effects in General Stray Field NMR Experiments", *Journal of Magnetic Resonance*, 148, 367-378 (2000)
- [5]: M. Hürlimann, D. Griffin, "Spin Dynamics of Carr-Purcell-Meiboom-Gill-like Sequences in a Grossly Inhomogeneous B₀ and B₁ Fields and Application to NMR Well Logging", *Journal of Magnetic Resonance*, 143, 120-135 (1999)

Extending PFG Restricted Diffusion Measurements

Mark Flaum and George J. Hirasaki

Introduction

The most common technique for examining diffusion through NMR is the pulsed field gradient sequence (PFG) [1]. The PFG measures the distance spins diffuse over a controlled time. This contains information about the structure of a porous network when the space the spins have to diffuse in is smaller than the total distance they would freely move in the given time, giving rise to restricted diffusion. The comparison of measured diffusivity of a particle diffusing through a porous system to the free diffusion of the bulk fluid gives information about the length scale of the pore space.

As a technique for probing pore structure, the PFG has an advantage over relaxation-based methods as it is also sensitive to pore throat size, instead of merely the pore bodies. Throat size relates more reliably to permeability in carbonates, where the pore bodies and pore throats may not be correlated. Furthermore, the measurement need not be restricted to a single pore. In fact, as the diffusion time is increased, the diffusivity attenuation approaches a limit related directly to the tortuosity. The tortuosity provides a much stronger relationship to the permeability than T_2 distributions in carbonates[2].

The major limitation of the PFG method is that diffusing spins are also subject to relaxation, meaning it is not possible to use diffusion times longer than the relaxation time [3]. This problem is of particular weight with vuggy carbonates, which represent a system where T_2 -based permeability indicators tend to fail. The problem here is that relevant length scales are well beyond the maximum diffusion length of water in a pore space. In order to approach this problem, we carried out a series of measurements with pentane as the saturating fluid in place of water. Pentane has a longer bulk relaxation time, and a higher diffusivity than water and less surface relaxation. The results of these experiments are presented here.

Background

Hahn Echo

Diffusion has a major effect on NMR magnetization in the presence of a magnetic field gradient. When the magnetic field is not uniform, any spin (polarized proton) that diffuses from one field strength to another will lose coherence with the non-relaxed spins, and will therefore not be measured when the total number of coherent spins is counted in a spin echo. The standard spin echo method, called the Hahn echo, nutates the spins into the transverse plane and allow them to precess for a controlled amount of time τ , then flip the spins 180°. The spins still in the transverse plane then precess back to their original position, where they achieve coherence called a 'spin echo', as shown in Figure 1. The mechanism of gradient induced relaxation is different from the standard transverse relaxation (called T_2 , and based on the spin-spin interactions in the system), but both

affect the attenuation of the magnetization. The echo attenuation in a gradient is as follows [4]:

$$\ln\left(\frac{M}{M_o}\right) = \frac{-t}{T_2} + 2\gamma^2 DG^2 \frac{\tau^3}{3} \quad (1)$$

Where M is magnetization as a function of time (M_0 at time 0), τ is the time between the radio-frequency pulses, T_2 is the characteristic transverse relaxation time, γ is the gyro-magnetic ratio, D is the self-diffusion constant of the relaxing fluid, and G is the strength of the field gradient. From this expression, the diffusion constant of the fluid can often be evaluated directly from the magnetization decay of a Hahn echo in a known constant field gradient.

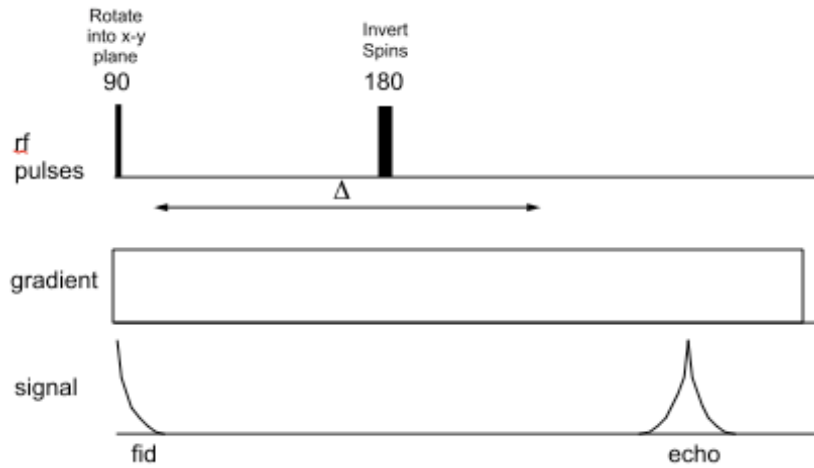


Figure 1: The Hahn Echo in a Magnetic Field Gradient

The Pulsed Field Gradient

For many systems, however, it is not possible to determine diffusion using a simple spin echo. For example, if the diffusivity or gradient strength is too high, the magnetization decay may be too fast to measure accurately, and techniques usually used to extend this decay tend to mute the effect of the diffusion term. Also, if the diffusion constant is very small, or if the diffusion term in the exponential is small compared to the T_2 , decay due to diffusion in the field gradient may not be significant compared to relaxation. In porous systems the presence of surface relaxation (due to paramagnetic materials in the matrix or similar mechanisms) tends to reduce T_2 leaving diffusion-based relaxation negligible.

When a Hahn echo is no longer adequate for examining relaxation due to diffusion, it is possible to employ a different pulse sequence, called the Pulsed Field Gradient spin echo (PFG). A diagram of this pulse sequence is shown in Figure 2. In this sequence, instead of requiring that the entire experiment take place in a field gradient, the gradient is applied in two short pulses after each of the radio-frequency pulses. These gradient pulses are of time width δ and separation Δ , which referred to as the diffusion time, as it determines the amount of time the spins are allowed to diffuse.

The first pulse spreads the spins into positions where they are allowed to diffuse, effectively encoding the phase of the spins. Then, after the 180° pulse inverts the precession, second gradient pulse returns the spins to their original orientation for measurement, with the difference that now those spins that have diffused are not decoded to their original position are no longer measured in the spin echo. In this way, it is possible to separate the diffusion relaxation from transverse relaxation by comparing the magnetization with gradient pulses present to the magnetization with the gradient strength reduced to zero according to the equation [4]:

$$\ln\left(\frac{M(G)}{M(G=0)}\right) = -\gamma D G^2 \delta^2 \left(\Delta - \frac{\delta}{3}\right) \quad (2)$$

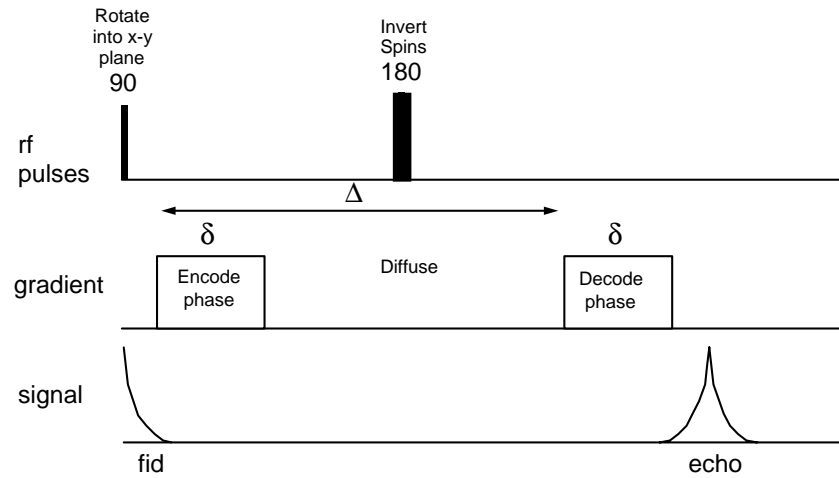


Figure 2: Pulsed Field Gradient Sequence.

The Pulsed Field Gradient – Stimulated Echo

In some systems, however, it is still often not possible to measure D with these methods due to the short transverse relaxation time. It may be possible to take advantage of the fact the longitudinal relaxation time is often larger than the transverse relaxation time. For rock systems, the longitudinal to transverse relaxation time ratio is on average 1.5:1. To take advantage of this, the spins can be moved from the axis where they decay according to the transverse relaxation time to the axis where they experience longitudinal relaxation. This pulse sequence, called the Pulsed Field Gradient – Stimulated Echo (PFG-SE), is shown in Figure 3. This sequence again begins with a 90° rf pulse, followed by a gradient pulse of width δ to encode the phase of the spins. In this case, however, another 90° rf pulse follows, moving the spins into the plane of longitudinal relaxation, where they are effectively stored without allowing transverse decay. Immediately preceding the end of this diffusion time, another 90° pulse moves the spins back to the transverse plane so as to allow the development of an echo similar to the spin

echo above, called the stimulated echo. Finally, a second gradient pulse undoes the spreading, again decoding the phase excluding those that have diffused out of coherence. This sequence is characterized by two times, τ_1 and τ_2 , corresponding to the start of the second and third 90° rf pulses. It should also be noted that δ is very small compared to the other times in the pulse sequence, so Δ , the time between gradient pulses, is generally assumed to be equal to the time the spins diffuse. The equation for the magnetization of this system is [1]:

$$\ln\left(\frac{M}{M_0}\right) = \left(\frac{(\tau_2 - \tau_1)}{T_1} - 2\frac{\tau_1}{T_2} - \gamma D G^2 \delta^2 \left(\Delta - \frac{\delta}{3}\right)\right) \quad (3)$$

This result can be compared to the result obtained with the gradients equal to zero, giving once again equation (2), except that the noise levels for systems with T_1 greater than T_2 will be reduced.

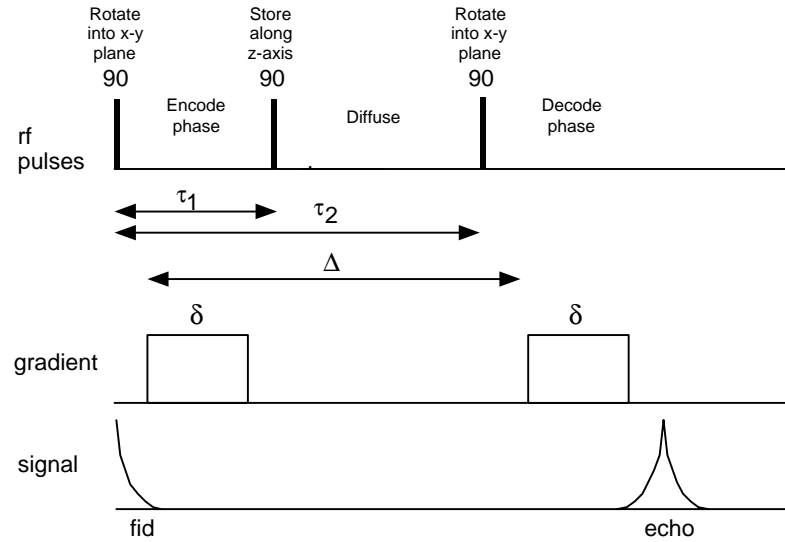


Figure 3: Pulsed Field Gradient – Stimulated Echo Sequence.

NMR Diffusion in Porous Media

In a porous system, there are two distinct categories of diffusion. The first is free diffusion, where the diffusing particle has no contact with the surrounding surfaces and thus behaves as any diffusing particle in a bulk fluid. The second is restricted diffusion, where the diffusing particle is obstructed and thus reflected by the walls of the pore body. There are two parameters that determine which regime a measurement describes. The first is diffusion length:

$$l_d = \sqrt{6D_0\Delta} \quad (4)$$

Where D_0 is the bulk self-diffusion constant. The second is the characteristic spatial wavenumber associated with the gradient pulse [2]:

$$k = \gamma \delta G \quad (5)$$

The importance of the equation (4) is evident, for when the diffusion length approaches the pore radius, diffusion starts to deviate from free diffusion.

The parameter k from equation (5) is already evident in equations (1), (2), and (3), and is also fundamental in describing the magnetization in a restricted diffusion system [2]:

$$\ln\left(\frac{M(k, \Delta)}{M(0, \Delta)}\right) = \sum_{n=1}^{\infty} \frac{(ik \cdot [r(0) - r(\Delta)])^{2n}}{2n} \quad (6)$$

Where $[r(0) - r(\Delta)]$ expresses the distance traveled by a spin during time Δ . If k is small, this expression can be truncated to the first term, and the magnetization is only dependant on k^2 , but when k becomes large, higher order terms can be significant. In practice, this equation is almost always truncated to determine D , in which case the equation can be rewritten as follows [2]:

$$\ln\left(\frac{M(k, \Delta)}{M(0, \Delta)}\right) = -k^2 \Delta D(\Delta) \quad (7)$$

Time Dependant Diffusion: Short Diffusion Times

As indicated in equation (7), the diffusivity that is determined from this expression is dependent on the diffusion time Δ of the experiment. If the measured $D(\Delta)$ differs from the bulk value, restricted diffusion is indicated. A plot of measured diffusivity against diffusion length will diverge from linearity when this occurs. At very short diffusion times Δ , the observed diffusion should behave exactly as the bulk-fluid diffusion, as no spins diffuse long enough to encounter the restrictions. As the diffusion time increases, however, more and more spins will reach the wall and face restriction, so the observed diffusivity will begin to diverge from the bulk-fluid diffusivity. At the onset of this divergence, there will be a thin layer of spins close to the surface of the pore that diffuse under restriction, while those in the body of the pore diffuse as bulk fluid. The deviation of the observed diffusion constant from the actual self-diffusion constant will therefore be proportional to the surface to volume ratio. The equation to describe this deviation is [6]:

$$\frac{D(\Delta)}{D_0} = 1 - \frac{4\sqrt{D_0\Delta}}{3\sqrt{\pi}} \frac{S}{V} + O(D_0\Delta) \quad (8)$$

It should be noted that if the diffusion times are extremely short, the equation collapses down to free diffusion. It has also been speculated that the development over time should give some indication of the varying length scales throughout a system. The logic is this: if there are multiple distinct length scales in a sample, the development of each length scale should cause an inflection in a curve of D_{obs} vs. Δ representing each changing length scale. The smallest range of pore sizes would cause a deviation at short times, and later, when the diffusion in a larger pore range begins to encounter restriction, there will be a new effect visible in the deviation. As long as the pore size distribution

consists of several distinct ranges, separated perhaps by one or two orders of magnitude, it should be possible to distinguish the contributions from the different pore-size ranges. This would be a particularly useful measurement in carbonate rocks, where the vugs will have a large effect on relaxation measurements but are often excluded from predictions of permeability as they are assumed to have little contribution to flow [9].

Time Dependent Diffusion: Long Diffusion Times

Returning once more to equation (7), the other regime of interest is when Δ is large. If Δ is large enough to describe diffusion through the entire system, $D(\Delta)$ should approach a constant value representing the macroscopic diffusion coefficient. The macroscopic diffusion constant is essentially a measure of the path length through the pore network, as the proton is essentially allowed to diffuse long enough to navigate through all connected pores. As a measure of connectivity, the macroscopic diffusion constant (called D_{eff}) can be used to determine the formation factor F , a fundamental parameter related to tortuosity. Formation factor is actually the ratio of conductivity through a porous system compared to conductivity through free fluid. The relationship between D_{eff} and F is as follows [2]:

$$D_{\text{eff}} = \frac{D_0}{\tau_{\text{tort}}} = \frac{D_0}{F\phi} \quad (9)$$

Where ϕ is the porosity of the system and τ_{tort} is the tortuosity. D_{eff} is often referred to as the tortuosity limit or asymptote.

Limits of the Pulsed Field Gradient

In order to evaluate the limit D_{eff} , there must remain enough sensitivity to distinguish diffusion-based decay from T_2 decay. The key parameter is again the l_d . If the signal disappears before l_d has approached the length scale of the entire network, it will not be possible to evaluate the D_{eff} . The l_d can be increased by modifying either the relaxation time or the diffusivity of the saturating fluid. In this experiment, pentane was the saturating fluid chosen, as pentane relaxes slower than water and has a higher diffusivity as well, Table 1. Experiments have been carried out with success in the literature with polarized xenon gas as the saturating fluid [7]. Polarized xenon is not available for these experiments, but we expect that supercritical ethane will prove practical. Ying Zhang (this report) measured the values of ethane in Table 1.

Compound	Relaxation Time (s)	Diffusivity (cm ² /s)
Water	2.8	2.0×10^{-5}
Pentane	4.5	2.0×10^{-4}
Ethane (28° C, 575 psi)	20	1.1×10^{-3}
Xenon [10]	1 (O ₂ doped)	5.7×10^{-2}

Table 1: Relaxation Times and Diffusivities

Experimental

Dry rocks were wrapped in heat-shrinkable teflon tubing, saturated with water or air-saturated pentane and capped. T_2 distributions for the two samples chosen are in Figures 4 and 5. Figure 4 shows the samples water-saturated, Figure 5 saturated with pentane. In the latter case, the distribution have shifted to longer times, suggesting more time available to diffuse before the sample has relaxed. According to these distributions, the signal for either sample saturated with pentane can be expected to relax completely though T_2 relaxation alone after 4 to 5 seconds.

These rocks were measured using the PFG-SE sequence. The gradient pulses were 3 G/cm, with a duration δ of 750 microseconds. The gradient diffusion time Δ was varied until the signal was no longer detectable. Equipment limitations provided a minimum Δ of 20 milliseconds.

Results

The results of the PFG-SE measurements are shown in Figures 6 and 7. Figure 6 shows the results of the magnetization decay. The magnetization decay shown is due to diffusion only, as the relaxation contribution is canceled out by comparison with the results of same measurement with gradient strength of zero. For unrestricted diffusion, this plot would show a straight line, but restrictions change the slope over time. The more permeable sample seems to diffuse within a single pore space throughout the measurements carried out here, as the slope of reduced magnetization against diffusion

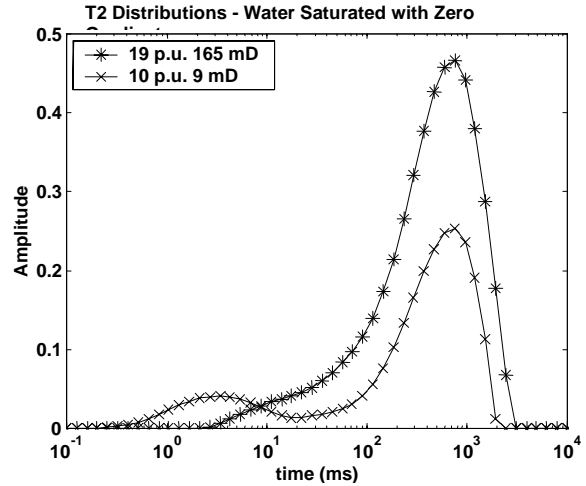


Figure 4: Water-Saturated T_2 Distribution

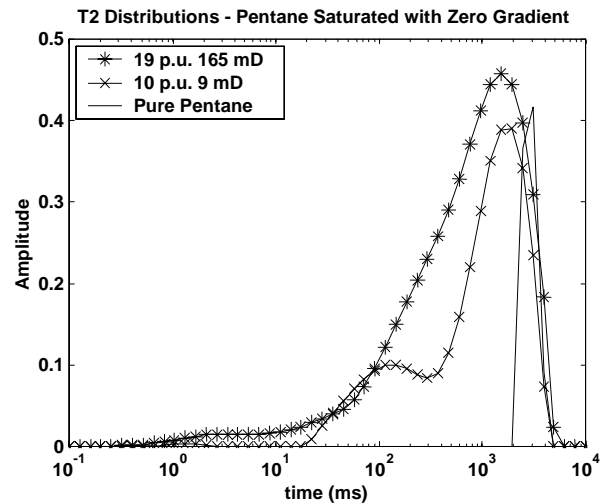


Figure 5: Pentane-Saturated T_2 Distribution

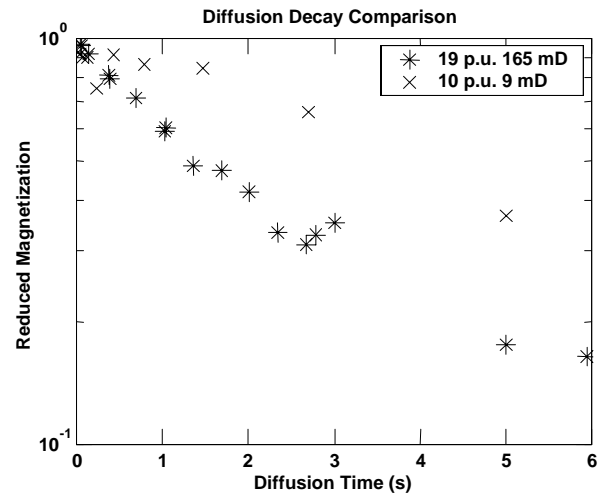


Figure 6: Diffusion decay comparison

time is largely constant. The less permeable sample shows the definite onset of restriction. In Figure 7, reduced measured diffusivity is plotted against diffusion length. The first sample had a permeability of 165 mD and a porosity of 19 p.u. The second had a permeability of 9 mD and a porosity of 10 p.u. The first curve appears to decay slowly, and does not achieve a plateau before sufficient relaxation occurs to leave no measurable signal. The second sample, on the other hand, appears to have reached a plateau. The samples presented here are both vuggy carbonates, though by visual inspection the first seems to contain significantly more vugs than the second.

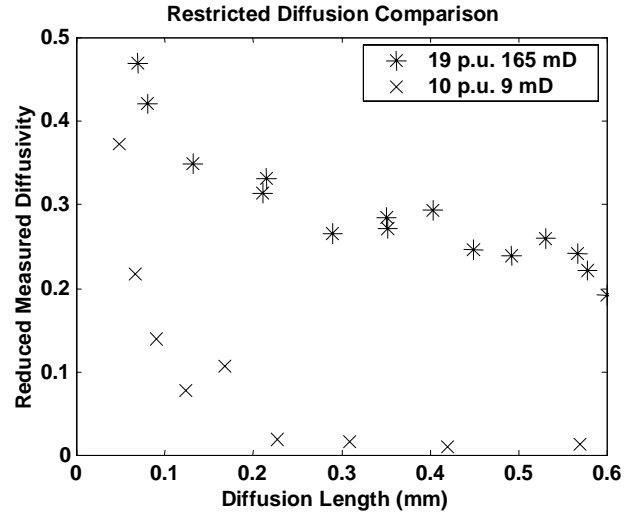


Figure 7: Restricted diffusion comparison. Both samples are Yates field carbonates saturated with pentane. Reduced diffusivity refers to measured diffusivity divided by the measured diffusivity of bulk pentane. Diffusion length is defined as $\sqrt{6D_o\Delta}$

In neither sample was it possible to estimate the surface-to-volume ratio, as the minimum diffusion times were far too long. In both rocks the magnetization had dropped below half of the relaxation-only amount at the first measurement. The 165 mD sample indicates a formation factor of 20, very similar to the value of 27.8 predicted by Archie's law [7] using a cementation exponent of 2. This value, calculated from the last 6 data points, seems low, as the cementation exponent for a vuggy carbonate is expected to be higher than the sandstone value of 2. This formation factor corresponds to a tortuosity of 4. This sample does not appear to have reached the correct tortuosity limit. A formation factor of 670 can be calculated for the 9 mD sample using equation (9). Archie's Law [7] would predict a value between 100 and 1000, depending on the value of the cement exponent. No measurements were made to estimate the cementation exponent. This formation factor corresponds to a tortuosity of 67. This is much larger than that of the high permeability rock.

Irwan Hidajat and Kishore Mohanty (this report) have compiled a study of pore morphology and rock characterization data that will be used with these experimental techniques to further examine the extended PFG methods. A set of six carbonate rock samples with complicated pore structures were selected and characterized using mercury porosimetry, thin section analysis, and basic core petrophysical measurements. These cores will then be analyzed in a CT scanner, and finally measured with PFG NMR. The objective of these measurements will be to develop a complete understanding of the pore morphology of the samples, as well as to develop new techniques for evaluating and predicting vuggy carbonate properties with NMR.

Conclusions

PFG measurements on two samples with distinctly different permeabilities gave very different results, suggesting that it may be quite possible to evaluate permeability from these diffusion measurements. The results also indicated that a pentane-saturated system may be adequate for some samples, but it will be necessary to extend the maximum achievable diffusion length for to obtain a complete result for others. The possibility of extending these diffusion lengths with supercritical ethane seems promising.

References

- [1]: J. E. Tanner, "Use of Stimulated Echo in NMR Diffusion Studies", *Journal of Chemical Physics*, **52** 5 (1970)
- [2]: P. Mitra, P. Sen, "Effects of microgeometry and surface relaxation on NMR pulsed-field-gradient experiments: Simple pore geometries", *Physical Review B*, **45**, 1 (1992)
- [3]: L. Latour, R. L. Kleinberg, P.P. Mitra. C.H. Sotak "Pre-Size Distributions and Tortuosity in Heterogeneous Porous Media", *Journal of Magnetic Resonance A*, **112**, 83-91 (1995)
- [4]: E. Fukushima, S.B.W. Roeder, Experimental Pulse NMR, Perseus Books, Mass. 1981
- [5]: M. Lipsicas, J.R. Banavar, J. Willemsen, "Surface Relaxation and Pore Sizes in Rocks: A Nuclear Magnetic Resonance Analysis", *Applied Physics Letters* , **48**, 1554 (1986)
- [6]: L. Schwartz, P. Sen, P Mitra, "Simulations of Pulsed Field Gradient Spin Echo Measurements in Porous Media", *Magnetic Resonance Imaging* **12**, 2(1994)
- [7]: R. Mair, M. Hurlimann, P. Sen, L. Schwarz, S. Patz, R Walsworth, "Tortuosity measurement and the effects of finite pulse widths on xenon gas diffusion NMR studies of porous media", *Magnetic Resonance Imaging* **19**, 345-351(1994)
- [8]: D. Ellis, Well Logging for Earth Scientists, Elsevier Science Publishing Co., New York (1987)
- [9]: D. Chang, H. Vinegar , C. Morriss ,C. Straley, "Effective Porosity, Producible Fluid and Permeability in Carbonates from NMR Logging", *Log Analyst*, **38** 2 (1997)
- [10]: R. Mair, D. Cory, S. Peled, C-H. Tseng, S. Patz, R Walsworth, "Pulsed-Field-Gradient Measurements of Time Dependant Gas Diffusion", *Journal of Magnetic Resonance* **135**, 478-486(1998)

STUDY OF VUGGY CARBONATE CORES USING X-RAY CT

I. Hidajat and K. K. Mohanty

Department of Chemical Engineering

University of Houston,

Abstract

Estimating petrophysical properties of carbonate rocks from NMR measurement is much less reliable than of sandstone. The difficulty arises from the fact that most carbonates exhibit three different length scales from intragranular porosity, intergranular porosity and vugular porosity. The existing permeability correlation from T_2 measurement assumes that vugs do not contribute to permeability, hence a 750 ms cut off is chosen to exclude the vug contribution. This may not always be the case, since vugs may be connected in some formation and contribute to the permeability. The objectives of this work are to identify vug connectivity by using X-ray CT scan, and to improve NMR permeability correlation. CT scanning of dry Yates core material shows that uniformity of vug distribution varies from core to core. CT scanning of core floods in one Chester Field sample shows that the vugs are non-touching. The Chang and Vinegar correlation estimates the permeability correctly from NMR T_2 response because the vugs do not contribute to permeability in this sample. In the future, similar core flood experiments will be performed in some samples from the Yates field.

Introduction

More than 50% of the world's hydrocarbon reserves is in carbonate formations. However, estimating petrophysical properties from NMR measurements in carbonate rocks have always been a bigger challenge than in sandstone formations. Broad pore size distribution in carbonates, from intragranular porosity to large vugs is the reason for the unreliable estimation of transport properties from NMR logging.

Fig. 1 shows a simplified diagram for classifying different type of pore space in carbonate rocks¹. The intragranular porosity is the porosity inside the grain (ϕ_μ). The intergranular porosity is the pore space between the grains. And the vuggy porosity is defined as the pore space within grains or crystals, or that is significantly larger than grains or crystals.² Vugs can be thought of as the absence of one or more grains in packing, or if there is a significant pore space within the grain. The more popular definition for vugs in industry is a pore space that can be easily seen because usually these pores are larger than 200 μm in size.¹

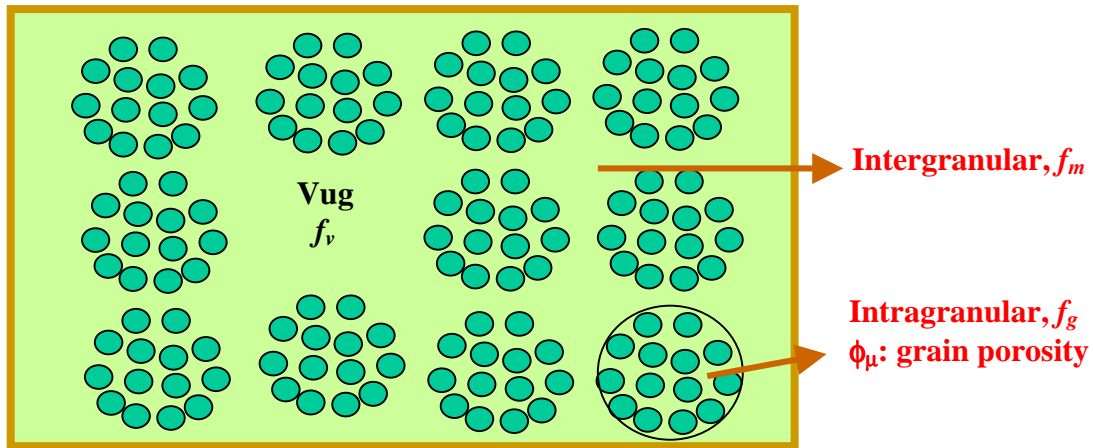


Fig. 1 Simplified Model of Carbonate Rocks

From Fig. 1, we can write:

$$f_v + f_m + f_g = 1 \quad (1)$$

where f_v is the vug volume fraction, f_m is the intergranular volume fraction and f_g is the grain volume fraction. The overall porosity (ϕ) is given as :

$$\phi = f_v + f_m + f_g \phi_\mu , \quad (2)$$

where ϕ_μ is the intrinsic porosity of the grain.

Vugs can be classified into separate vugs and touching vugs.² Separate vugs are defined as pore space that is interconnected only through the interparticle porosity. Touching vugs are pore space that forms an interconnected pore system independent of the interparticle porosity.

Chang and Vinegar et al. (1997) measured 27 carbonate core plugs and found the permeability correlation from the NMR T_2 distributions as:³

$$k = 4.75 (\phi_{\text{NMR}, 750})^4 (T_{2, 750})^2 \quad (3)$$

where k is the permeability (mD), $\phi_{\text{NMR}, 750}$ and $T_{2, 750}$ is the porosity and the logarithmic mean of T_2 distribution with $T_2 < 750$ ms. The correlation assumes that vugs have T_2 distribution larger than 750 ms and they do not contribute to the permeability. In other words, they assume that all the vugs are separate vugs. This may not be the case, in some instances vugs may be connected and contribute to the permeability.

Hicks (1990) conducted CT Scan study on carbonate rocks from Fenn Big Valley and San Andres (TX) dolomite.⁴ He studied the porosity distribution, residual saturations and miscible displacements. However, no study was conducted on the connectivity of the vugs.

The objective of this work is to study the vug connectivity and to improve the permeability correlation from NMR for vugs contribution. From CT Scan experiment, we

can investigate the connectivity and the distribution of the vugs in the rock sample. Other measurements such as: permeability, capillary pressure, Sor and thin section will also be performed. By combining the matrix structure information from the thin section and the vugs distribution from the CT Scan, we will be able to construct a representative porous media and simulate different vugs configuration. Finally, from all the information both from experiment and simulation we may identify the condition where vugs contribute to permeability.

2. CT Scan Experiments

CT scanning is done by using a Deltascan 2060HR CT scanner manufactured by Technicare Corporation. The scanner gantry has been rotated 90° from the conventional vertical position so that the scan plane is horizontal. This enables the fluid displacements to be conducted in the vertical direction. The scanner resolution is 0.25 x 0.25 x 2mm for each voxel. All experiments reported here were conducted with the scan plane horizontal. For flow experiments, a core is put into a hassler type core holder. The core holder is mounted on a table positioned below the gantry and the table is raised or lowered to place the core at the desired position. The position of the core can be reproduced to within 5 µm in the vertical direction. During a scan, the X-ray source rotates through a full circle in the scan plane around the core sample. The 720 detectors located around the scan circle detect the X-ray signal, then the host computer will process the data and perform a reconstruction. The reconstructed image is a matrix of 512 x 512 pixels, and each pixel represents the voxel size as described above. Table 1 shows the available parameters in the CT scan and the selected parameters for the entire experiments done.

Parameter	Available	Selected
Voltage (KV)	80, 100, 120	120
Current (mA)	25, 50, 75, 100	75
Scan time (sec)	2, 4, 8	8
Scan diameter (cm)	12, 25, 40 ,50	12
Slice thickness (mm)	2, 5, 20	2

Table 1. Available and Selected Parameter in CT-Scan

The first CT experiment was done on Yates samples. The samples were directly scanned without putting them into the coreholder. No flow experiment was done at this stage. The purpose was to study the sample structure and identify suitable positions for plugging 1” or 1.5” core samples.

The second CT experiment was done on a Chester Field sample and involved flooding experiments. The purpose of the experiment is to investigate the porosity distribution, preferential flow path, and oil saturation at S_{wr} and at S_{or} .

3. Yates Samples

Six Yates bare samples are scanned, and we present three of them since the other three can be categorized into these three classes. The scans were taken at 1-cm interval.

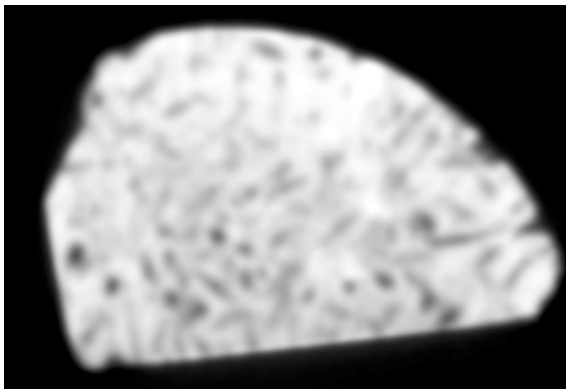
The first sample is 17C9; the sample is 6 cm in diameter and 6.8 cm in height. The sample is not cylindrical. The picture of the sample is shown in Fig. 2. Visually it is observed that the matrix is very tight and there are a lot of vugs; the vug size is about 1 mm to 3 mm. Vugs are distributed more or less uniformly throughout the sample (Fig. 3). Small diameter plugs are representative of the medium.

The second sample is 2416; the sample is 7 cm in diameter and 10.6 cm in height. The matrix also looks very tight and vugs are not uniformly distributed. Fig. 4 shows the picture of the sample. Vugs occur only in some layers, and the other layers there are almost free of vugs, as indicated in CT images (Fig. 5). Most of the vugs are small and less than 0.5 mm. A few vugs have size about 1 mm.

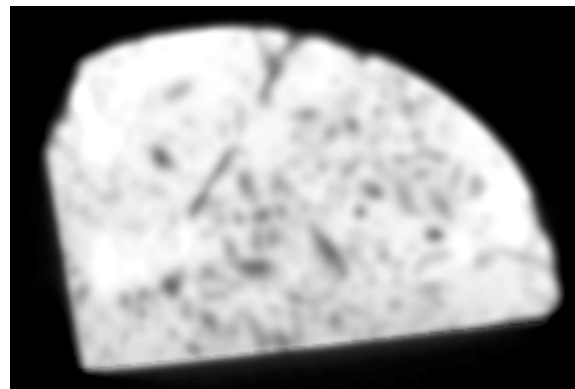
The third sample is 7626B; the sample is 8 cm in diameter and 17.9 cm in height. The matrix looks permeable, but the vugs distribution is not uniform. Fig. 6 shows the picture of this sample, which has some large vugs with size up to 5mm. The small vugs are scattered throughout the sample with size about 1mm – 2mm. The CT images are given in Fig. 7.



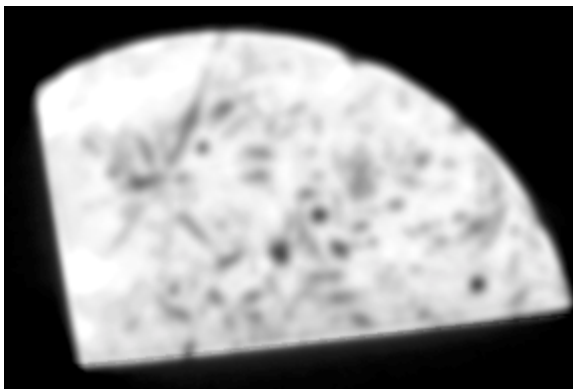
Fig. 2. Picture of sample no.17C9



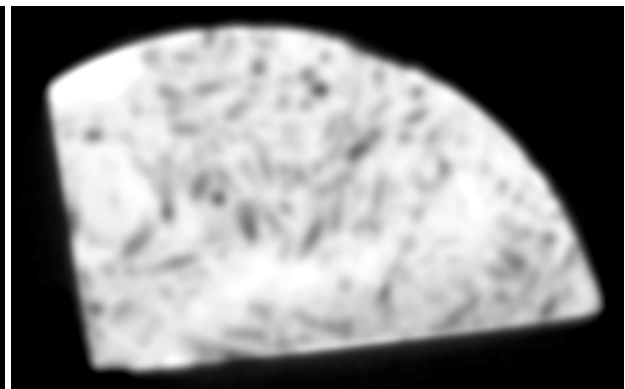
Slice 1



Slice 3



Slice 5

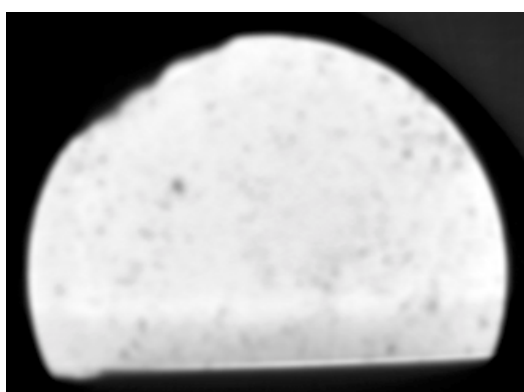


Slice 8

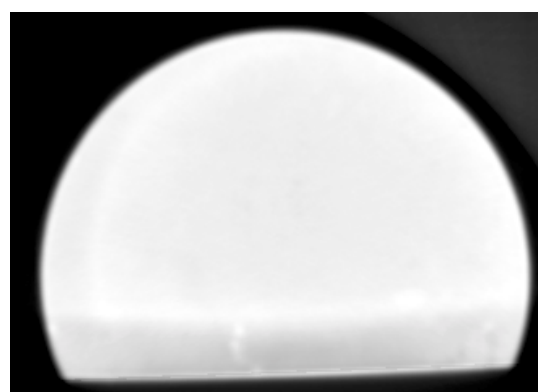
Fig. 3 CT Image for sample 17C9 at selected slices



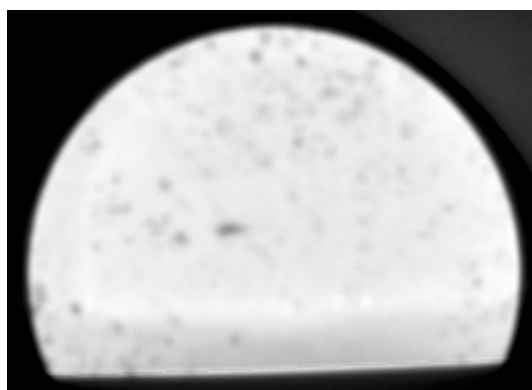
Fig. 4 Picture of sample no. 2416



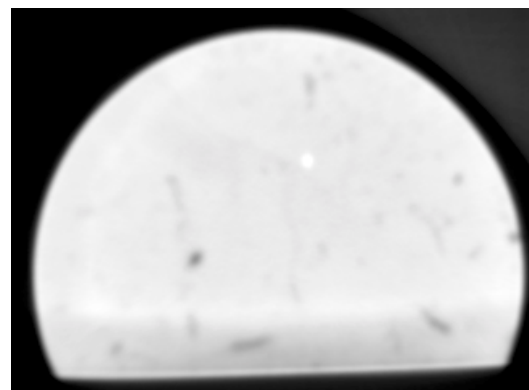
Slice 1



Slice 4



Slice 7

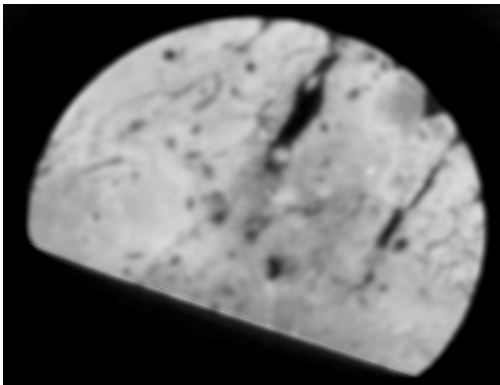


Slice 10

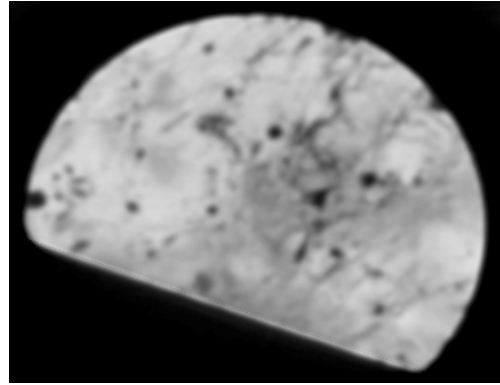
Fig. 5 CT Images for Sample 2416 at selected slices



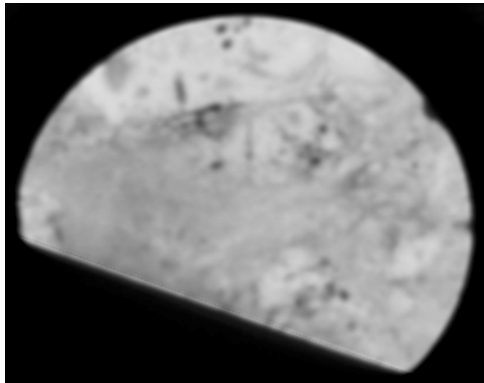
Fig. 6 Picture of sample no. 7626B



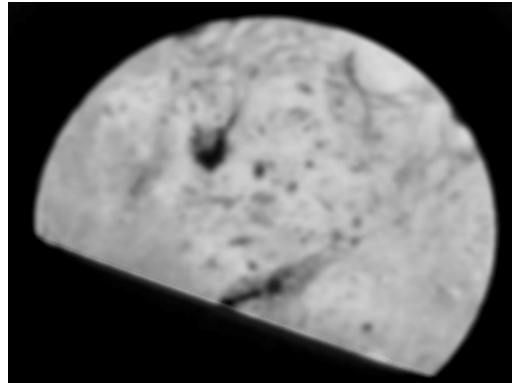
Slice 4



Slice 6



Slice 11



Slice 15

Fig. 7 CT Images for Sample 7626B at selected slices

4. Flooding Experiment on Chester Field Sample

The second experiment is performed on the Chester Field sample. This plug is a dolomite, 1" in diameter and 1.5" long. According to the data from Shell, the porosity is 17.8% and the air permeability is 115 mD. The calculated pore volume from the porosity is 3.6 ml. Vugs of about 1 – 2 mm are visible on the plug. The sample was put into a core holder and an overburden pressure about 700 psi was applied. The scans were taken at 4-mm interval. Doped brine and doped oil are used in some experiments to increase the image contrast.

The following experiments were conducted on this sample:

1. The core was scanned in vacuum condition.
2. The core was saturated with brine (1 wt% of NaCl), and scanned. By subtracting with the CT image taken in step 1, porosity distribution of the core was obtained.
3. The core was flooded with doped brine (15 wt% of NaI in brine) and scanned at different time. From this step, preferential flow path was investigated.
4. The core was flushed with brine and scanned.
5. The core was flooded with doped oil (15 wt% of Iododecane in n-decane) until S_{wr} was reached and scanned to obtain oil distribution at S_{wr} .
6. The core was flooded with brine until S_{or} was reached and scanned to obtain oil distribution at S_{or} .
7. The core was taken out from the coreholder. NMR T_2 response was measured at S_{or} condition.
8. The core was cleaned by using Dean-Stark extraction apparatus. Toluene was used as the cleaning fluid. The amount of water collected was measured.
9. The core was resaturated with brine and NMR T_2 response was measured at 100% brine condition.

The porosity distribution from the CT Scan for each slice is given in Fig. 8. The light colored area indicates high porosity region. The high porosity regions are uniformly distributed in slices 1 through 6; they shift towards the upper right area in slices 7 -10.

Each slice contains a few vugs (from one vug to about four vugs) and the vugs appear not to be touching.

Figs. 9 through 11 show the doped brine profile at 0.25, 0.5 and 1.25 injected pore volume, respectively. Note that the color represents the CT number difference between the core with doped brine and the core in vacuum condition, and it is not actual doped brine concentration. Because of the machine problem during the experiment, we were not able to take scan of the fully saturated core at 100% doped brine saturation at the same scan condition. The CT number difference reflects the concentration of doped brine in the core. At 0.25 PV injected, the brine had not reached slices 7 through 10. The doped brine flowed through high porosity area, and clearly some vugs in slice 1, 2, 3 and 6 were in this flow path. At 0.5 PV injected, the brine breakthrough had occurred. As shown in Fig. 10, there were vugs in slices 9 and 10 in this flow path. Similar to the porosity distribution, the flow path moved to the upper right past the slice 7. There were some vugs in slice 9 that had not been invaded by doped brine yet, indicating that those vugs were not in the preferential flow path and channeling occurred. At 1.25 PV injected, most of the pore space was invaded by doped brine. The vugs are indicated with very light color region. This experiment shows that although the vugs are not touching, most of them are in the preferential flow path.

Fig. 12 shows the doped oil distribution at irreducible water saturation (S_{wr}) condition. The calculated S_{wr} from the material balance is 52%. The data for slice 1 is corrupted and it is not shown. Again, the color refers to the CT number difference between the core with doped oil and the core with saturated brine. To obtain the doped oil saturation profile, scan from 100% doped oil saturated core is needed which is not available at this stage. The CT number difference, again, reflects the amount of doped oil. From the CT images in Fig. 12, the doped oil appears to be almost uniformly distributed in the high porosity area. All the vugs are occupied by the oil.

Fig. 13 shows the doped oil profile at the residual oil saturation (S_{or}) condition. The computed S_{or} from the material balance is 32%. Again, the color refers to the CT number

difference between the core with doped oil and the core with saturated brine. From the CT images in Fig. 13, the doped oil is mostly swept from the middle region of the core, and the S_{or} resides in the perimeter region. The pore volume computed from the Dean Stark extraction is 3.67 ml, which is consistent with the pore volume calculated from the porosity data from Shell.

T_2 distributions at S_{or} and 100% brine saturation are shown in Fig. 14. The solid line represents the T_2 distribution at 100% brine saturated. The peak occurs at 600 ms and the computed $T_{2logmean}$ is 381 ms. There is a significant region at T_2 greater than 750 ms, indicating the presence of vugs. The computed permeability from Eq. 3 is 99 mD, which agrees well with the air permeability. This also confirms that vugs are non-touching and do not contribute to its permeability. The dashed line in Fig. 14 shows the T_2 distribution for the doped oil. The main peak is at 500 ms and the response is bimodal because the oil is not pure n-decane. The dotted line represents the T_2 distribution for the core at S_{or} . This T_2 distribution is very similar to that for brine saturated core. The similarity in T_2 distribution greater than 750 ms indicates that the vugs are filled with brine. This is unlike the common assumption that residual oil occupies the vugs in water wet media.

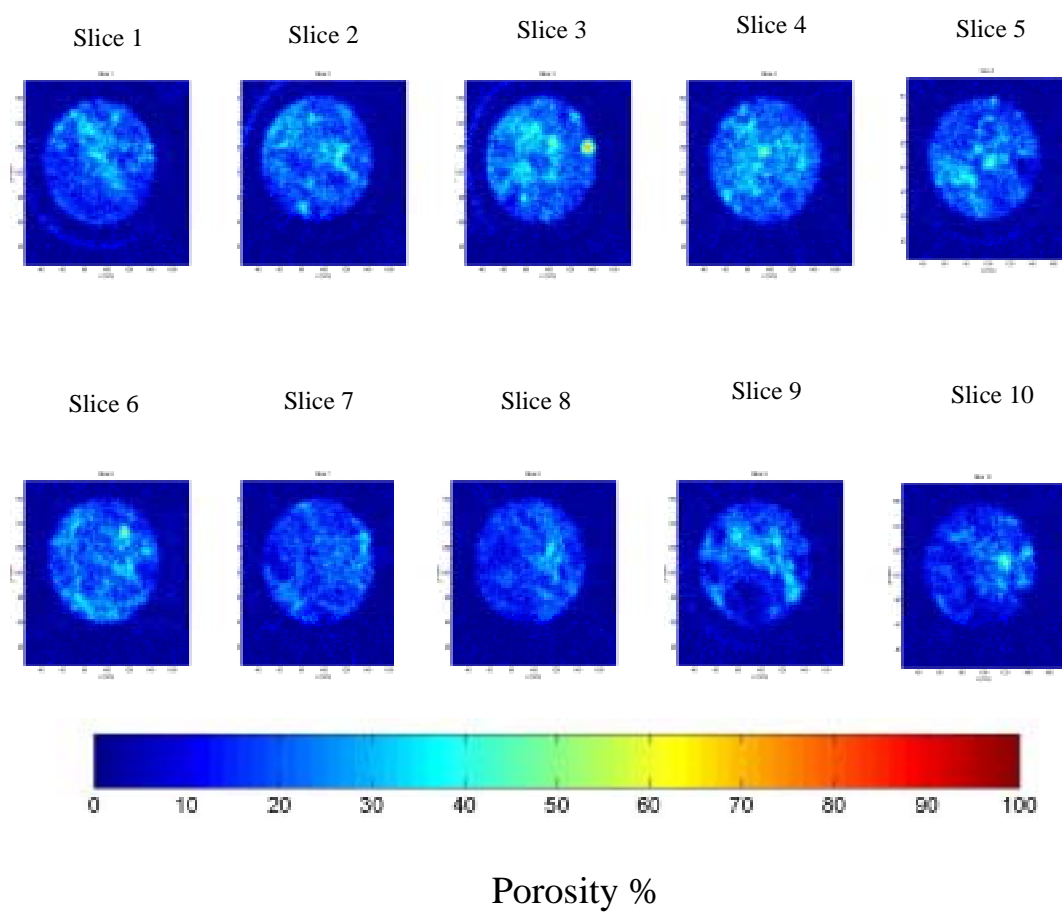


Fig. 8 Porosity Distribution from CT Scan

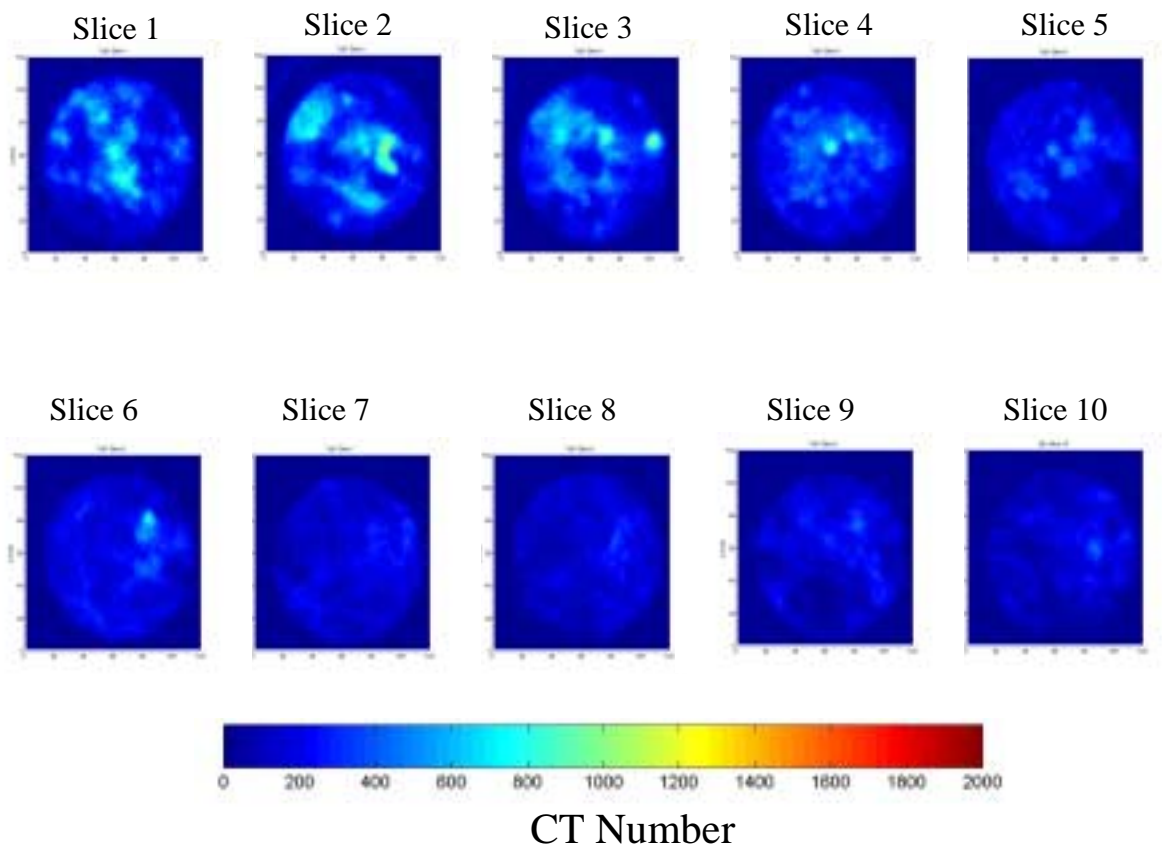


Fig. 9 Doped brine profile at 0.25 PV Injected

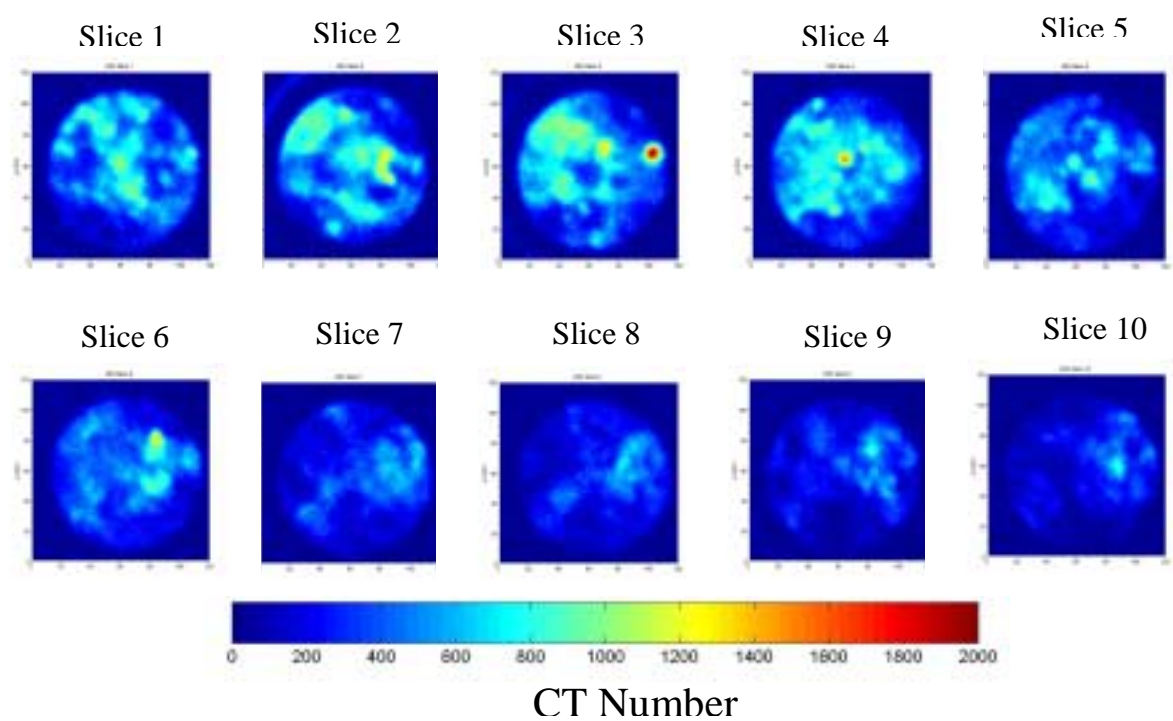


Fig. 10 Doped brine profile at 0.5 PV Injected

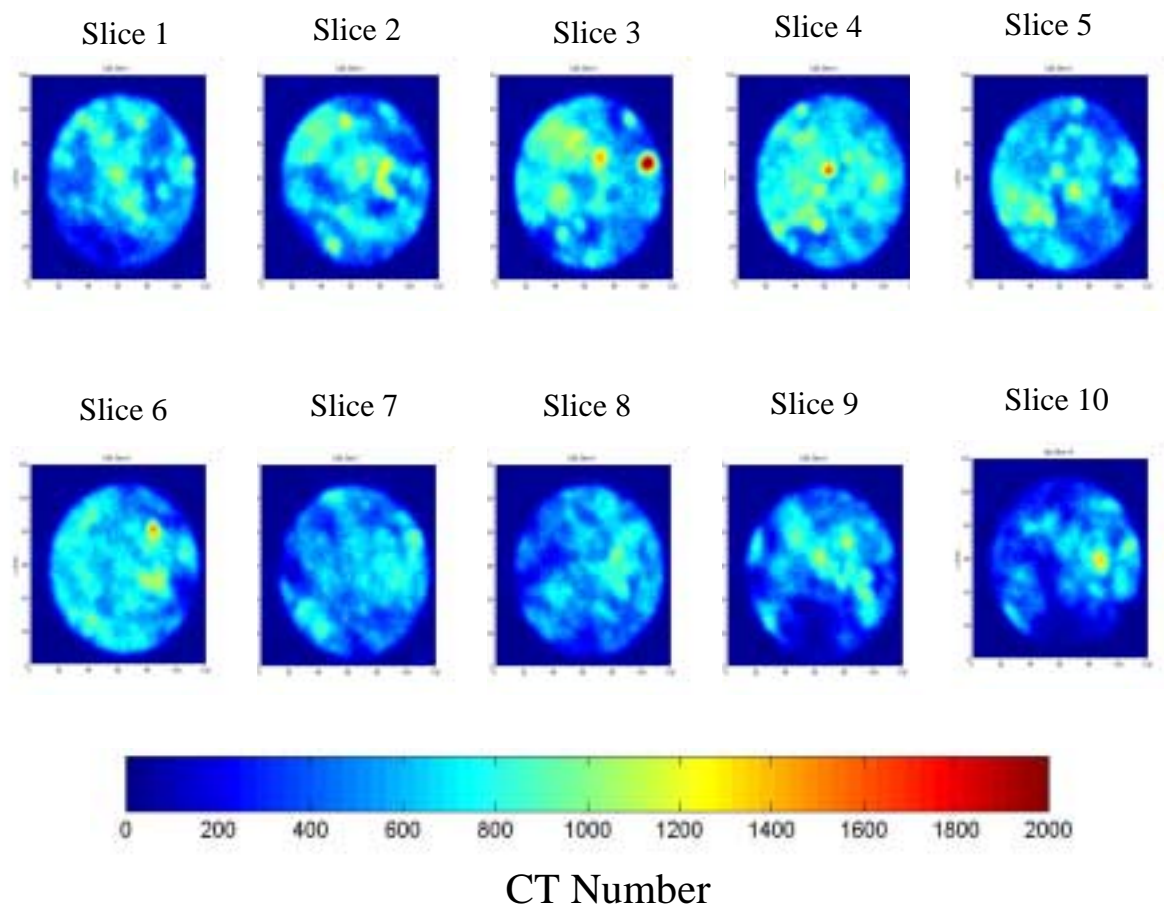


Fig. 11 Doped brine profile at 1.25 PV injected

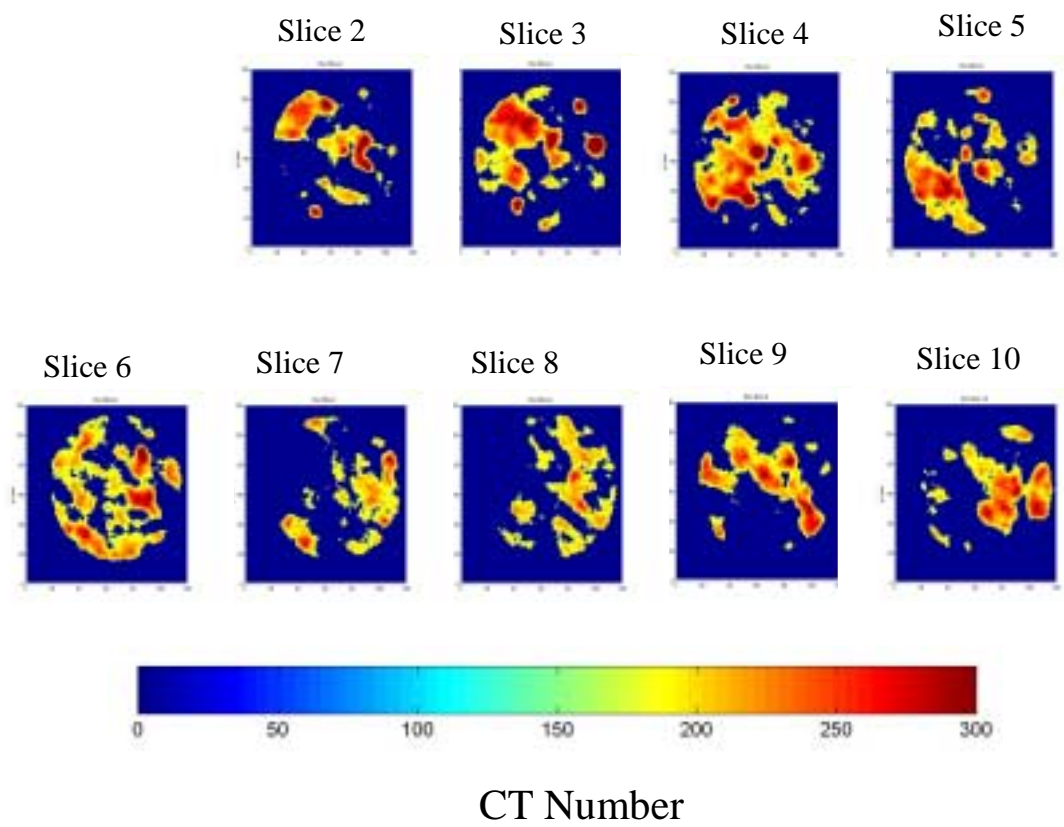


Fig. 12 Doped Oil Profile at S_{wr}

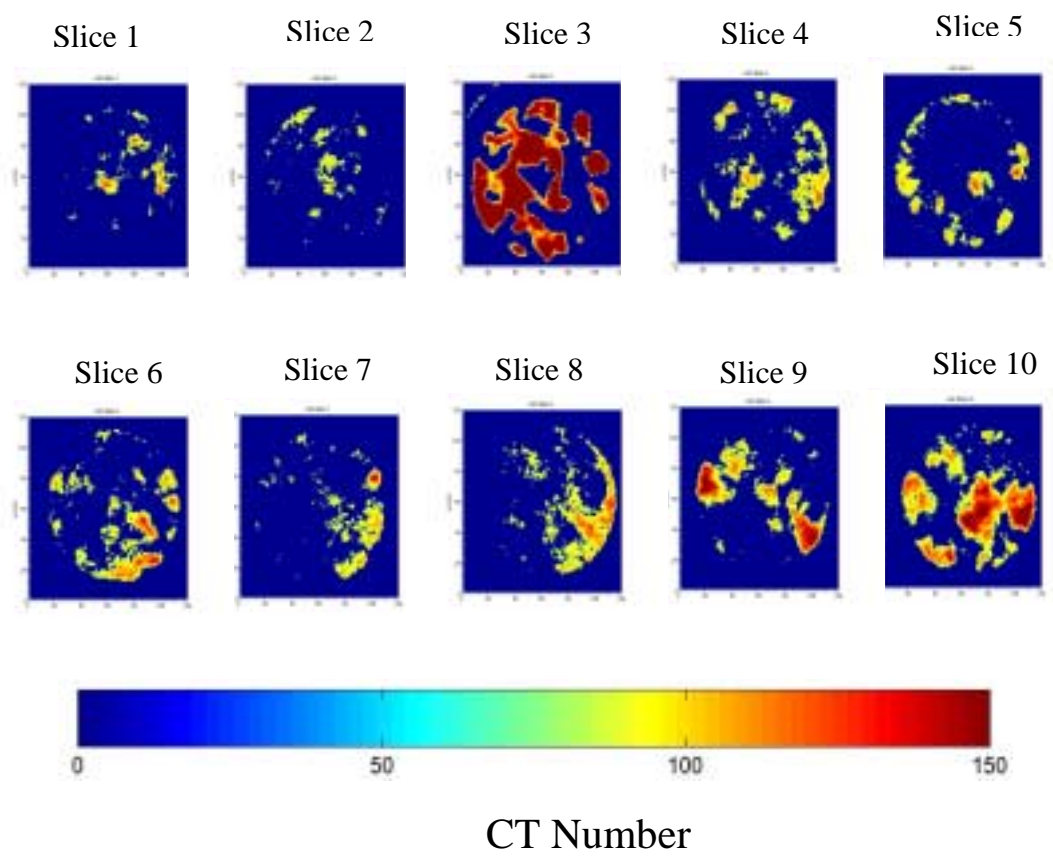


Fig. 13 Doped Oil Profile at S_{or}

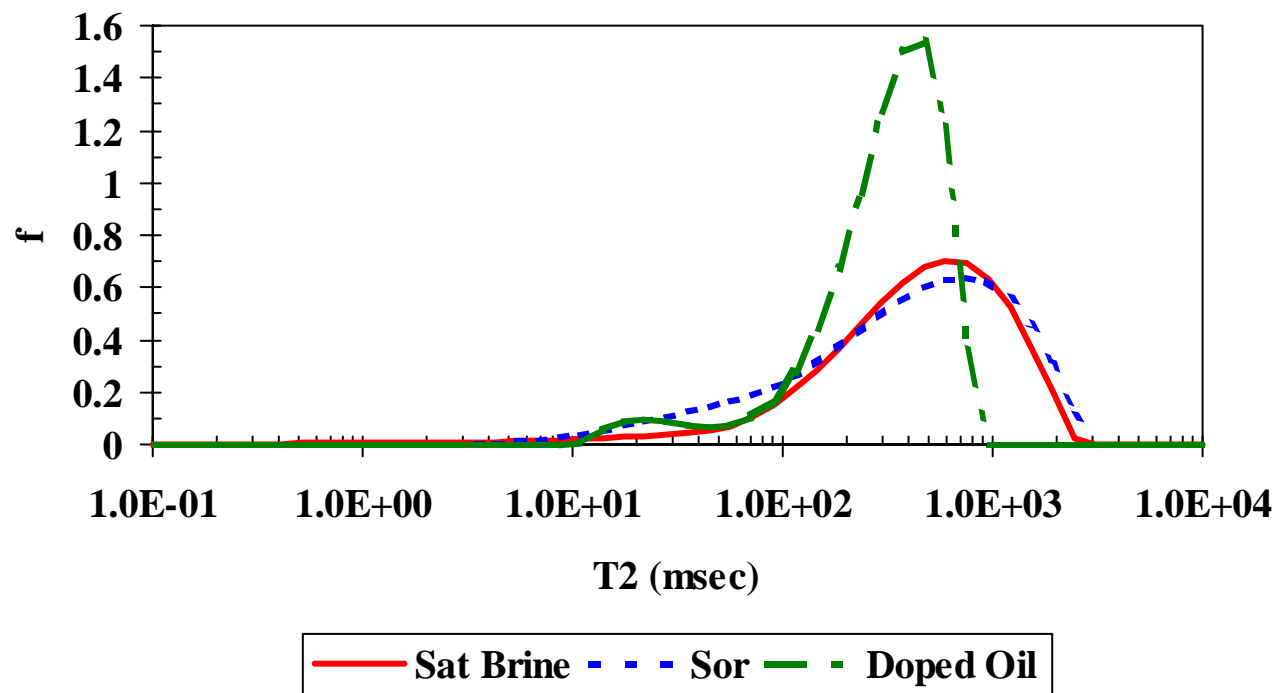


Fig 14. T_2 distribution for Chester Field sample and for doped oil

Summary

This work has demonstrated the use of X-ray CT scanning for studying porosity distribution, vugs distribution, preferential flow path and oil distribution at S_{wr} and S_{or} for core samples. CT scanning of dry Yates core material shows that uniformity of vug distribution varies from core to core. CT scanning of core floods in one Chester Field sample shows that the vugs are non-touching. The Chang and Vinegar correlation estimates the permeability correctly from NMR T_2 response because the vugs do not contribute to permeability in this sample. In the next six months, similar core flood experiments will be performed in some samples from the Yates field.

Acknowledgment

We would like to thank Marathon Oil Company and Shell Development Company for providing the carbonate samples.

Reference:

1. T.S. Ramakrishnan, A. Rabaute, E. J. Fordham, R. Ramamoorthy, M. Herron, A. Matteson, B. Raghuraman, A. Mahdi, M. Akbar and F. Kuchuk, "A Petrophysical and Petrographic Study of Carbonate Cores from Thamama formation", SPE 49502, 1998.
2. F. J. Lucia, "Carbonate Reservoir Characterization", Springer, New York, 1999.
3. D. Chang, H. Vinegar, C. Morriss, and C. Straley, "Effective Porosity, Producing Fluid, and Permeability in Carbonates from NMR Logging", The Log Analyst, 1997.
4. P. J. Hicks, Jr., "A Study of Heterogeneous Carbonate Cores Using X-Ray CT: Porosity, Residual Saturations and Miscible Displacements", Ph.D. Thesis, University of Houston, 1990.